<< Previous Chapter

PART II

RADIATIVE TRANSFER

Part II of our book develops the laws that govern the transfer of radiant energy from one location to another.

Chapter 4 discusses the transfer of radiant energy *across the air-water surface* of a natural water body. This chapter introduces the *interaction principle*, from which the entire formalism of radiative transfer theory can be derived. Here the interaction principle provides us with the *boundary conditions* that will be required for the solution of the radiative transfer equations to be developed in Chapter 5. Both radiance and irradiance levels of the interaction principle are presented. This chapter is distinguished by a discussion of the *numerical techniques* needed for a proper application of the interaction principles to wind-blown, random air-water surfaces. The chapter contains many numerically generated results, which illustrate the radiative transfer properties of wind-blown water surfaces.

Chapter 5 treats the transfer of radiant energy *within the water body*. The chapter begins with a discussion of the physical processes of absorption, elastic and inelastic scattering, and emission. We then develop the complete *radiance transfer equation,* from which the *two-flow equations* governing *irradiance* transfer are then obtained. We thoroughly discuss the input required for solution of the various equations. The two-flow equations yield several useful relations among inherent and apparent optical properties. We finish the chapter with a discussion of how polarization and the processes of Raman scattering, fluorescence, and bioluminescence are included in the radiative transfer equations. Discussion of the associated numerical techniques for solving the transfer equations is deferred to Part III.

This Page Intentionally Left Blank

Chapter 4

Across the Surface

Most of the photons descending from the atmosphere over an ocean or lake eventually reach the water surface. The surface reflects some of these photons back to the sky, and transmits the remainder into the water body. Likewise, photons within a water body occasionally strike the air-water surface from below; some of these photons pass through the surface into the air and some are reflected back into the water body. The precise description of this activity is partly provided by the *interaction principle* of radiative transfer theory written, in this instance, for the air-water surface. In this chapter we shall state the interaction principles for radiance and irradiance for a general wind-blown surface, and show how the associated *reflectance* and *transmittance* functions occurring in the principles can be evaluated. These interaction principles serve as *boundary conditions* for the solution of the radiance and irradiance equations of transfer within the water body.

We shall discuss three states of the air-water surface. The first is a level water surface, for which the associated surface reflectance and transmittance functions can be evaluated analytically. The second is a surface covered by wind-generated capillary waves. We shall discuss in some detail the numerical techniques needed for modeling of capillary-wave surfaces. Radiative transfer across such surfaces will be illustrated by numerically generated examples. Third, we show how the numerical techniques developed for capillary waves can be extended to gravity waves, or to well developed seas with all scales of wave motion.

Radiative transfer across wind-blown surfaces is in many ways more complex and difficult to describe quantitatively than is transfer within the water. Our discussion in this chapter therefore has some rather abstract and mathematical sections. We offer no apology for this, since it is not our fault that nature has made sea surfaces so complicated. However, those sections that deal primarily with numerical techniques, rather than with general principles or with illustrative examples, have their headings followed by two vertical bars: ||. If you wish only an overview of the subject, you may skip the barred sections without guilt. If you find our presentation of numerical algorithms to be tedious, just remember that the discussion here is considerably less tedious than having to figure out these matters for

yourself when it comes time to write a computer program. Those readers desiring to apply radiative transfer theory to the numerical solution of their own problems will find the barred sections very useful, since the path from elegant theory to numerical algorithms is seldom obvious.

4.1 Interaction Principles

See Note

Radiative transfer theory is distinguished by the fact that it is one of the branches of physics that can be made to rest on a single principle from which all the salient structures of the theory can be systematically deduced. In this sense it is a closed subset of electromagnetic theory. The principle that permits this mode of construction of radiative transfer theory is called the *interaction principle* [see Supplementary Note 3].

The interaction principle is a statement of the linearity of classical radiative transfer processes. Thus *radiative transfer theory*, a complex web of deductions following from the principle, is at its core a *linear theory of the interaction of light with matter* on a *phenomenological* level. The structure of the theory arises from two restrictions placed on the theory by its principal developers.

The first restriction is that the theory be concerned only with electromagnetic radiation of low irradiances and of low photon energies. By "low irradiances" we mean that the radiant energy incident on a material medium induces a response in the medium that is directly proportional to the magnitude of the electric field describing the radiation. It is this linear response – and the linearity of Maxwell's equations – that leads, for example, to the simple laws of reflection and refraction that we shall encounter in Section 4.2. At extremely high irradiances, typically greater than 10^{10} W m^{-2} (as can be generated with lasers), materials may exhibit responses that are proportional to the square (or higher powers) of the electric field. The resulting phenomena, such as frequency doubling of light passing through a crystal, are the subject matter of modern *nonlinear optics*. By "low photon energies" we mean that the photons lack enough energy to produce phenomena such as the excitation of atomic nuclei or pair production (conversion of a photon into an electron-positron pair), as can occur with gamma rays. Such phenomena require the tools of quantum mechanics for study. At ultraviolet to infrared wavelengths, photons can induce atomic electron transitions and can excite molecular vibrations and rotations, but no more. The typical irradiances of 10^{3} W m^{-2} at visible wavelengths encountered in hydrologic optics are well within the "low irradiance, low photon energy" domain for which radiative transfer theory is valid. Note that radiative transfer theory

does include *inelastic* phenomena such as spontaneous Raman scattering and fluorescence, which are well described as linear responses of optical media.

The second restriction placed on radiative transfer theory is that it be a *phenomenological* theory. That is to say, *we make our measurements and define our variables at a macroscopic level of observation for which geometrical optics is valid, and we do not examine the underlying causes of physical phenomena*. For example, the volume scattering function β contains all of the information needed to completely describe the scattering properties of a given macroscopic volume of water. Neither the microscopic, physical details of the scattering process (e.g. absorption and re-emission of photons by atoms), nor the scattering phenomena of physical optics (e.g. diffraction) are within the purview of radiative transfer theory. It is only the net effect of these microscopic, physical processes as parameterized by the bulk quantity β that is of interest.

Of course, we legitimately may wish to *predict* the value of the scattering function β from first principles and a knowledge of the constituents of a water sample. We outlined in Section 3.11 one way in which this can be done. However, this noble endeavor cannot be accomplished within the framework of classical radiative transfer theory.

Plane-parallel water bodies

Our subsequent detailed development of radiative transfer theory will be restricted to the special case of *plane-parallel* water bodies. Thus we assume that the water body is infinite in horizontal extent and that there are no horizontal variations of inherent optical properties or of boundary conditions. The inherent optical properties of the water body may, however, vary arbitrarily with depth. These assumptions reduce the number of spatial variables to one, the depth, and allow us to discuss hydrologic optics in the simplest setting that is still a usefully realistic model of nature. But more importantly, the adoption of plane-parallel water bodies will enable us to employ some very powerful mathematical techniques that are applicable only to problems with simplified geometry.

In Section 1.4 and Fig. 1.3 we adopted a cartesian coordinate system in which the nadir direction $\hat{\boldsymbol{i}}_3$ is used as the reference direction for defining the polar angle θ, and the downwind direction $\hat{\boldsymbol{i}}_1$ is the reference for the azimuthal angle ϕ. We now consider the depth variable x_3 in more detail. Observations taken at sea are recorded in terms of the *geometric depth* z, measured in meters positive downward from the mean sea surface. We shall learn in Chapter 5 that the relevant measure of depth in computing

underwater light fields is the *optical depth* ζ, which is defined via

$$d\zeta \equiv c(z)\,dz\,, \tag{4.1}$$

where $c(z)$ is the beam attenuation coefficient at geometric depth z, and $d\zeta$ and dz are infinitesimal increments of ζ and z. Note that because c has units of m^{-1}, the *optical depth is nondimensional*. The standard symbol for optical depth is τ. However, we wish to reserve τ for later use (as a local transmittance). We therefore adopt the Greek equivalent of z as a reasonable replacement for τ. The symbol z will always denote geometric depth, as is customary in oceanography.

We shall take the depth variable x_3 to be either geometric depth z or optical depth ζ, as is convenient at the moment; both have the value zero at mean sea level. We can obtain the finite optical depth ζ corresponding to a finite geometric depth z by integration of Eq. (4.1):

$$\zeta = \int_0^z c(z')\,dz'\,. \tag{4.2}$$

If the beam attenuation coefficient is known as a function of the optical depth, we can obtain corresponding z and ζ values from

$$z = \int_0^\zeta \frac{1}{c(\zeta')}\,d\zeta'\,.$$

It will prove very convenient to denote certain depths as follows. Let "a" denote depth zero, but *in the air just above the water surface*; let "w" be depth zero, but *in the water just below the surface*. The air-water surface is then an infinitesimally thin slab between depths a and w, denoted by $S[a,w]$. Corresponding optical and geometric depths *within the water body* are denoted by "ζ" and "z," respectively. When we need to specify several arbitrary depths within the water body, we shall use subscripts on ζ or z, e.g. ζ_1, ζ_2, and ζ_3, where $\zeta_1 \le \zeta_2 \le \zeta_3$ always. Next, let "m" be the *maximum depth of interest*, i.e. the greatest depth at which we wish to study the optical properties of the water body. Finally, let "b" denote the *bottom of the water body*. The context in a given discussion will make clear whether m and b represent optical or geometric depths. The region of interest is then the slab $S[w,m]$, and the bottom boundary of the water body is the slab $S[m,b]$. The lower boundary $S[m,b]$ can be either an infinitesimally thin surface representing, say, a muddy or sandy bottom, or $S[m,b]$ can represent a finitely or infinitely thick slab of water below the greatest depth of interest. Indeed, the surface $S[a,w]$ can in principle

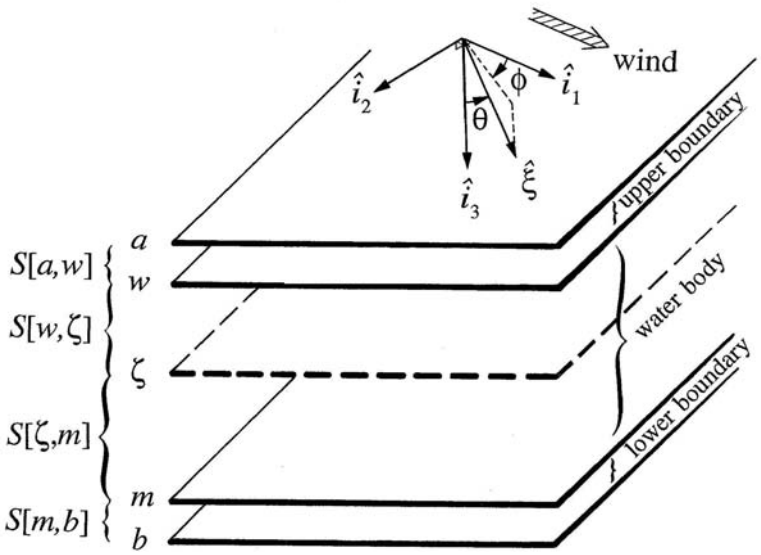

Fig. 4.1. Representation of a plane-parallel water body and the associated coordinate system. [redrawn from Mobley and Preisendorfer (1988)]

represent a finitely thick layer such as a glass plate or a film of oil, but we shall not explicitly consider this possibility. Clearly we then have

$$0 \equiv a \le w \le \zeta_1 \le \zeta_2 \le \zeta_3 \le m \le b < \infty .$$

The plane-parallel water body and associated coordinate system are shown in Fig. 4.1.

Interaction principle for the air-water surface

The interaction principle for the air-water surface $S[a,w]$ is an algebraic prescription for calculating the radiant power *emerging* from the surface when the radiant power *incident* on the surface is specified. We shall formulate the principle for both radiances and the irradiances.

Recalling the definitions and discussions in Chapter 1, we can, for brevity, let $L(\zeta;\hat{\xi})$ be the (monochromatic) spectral radiance at optical depth ζ and in direction $\hat{\xi} = (\theta,\phi)$; the wavelength λ and time t are understood. With this notation, $L(a;\hat{\xi})$, $\hat{\xi} \in \Xi_d$, represents the downward radiance incident on the air-water surface from above; this radiance is called the *air-incident* radiance. Likewise, $L(w;\hat{\xi})$, $\hat{\xi} \in \Xi_u$, is the radiance incident on

the surface $S[a,w]$ from below; this is the *water-incident* radiance. These incident radiances give rise to two *response* radiances: $L(a;\hat{\xi})$, $\hat{\xi} \in \Xi_u$, emanating from the upper side of the surface and $L(w;\hat{\xi})$, $\hat{\xi} \in \Xi_d$, emanating from the lower side of $S[a,w]$.

The interaction principle for radiance then asserts the existence of four radiance transfer functions associated with $S[a,w]$, namely $t(w,a;\hat{\xi}'\rightarrow\hat{\xi})$, $r(a,w;\hat{\xi}'\rightarrow\hat{\xi})$, $r(w,a;\hat{\xi}'\rightarrow\hat{\xi})$ and $t(a,w;\hat{\xi}'\rightarrow\hat{\xi})$, each of dimension sr^{-1}, such that

$$L(a;\hat{\xi}) = \int_{\Xi_u} L(w;\hat{\xi}')\, t(w,a;\hat{\xi}'\rightarrow\hat{\xi})\, d\Omega(\hat{\xi}') + \int_{\Xi_d} L(a;\hat{\xi}')\, r(a,w;\hat{\xi}'\rightarrow\hat{\xi})\, d\Omega(\hat{\xi}') \qquad \text{for } \hat{\xi} \in \Xi_u, \tag{4.3}$$

and

$$L(w;\hat{\xi}) = \int_{\Xi_u} L(w;\hat{\xi}')\, r(w,a;\hat{\xi}'\rightarrow\hat{\xi})\, d\Omega(\hat{\xi}') + \int_{\Xi_d} L(a;\hat{\xi}')\, t(a,w;\hat{\xi}'\rightarrow\hat{\xi})\, d\Omega(\hat{\xi}') \qquad \text{for } \hat{\xi} \in \Xi_d. \tag{4.4}$$

The physical interpretations of Eqs. (4.3) and (4.4) are quite simple. Consider Eq. (4.3). On the left hand side we have the radiance just above the surface (at "depth" a); this radiance is directed away from the surface ($\hat{\xi} \in \Xi_u$, i.e. the photons are traveling upward). The first term on the right hand side of Eq. (4.3) specifies how much of the radiance incident on the bottom side of the surface (depth w) in the upward direction ($\hat{\xi}' \in \Xi_u$) is transmitted through the surface and into direction $\hat{\xi}$. The integration over all $\hat{\xi}' \in \Xi_u$ merely adds up the radiance $L(\mathrm{w};\hat{\xi}')$ incident in all upward directions, which is transmitted in some amount determined by $t(w,a;\hat{\xi}'\rightarrow\hat{\xi})$ into direction $\hat{\xi}$. The second term on the right hand side tells us how much $[r(a,w;\hat{\xi}'\rightarrow\hat{\xi})]$ of the downward ($\hat{\xi}' \in \Xi_d$) radiance incident on the upper side of the surface (depth a) is reflected back upward into direction $\hat{\xi} \in \Xi_u$ by the surface between depths a and w. A corresponding interpretation holds for Eq. (4.4): now the left hand side gives the radiance just below the surface (depth w) that is directed away from the surface ($\hat{\xi} \in \Xi_d$), and so on.

Note how the order of the depth arguments a and w reminds us of the distinct physical processes: $t(a,w;\hat{\xi}'\rightarrow\hat{\xi})$ transmits radiance from above the surface to below (i.e. from depth a to depth w), whereas $t(w,a;\hat{\xi}'\rightarrow\hat{\xi})$ transmits radiance from below the surface to above it (i.e. from depth w to depth a). Likewise, radiance reflectance from the air side of the surface,

$r(a,w;\hat{\boldsymbol{\xi}}'\rightarrow\hat{\boldsymbol{\xi}})$, is physically different from reflectance from the water side, $r(w,a;\hat{\boldsymbol{\xi}}'\rightarrow\hat{\boldsymbol{\xi}})$. The direction of the arrow in the $\hat{\boldsymbol{\xi}}'\rightarrow\hat{\boldsymbol{\xi}}$ part of the argument reminds us that photons (radiance) originally traveling in direction $\hat{\boldsymbol{\xi}}'$ are reflected or transmitted into direction $\hat{\boldsymbol{\xi}}$.

It is implicitly assumed in writing Eqs. (4.3) and (4.4) that the surface $S[a,w]$ neither absorbs nor emits photons – it only reflects or transmits them. This assumption is physically reasonable since, for our present purposes, $S[a,w]$ represents just a discontinuity in the real index of refraction, not a finite layer of a material medium.

We can obtain the *interaction principle for irradiance* from Eqs. (4.3) and (4.4). Multiplying Eq. (4.3) by $|\hat{\boldsymbol{\xi}}\cdot\hat{\boldsymbol{i}}_3|$ (note that $\hat{\boldsymbol{\xi}}\cdot\hat{\boldsymbol{\xi}}\,\hat{\boldsymbol{i}}_3 \le 0$) and integrating over Ξ_u, and multiplying Eq. (4.4) by $|\hat{\boldsymbol{\xi}}\cdot\hat{\boldsymbol{\xi}}\,\hat{\boldsymbol{i}}_3|$ (although now $\hat{\boldsymbol{\xi}}\cdot\hat{\boldsymbol{\xi}}\,\hat{\boldsymbol{i}}_3 > 0$) and integrating over Ξ_d, we find

$$E_u(a) = E_u(w)\,t(w,a) + E_d(a)\,r(a,w)\,, \tag{4.5}$$

and

$$E_d(w) = E_u(w)\,r(w,a) + E_d(a)\,t(a,w)\,. \tag{4.6}$$

Here E_u and E_d are the upward and downward spectral plane irradiances at the indicated depths. In order to obtain the simple forms of Eqs. (4.5) and (4.6), we have defined four *irradiance transfer functions*:

$$t(w,a) \equiv t_- \equiv \frac{1}{E_u(w)} \int_{\Xi_u} \left[\int_{\Xi_u} L(w;\hat{\boldsymbol{\xi}}')\, t(w,a;\hat{\boldsymbol{\xi}}'\rightarrow\hat{\boldsymbol{\xi}})\, d\Omega(\hat{\boldsymbol{\xi}}') \right] |\hat{\boldsymbol{\xi}}\cdot\hat{\boldsymbol{i}}_3|\, d\Omega(\hat{\boldsymbol{\xi}})\,, \tag{4.7a}$$

$$r(a,w) \equiv r_+ \equiv \frac{1}{E_d(a)} \int_{\Xi_u} \left[\int_{\Xi_d} L(a;\hat{\boldsymbol{\xi}}')\, r(a,w;\hat{\boldsymbol{\xi}}'\rightarrow\hat{\boldsymbol{\xi}})\, d\Omega(\hat{\boldsymbol{\xi}}') \right] |\hat{\boldsymbol{\xi}}\cdot\hat{\boldsymbol{i}}_3|\, d\Omega(\hat{\boldsymbol{\xi}})\,, \tag{4.7b}$$

$$r(w,a) \equiv r_- \equiv \frac{1}{E_u(w)} \int_{\Xi_d} \left[\int_{\Xi_u} L(w;\hat{\boldsymbol{\xi}}')\, r(w,a;\hat{\boldsymbol{\xi}}'\rightarrow\hat{\boldsymbol{\xi}})\, d\Omega(\hat{\boldsymbol{\xi}}') \right] |\hat{\boldsymbol{\xi}}\cdot\hat{\boldsymbol{i}}_3|\, d\Omega(\hat{\boldsymbol{\xi}})\,, \tag{4.7c}$$

$$t(a,w) \equiv t_+ \equiv \frac{1}{E_d(a)} \int_{\Xi_d} \left[\int_{\Xi_d} L(a;\hat{\boldsymbol{\xi}}')\, t(a,w;\hat{\boldsymbol{\xi}}'\rightarrow\hat{\boldsymbol{\xi}})\, d\Omega(\hat{\boldsymbol{\xi}}') \right] |\hat{\boldsymbol{\xi}}\cdot\hat{\boldsymbol{i}}_3|\, d\Omega(\hat{\boldsymbol{\xi}})\,. \tag{4.7d}$$

Observe that the *irradiance* transfer functions are dimensionless.

If the four radiance transfer functions are known, then Eqs. (4.3) and (4.4) tell us *all there is to know about how the air-water surface affects any incident radiance distribution.* Likewise, if the irradiance transfer functions of Eq. (4.7) are known, then Eqs. (4.5) and (4.6) completely specify the

surface as regards its effect on the incident irradiance corresponding to the incident radiance seen in Eqs. (4.7). Unfortunately, however, the elegant interaction principle gives us no clue as to how the needed transfer functions are obtained in practice. Our main purposes in the remainder of this chapter are to develop a means of evaluating the transfer functions for a wind-blown water surface, and to obtain some intuitive feeling for the nature of these functions. We shall see that in all cases the transfer functions for both irradiance and radiance can be approximately evaluated using Monte Carlo procedures. Alternatively, since radiance is more fundamental than irradiance, the irradiance transfer functions can be determined by a numerical integration of Eq. (4.7), once the radiance transfer functions have been determined by a Monte Carlo procedure.

Note that *the radiance transfer functions,* $t(w,a;\hat{\xi}' \rightarrow \hat{\xi})$ *etc., depend only on the nature of the air-water surface; thus they are inherent optical properties* (IOP's). However, *the irradiance transfer functions*, $t(w,a)$ *etc., depend both on the nature of the surface and on the incident radiance distribution,* as is seen in the defining Eqs. (4.7). *The irradiance transfer functions are therefore not IOP's.* This is our first hint that irradiance, which appears simpler than radiance because it does not contain detailed directional information, is in fact often more difficult to treat mathematically than is radiance. We shall say more about this matter in Section 5.10.

The specific form of the interaction principle used here for the air-water surface is derived from the general statement of the principle found in Preisendorfer (1965, p. 114) or in *H.O. II*, p. 205. The interaction principle is simply a *formalization* (a translation into mathematical form) of the requirement that radiative transfer theory on the phenomenological level be a linear theory. The principle then supplies the linear operators needed to describe the phenomenon. The integrals in Eqs. (4.3) and (4.4) are examples of these linear operators; the transfer functions, $t(w,a;\hat{\xi}' \rightarrow \hat{\xi})$ and its three partners, are the *kernels* of these operators. Mathematical concerns about the existence of the operators are addressed in *H.O. II*, p. 372. The interaction method of formulating problems in radiative transfer theory is treated in detail in *H.O. II*, Chapter 3.

4.2 The Level Surface

It is a rare day when a lake or ocean surface is glassy calm, for even a slight breeze will ruffle the water surface with capillary waves, and ocean swell may be present on a surface that otherwise would be calm. However, discussion of a level water surface is not just an idle mathematical exercise

of little applicability to natural waters. First, a level surface allows us to introduce several important concepts in their simplest form, and thereby gain some intuition about the physical processes involved. Second, our numerical treatment of wind-blown air-water surfaces rests on a resolution of the wave-covered surface into small wave facets, each of which can be treated as a locally plane surface (although tilted from the horizontal) obeying the laws of geometrical optics now to be discussed.

When the air-water surface is a flat horizontal plane, the reflection and transmission of photons across the surface follow directly from the laws of geometrical optics. There are two cases to consider, as shown in Fig. 4.2, namely the *air-incident* and *water-incident* cases. As above, the term "air-incident" refers to downward traveling photons that are incident from the air onto the water surface. "Water-incident" refers to upward traveling photons incident from the water body onto the water surface. The air-water surface divides space into two regions: the atmosphere, with real index of refraction n_a, and the water body, with index of refraction n_w. The convenient approximations $n_a = 1$ and $n_w = 1.34$ are sufficiently accurate for our present purposes.

Fresnel reflectance

We now find the concept of a *light ray* to be convenient. We envision a ray simply as a narrow beam of photons traveling in almost the same direction. The ray has a given spectral power, small cross sectional area, and small solid angle, from which the radiance of the ray can be defined using Eq. (1.20). A collimated laser beam is a good physical approximation to the concept of a ray.

In the air-incident case shown in Fig. 4.2(a), such a ray of photons approaches the air-water surface along direction $\hat{\boldsymbol{\xi}}'$ in Ξ_d; $\hat{\boldsymbol{n}}$ is a unit vector normal to the surface and directed upward ($\hat{\boldsymbol{n}} = -\hat{\boldsymbol{\imath}}_3$). Upon reaching the water surface, the ray $\hat{\boldsymbol{\xi}}'$ produces two daughter rays: a reflected ray along $\hat{\boldsymbol{\xi}}_r$ and a transmitted (refracted) ray along $\hat{\boldsymbol{\xi}}_t$. The directions $\hat{\boldsymbol{\xi}}_r$ and $\hat{\boldsymbol{\xi}}_t$ lie in the plane defined by $\hat{\boldsymbol{\xi}}'$ and $\hat{\boldsymbol{n}}$. One can compute the directions $\hat{\boldsymbol{\xi}}_r$ and $\hat{\boldsymbol{\xi}}_t$ by observing the colinearity of the vector tips of the reflected direction and the modified transmitted or incident directions. This colinearity, which is shown by the dashed lines in Fig. 4.2, follows from Snell's law written for the air-incident case:

$$\sin\theta' = n_w \sin\theta_t . \tag{4.8}$$

The resulting expressions for the reflected and transmitted ray directions are

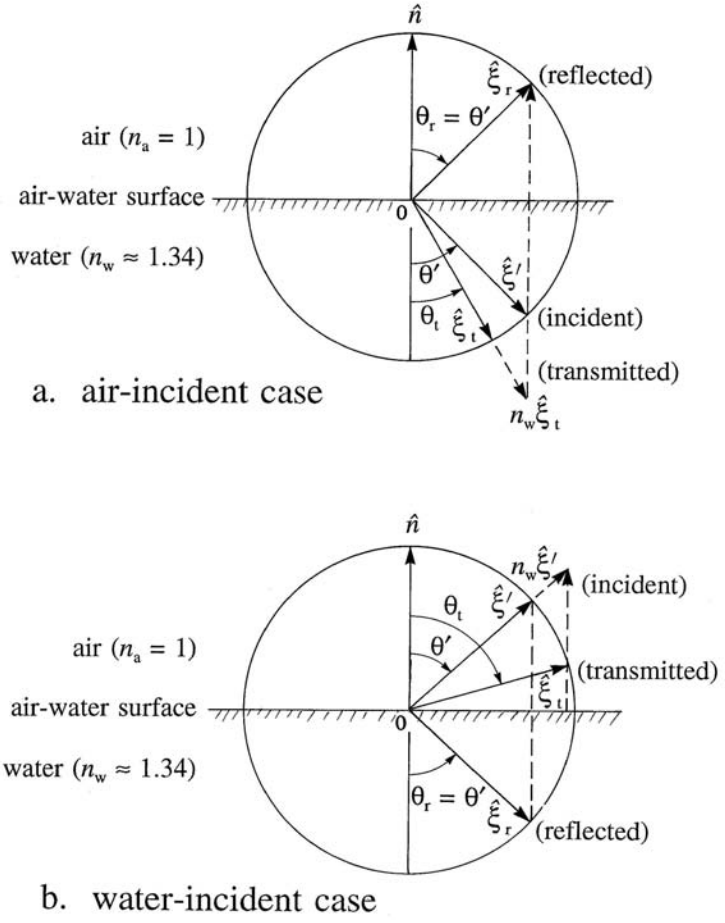

Fig. 4.2. Schematic diagrams for reflected and refracted rays. The diagrams summarize Eqs. (4.8)-(4.13). [redrawn from Preisendorfer and Mobley (1985)]

$$\hat{\xi}_r = \hat{\xi}' - 2\,(\hat{\xi}'\cdot\hat{n})\,\hat{n} \tag{4.9a}$$

and

$$\hat{\xi}_t = \frac{1}{n_w}\,(\hat{\xi}' - c\,\hat{n})\,, \tag{4.9b}$$

where

$$c \equiv \hat{\xi}'\cdot\hat{n} + \left[(\hat{\xi}'\cdot\hat{n})^2 + n_w^2 - 1\right]^{1/2}. \tag{4.9c}$$

The angles of reflection and transmission are given by

$$\theta_r = \cos^{-1}|\hat{\xi}'\cdot\hat{n}| = \theta' \tag{4.10a}$$

and

$$\theta_t = \sin^{-1}\left(\frac{1}{n_w}\sin\theta'\right), \tag{4.10b}$$

respectively.

For the water-incident case shown in Fig. 4.2(b), Snell's law reads

$$n_w \sin\theta' = \sin\theta_t . \tag{4.11}$$

The reflected and transmitted directions are

$$\hat{\xi}_r = \hat{\xi}' - 2(\hat{\xi}'\cdot\hat{n})\hat{n}, \tag{4.12a}$$

and

$$\hat{\xi}_t = n_w\hat{\xi}' - c\hat{n}, \tag{4.12b}$$

where

$$c \equiv n_w\hat{\xi}'\cdot\hat{n} - \left[(n_w\hat{\xi}'\cdot\hat{n})^2 - n_w^2 + 1\right]^{1/2}, \tag{4.12c}$$

and the corresponding angles of reflection and transmission are

$$\theta_r = \cos^{-1}|\hat{\xi}'\cdot\hat{n}| = \theta' \tag{4.13a}$$

and

$$\theta_t = \sin^{-1}(n_w\sin\theta') . \tag{4.13b}$$

For either the air-incident or the water-incident case, the *reflectance* $r(\theta')$ of the unperturbed air-water surface for unpolarized incident radiant energy is given by *Fresnel's formula* (Sears, 1949, p. 174):

$$r(\theta') \equiv r(\hat{\xi}'\cdot\hat{n}) = \frac{1}{2}\left\{\left[\frac{\sin(\theta'-\theta_t)}{\sin(\theta'+\theta_t)}\right]^2 + \left[\frac{\tan(\theta'-\theta_t)}{\tan(\theta'+\theta_t)}\right]^2\right\}, \tag{4.14a}$$

which holds if $\theta' \neq 0$. In the case of normal incidence, $\theta' = 0$ and hence $\theta_r = \theta_t = 0$ also. Equation (4.14a) is then indeterminate. In this special case the surface reflectance is given by [see Supplementary Note 4]

$$r(0) = \left(\frac{n_w - 1}{n_w + 1}\right)^2 . \tag{4.14b}$$

See Note

The Fresnel reflectance lies in the interval $0 \le r(\theta') \le 1$ and gives the fraction of photons incident in a narrow beam along $\hat{\xi}'$ (from air or water) that is reflected by the surface. In other words, $r(\theta')$ gives the fraction of the incident irradiance of a collimated beam that is reflected by a level surface. Figure 4.3 shows the behavior of $r(\theta')$ for both air-incident and water-incident rays. The reflectance is shown for two values of n_w, which bracket the range of n_w encountered in natural waters. For both air- and water-incident rays, the reflectance is 0.02 to 0.03 for rays with incident angles of less than 30°. For air-incident rays, the reflectance does not exceed 0.1 until the angle of incidence is greater than 65°. For water-incident rays, however, the reflectance increases very rapidly for θ' greater than 30°, and equals one for incident angles greater than or equal to the critical angle $\theta' = \sin^{-1}(1/n_w) \approx 48°$. This phenomenon of *total internal reflection* greatly influences the passage of radiant energy back and forth across the sea surface. For example, an air-incident ray with $\theta' = 50°$ transmits at least 96% of its energy through a level surface and into the water, whereas a water-incident ray with $\theta' = 50°$ transmits none of its energy into the air. Thus, figuratively stated, it is much easier for light to get "into the water" than it is for light to get "out of the water."

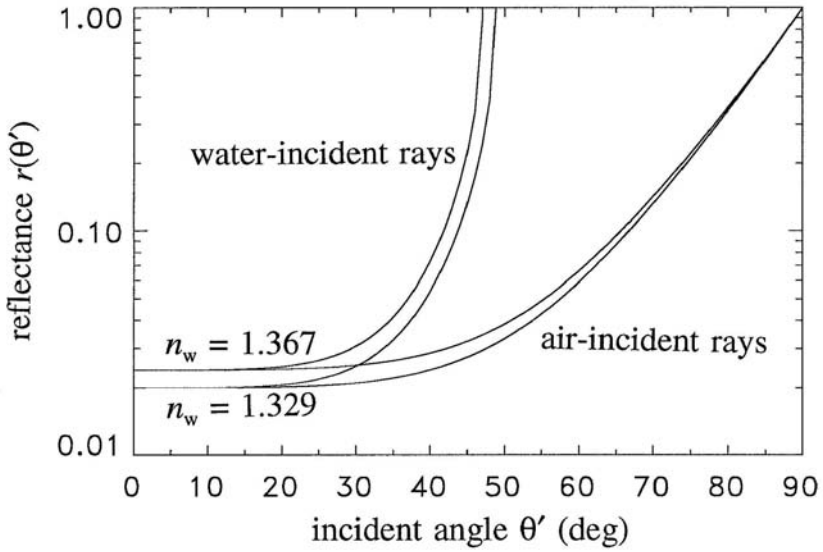

Fig. 4.3. Behavior of the Fresnel reflectance function of Eq. (4.14) for the extreme values of the real index of refraction n_w encountered in hydrologic optics.

The n^2 law for radiance

We now pause to pick up an important law of geometrical radiometry, the n^2 law for radiance. To see the general form of this law, consider two media separated by a transparent surface, as in Fig. 4.4(a). Suppose that a ray with central direction $\hat{\boldsymbol{\xi}}_1$ in medium 1, of index of refraction n_1, is incident on a locally plane boundary surface, which has a normal $\hat{\boldsymbol{n}}$. Further, suppose that the ray crosses the interface and passes into medium 2, of index of refraction n_2. The central refracted direction is $\hat{\boldsymbol{\xi}}_2$, which lies in the plane defined by $\hat{\boldsymbol{\xi}}_1$ and $\hat{\boldsymbol{n}}$. With the incident and refracted angles θ_1 and θ_2 assigned to $\hat{\boldsymbol{\xi}}_1$ and $\hat{\boldsymbol{\xi}}_2$ as shown in Fig. 4.4(a), Snell's law states that θ_1 and θ_2 are related by

$$n_1 \sin\theta_1 = n_2 \sin\theta_2 . \tag{4.15}$$

By construction, the azimuthal spreads $\Delta\phi_1$ and $\Delta\phi_2$ of the rays are equal and of magnitude, say, $\Delta\phi$. The narrow rays then have solid angles given by [recall Eq. (1.12)]

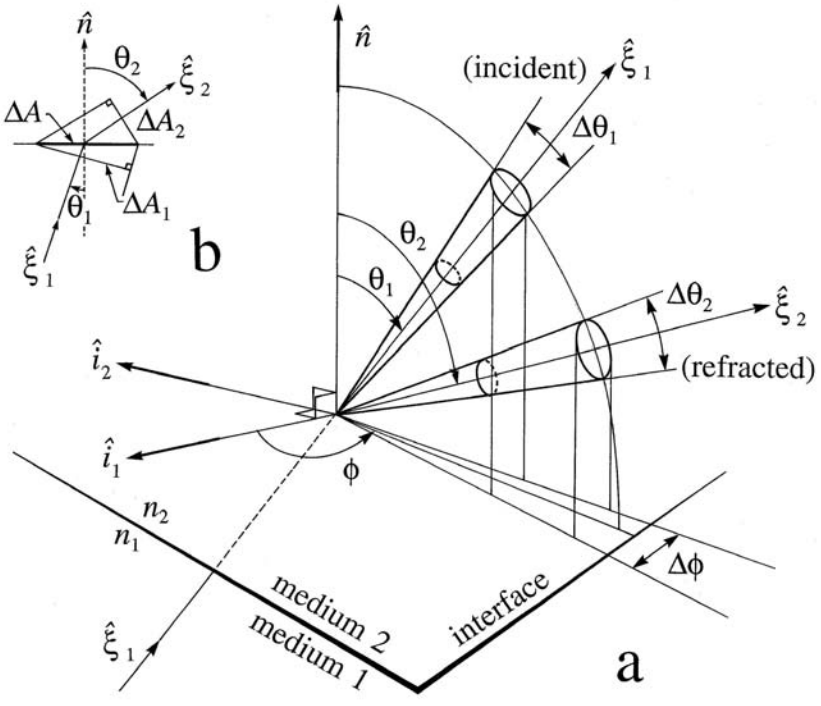

Fig. 4.4. Geometry used in deriving the n^2 law for radiance.

$$\Delta\Omega_1 = \sin\theta_1 \Delta\theta_1 \Delta\phi \quad \text{and} \quad \Delta\Omega_2 = \sin\theta_2 \Delta\theta_2 \Delta\phi . \tag{4.16}$$

Now, squaring each side of Eq. (4.15) and taking differentials gives

$$n_1^2 \sin\theta_1 \cos\theta_1 \Delta\theta_1 = n_2^2 \sin\theta_2 \cos\theta_2 \Delta\theta_2 .$$

Multiplying each side of this equation by $\Delta\phi$ and using Eq. (4.16), we come to

$$n_1^2 \cos\theta_1 \Delta\Omega_1 = n_2^2 \cos\theta_2 \Delta\Omega_2 , \tag{4.17}$$

which is called *Straubel's invariant* in geometrical optics.

We now can derive the n^2-law for radiance. Let the radiances of the two rays be

$$L_1 = \frac{\Delta\Phi_1}{\Delta A_1 \Delta\Omega_1} \quad \text{and} \quad L_2 = \frac{\Delta\Phi_2}{\Delta A_2 \Delta\Omega_2} , \tag{4.18}$$

where $\Delta\Phi_j$ and ΔA_j are, respectively, the spectral radiant powers and the cross-sectional areas of the incident ($j = 1$) and refracted ($j = 2$) rays. Now, from Eq. (4.14) we know $r(\hat{\boldsymbol{\xi}}_1 \cdot \hat{\boldsymbol{n}})$, and hence the Fresnel transmittance $t(\hat{\boldsymbol{\xi}}_1 \cdot \hat{\boldsymbol{n}}) = 1 - r(\hat{\boldsymbol{\xi}}_1 \cdot \hat{\boldsymbol{n}})$ of the air-water surface. Thus we know

$$\frac{\Delta\Phi_2}{\Delta\Phi_1} = t(\hat{\boldsymbol{\xi}}_1 \cdot \hat{\boldsymbol{n}}) . \tag{4.19}$$

Observe from Fig. 4.4(b) that ΔA_1 and ΔA_2 are related to ΔA by

$$\Delta A_1 = \Delta A \cos\theta_1 \quad \text{and} \quad \Delta A_2 = \Delta A \cos\theta_2 . \tag{4.20}$$

Now, from Eq. (4.18) we have

$$\frac{L_2}{L_1} = \frac{\Delta\Phi_2}{\Delta\Phi_1} \frac{\Delta A_1 \Delta\Omega_1}{\Delta A_2 \Delta\Omega_2} ,$$

which by Eqs. (4.19) and (4.20) has the equivalent form

$$\frac{L_2}{L_1} = t(\hat{\boldsymbol{\xi}}_1 \cdot \hat{\boldsymbol{n}}) \frac{\cos\theta_1 \Delta\Omega_1}{\cos\theta_2 \Delta\Omega_2} . \tag{4.21a}$$

Straubel's invariant (4.17) reduces this to still another equivalent form:

$$\frac{L_2}{L_1} = t(\hat{\boldsymbol{\xi}}_1 \cdot \hat{\boldsymbol{n}}) \frac{n_2^2}{n_1^2} , \tag{4.21b}$$

or

$$\frac{L_2}{n_2^2} = t(\hat{\boldsymbol{\xi}}_1 \cdot \hat{\boldsymbol{n}}) \frac{L_1}{n_1^2} . \tag{4.21c}$$

Equation (4.21) in any of its forms is the desired n^2 *law for radiance.*

We have derived the n^2 law from considerations of a beam of photons traveling an infinitesimal distance across the boundary from one medium to another. For this geometry, Eq. (4.21) is exact. The n^2 law is valid for *finite* path lengths in the two media, *to the accuracy with which absorption and scattering out of the beam within the media can be ignored.* If we also take $t(\hat{\boldsymbol{\xi}}_1 \cdot \hat{\boldsymbol{n}}) \approx 1$ [as is the case of nearly normal incidence on an air-water surface, for which $t(\hat{\boldsymbol{\xi}}_1 \cdot \hat{\boldsymbol{n}}) \approx 0.97$ as seen in Fig. 4.3], then Eq. (4.21) reduces to

$$\frac{L_2}{n_2^2} \approx \frac{L_1}{n_1^2} . \tag{4.22}$$

This result is known as the *fundamental theorem of radiometry* (Wyatt, 1978). The theorem is often stated as "the radiance divided by the square of the index of refraction is constant along any path." However, because all real substances have at least some absorption and scattering, the theorem is strictly true only for paths in a vacuum. In this case, $n_1 = n_2 = 1$, and Eq. (4.22) reduces to just $L_2 = L_1$, which is the radiance invariance law of Section 1.5. Equation (4.21) is thus a generalization of Eq. (1.33) to the case of material media.

A useful corollary of the n^2 law arises when we consider the successive crossings of a ray from one medium to another, as in the case of successive interactions of photons with a random air-water surface. Consider Fig. 4.5. A ray $\hat{\boldsymbol{\xi}}_1$ of radiance L_1 starts in a medium with index of refraction n_1, goes through a succession of refractions, and ends up with radiance L_s in a medium of refractive index n_s. In the j^{th} crossing of a surface, the incident radiance is L_j, the direction of incidence is $\hat{\boldsymbol{\xi}}_j$, and the interface normal is $\hat{\boldsymbol{n}}_j$, so that the Fresnel transmittance $1 - r(\hat{\boldsymbol{\xi}}_j \cdot \hat{\boldsymbol{n}}_j)$ is determined. Let $t(j,j+1)$ be the Fresnel transmittance of the interface between the media with refractive indexes n_j and n_{j+1}. Then by successive applications of Eq. (4.21b) we find

$$\frac{L_s}{L_1} = \prod_{j=1}^{s-1} t(j,j+1) \frac{n_s^2}{n_1^2} . \tag{4.23}$$

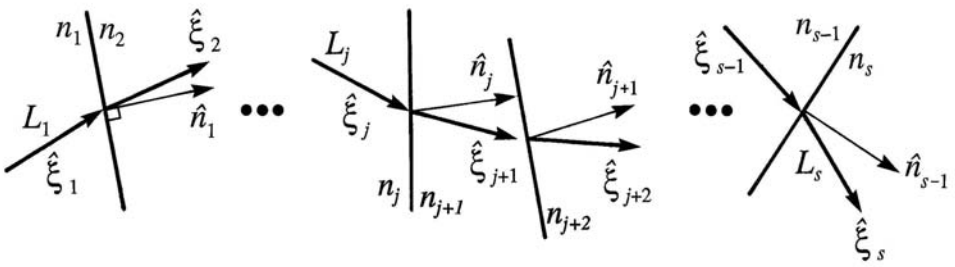

Fig. 4.5. An arbitrary sequence of ray-surface refractions.

Equivalently, for the radiant powers $\Phi_s = L_s \Delta\Omega_s \Delta A_s$ and $\Phi_1 = L_1 \Delta\Omega_1 \Delta A_1$,

$$\frac{\Phi_s}{\Phi_1} = \prod_{j=1}^{s-1} t(j, j+1) , \tag{4.24}$$

where Eq. (4.17) has been used in the reduction of Eq. (4.23). Equation (4.23) shows that the final radiance L_s depends only on the initial radiance L_1, on the initial and final indexes of refraction, and on the product of the transmittances. If the ray begins and ends in air or begins and ends in water, then $n_s = n_1$, and $L_s = L_1 \Pi\, t(j,j+1)$. Equation (4.24) is even simpler: the radiant power of a ray is affected only by the Fresnel transmittances. This result will be useful below in the Monte Carlo determinations of the air-water surface transfer functions. In particular it shows that as the radiant *power* of a transmitted ray is traced through a set of air and water regions, it is *not* necessary to include the n_j^2 factors.

Transfer functions for a level surface

We are now in a position to determine the explicit forms of the four radiance transfer functions for a level air-water surface.

The Fresnel formula (4.14) and the law of reflection (4.9a) allow us to write the air-incident radiance reflection function of Eq. (4.3) as

$$\begin{aligned} r(a,w;\hat{\xi}' \to \hat{\xi}) &= r(\hat{\xi}' \cdot \hat{n})\, \delta(\hat{\xi} - \hat{\xi}_r) \\ &= r(\hat{\xi}' \cdot \hat{n})\, \delta\big(\hat{\xi} - \hat{\xi}' + 2\,(\hat{\xi}' \cdot \hat{n})\, \hat{n}\big) , \end{aligned} \tag{4.25}$$

for the case of a level air-water surface. Here $\hat{\xi}' \in \Xi_d$ and $\hat{\xi} \in \Xi_u$, and $\delta(\hat{\xi} - \hat{\xi}_r)$ is the Dirac delta function defined in Eq. (1.15); it picks out only that direction $\hat{\xi}$ for which $\hat{\xi} = \hat{\xi}_r$. Recall that $r(\hat{\xi}' \cdot \hat{i}_1$ is dimensionless and

that $\delta(\hat{\xi} - \hat{\xi}_r)$ has units of sr^{-1}; thus $r(a,w;\hat{\xi}' \rightarrow \hat{\xi})$ has units of sr^{-1}, as required. The water-incident radiance reflection function $r(w,a;\hat{\xi}' \rightarrow \hat{\xi})$ has the same form as Eq. (4.25). However, in the air-incident case, $r(\hat{\xi}' \cdot \hat{n})$ is evaluated using the θ_t of Eq. (4.10b), whereas in the water-incident case θ_t is given by Eq. (4.13b). Thus a *reciprocity* relation holds for $r(\hat{\xi}' \cdot \hat{n})$: if $\hat{\xi}_r$ and $\hat{\xi}_t$ are the reflected and transmitted daughter rays of $\hat{\xi}'$, then $r(-\hat{\xi}_r \cdot \hat{n}) = r(\hat{\xi}' \cdot \hat{n})$ and $t(-\hat{\xi}_t \cdot \hat{n}) = t(\hat{\xi}' \cdot \hat{n})$, where $t(\hat{\xi}' \cdot \hat{n}) = 1 - r(\hat{\xi}' \cdot \hat{n})$ is the fraction of photons transmitted by the surface. These reciprocity relations for rays crossing the air-water surface are specific examples of general relations that hold true whenever the direction of photon travel is reversed. Such relations are the foundation of very powerful techniques (namely backward Monte Carlo methods) for solving radiative transfer problems; these matters will be discussed in Section 6.2.

Let us now apply the n^2 law for radiance to the air-water surface, with medium 1 as the air ($n_1 = 1$) and medium 2 as the water ($n_2 = n_w$). Then Eq. (4.21b) can be written as

$$L_w = L_a \, t(\hat{\xi}_a \cdot \hat{n}) \, n_w^2 , \tag{4.26}$$

for transmission from air to water. For the case of transmission from water to air, Eq. (4.21b) yields

$$L_a = L_w \, t(\hat{\xi}_w \cdot \hat{n}) \, \frac{1}{n_w^2} . \tag{4.27}$$

Since the $t(\hat{\xi}_a \cdot \hat{n}) n_w^2$ factor in Eq. (4.26) is precisely the function that transmits radiance L_a through the water surface to give L_w, this equation implies that the air-incident radiance transmittance function for a level surface can be written as

$$t(a,w;\hat{\xi}' \rightarrow \hat{\xi}) = t(\hat{\xi}' \cdot \hat{n}) \, n_w^2 \, \delta(\hat{\xi} - \hat{\xi}_t) . \tag{4.28}$$

In this equation, $t(\hat{\xi}' \cdot \hat{n}) = 1 - r(\hat{\xi}' \cdot \hat{n})$, where $r(\hat{\xi}' \cdot \hat{n})$ is given by Fresnel's formula (4.14), and $\hat{\xi}_t$ is given by the law of refraction (4.9b). In a similar fashion, Eq. (4.27) yields the water-incident radiance transmittance function:

$$t(w,a;\hat{\xi}' \rightarrow \hat{\xi}) = t(\hat{\xi}' \cdot \hat{n}) \, \frac{1}{n_w^2} \, \delta(\hat{\xi} - \hat{\xi}_t) , \tag{4.29}$$

where now $\hat{\xi}'$ and $\hat{\xi}$ are in Ξ_u, and $\hat{\xi}_t$ is given by Eq. (4.12b). The radiance reflectance and transmittance functions are now in a form suitable for use in the interaction principles (4.3) and (4.4).

As a simple example of the use of these transfer functions, let us explicitly evaluate the *irradiance* transfer function $r(a,w)$ for the special case of a level surface and a collimated radiance distribution. Air-incident radiance collimated in direction $\hat{\boldsymbol{\xi}}_o$ can be written as

$$\begin{aligned} L(a;\hat{\boldsymbol{\xi}}') &= E_{\perp}(a)\,\delta(\hat{\boldsymbol{\xi}}' - \hat{\boldsymbol{\xi}}_o) \\ &= \frac{E_d(a)}{|\cos\theta_o|}\,\delta(\hat{\boldsymbol{\xi}}' - \hat{\boldsymbol{\xi}}_o)\,, \end{aligned} \tag{4.30}$$

where $E_{\perp}$ is the plane irradiance on a surface perpendicular to $\hat{\boldsymbol{\xi}}_o$; $E_d = E_{\perp}|\cos\theta_o|$ is then the plane irradiance relative to $\hat{\boldsymbol{i}}_3$. Now by Eq. (4.7b),

$$r(a,w) = \frac{1}{E_d(a)} \int_{\Xi_u} \left[\int_{\Xi_d} L(a;\hat{\boldsymbol{\xi}}')\, r(a,w;\hat{\boldsymbol{\xi}}' \to \hat{\boldsymbol{\xi}})\, d\Omega(\hat{\boldsymbol{\xi}}') \right] |\hat{\boldsymbol{\xi}}\cdot\hat{\boldsymbol{i}}_3|\, d\Omega(\hat{\boldsymbol{\xi}})\,.$$

Substitution for $L(a;\hat{\boldsymbol{\xi}}')$ from Eq. (4.30) and for $r(a,w;\hat{\boldsymbol{\xi}}' \to \hat{\boldsymbol{\xi}})$ from Eq. (4.25) gives

$$r(a,w) = \frac{1}{E_d(a)} \int_{\Xi_u} \left[\int_{\Xi_d} \frac{E_d(a)}{|\cos\theta_o|}\, \delta(\hat{\boldsymbol{\xi}}' - \hat{\boldsymbol{\xi}}_o)\, r(\hat{\boldsymbol{\xi}}'\cdot\hat{\boldsymbol{n}})\, \delta(\hat{\boldsymbol{\xi}} - \hat{\boldsymbol{\xi}}_r)\, d\Omega(\hat{\boldsymbol{\xi}}') \right] |\hat{\boldsymbol{\xi}}\cdot\hat{\boldsymbol{i}}_3|\, d\Omega(\hat{\boldsymbol{\xi}})\,.$$

The integral over $\hat{\boldsymbol{\xi}}' \in \Xi_d$ is nonzero only when $\hat{\boldsymbol{\xi}}' = \hat{\boldsymbol{\xi}}_o$, thus

$$r(a,w) = \frac{1}{|\cos\theta_o|}\, r(\hat{\boldsymbol{\xi}}_o\cdot\hat{\boldsymbol{n}}) \int_{\Xi_u} |\hat{\boldsymbol{\xi}}\cdot\hat{\boldsymbol{i}}_3|\, \delta(\hat{\boldsymbol{\xi}} - \hat{\boldsymbol{\xi}}_r)\, d\Omega(\hat{\boldsymbol{\xi}})\,.$$

The $\hat{\boldsymbol{\xi}}$ integral is nonzero only for $\hat{\boldsymbol{\xi}} = \hat{\boldsymbol{\xi}}_r$, the direction of reflection corresponding to $\hat{\boldsymbol{\xi}}_o$, and we get

$$r(a,w) = \frac{1}{|\cos\theta_o|}\, r(\hat{\boldsymbol{\xi}}_o\cdot\hat{\boldsymbol{n}})\, |\hat{\boldsymbol{\xi}}_r\cdot\hat{\boldsymbol{i}}_3|\,.$$

But $|\hat{\boldsymbol{\xi}}_r\cdot\hat{\boldsymbol{i}}_3| = |\cos\theta_r| = |\cos\theta_o|$, and we are left with just

$$r(a,w) = r(\hat{\boldsymbol{\xi}}_o\cdot\hat{\boldsymbol{n}})\,.$$

Thus for the special case of a collimated incident radiance distribution and a level air-water surface, the irradiance reflectance function $r(a,w)$ is just the Fresnel reflectance of the surface, $r(\hat{\boldsymbol{\xi}}_o\cdot\hat{\boldsymbol{n}})$, as given by Eq. (4.14).

Such a simple result is not obtained for other distributions of incident radiance or for wind-blown water surfaces. In order to evaluate the

various radiance and irradiance transfer functions for other incident radiance distributions and sea states, we must resort to numerical methods.

Conservation of energy

Radiant energy in the form of a narrow ray in direction $\hat{\xi}'$ incident on a level water surface produces on the surface an irradiance E_i'. This incident irradiance E_i' is partly reflected and partly transmitted to form two new streams of irradiance E_r and E_t, respectively of magnitudes

$$E_r = E_i' r(\hat{\xi}' \cdot \hat{i}_3) \quad \text{and} \quad E_t = E_i' t(\hat{\xi}' \cdot \hat{i}_3) . \tag{4.31}$$

Because $t(\hat{\xi}' \cdot \hat{i}_3) = 1 - r(\hat{\xi}' \cdot \hat{i}_3)$, always, it is clear that conservation of radiant energy across the surface holds at the point of incidence: $E_r + E_t = E_i'$. It is also clear that, by construction, this relation holds at any point of a locally plane (but otherwise arbitrarily structured) air-water surface. This fact will be used repeatedly (and implicitly) in the ray-tracing procedures below.

It is clear from Eq. (4.31) that the transmitted irradiance just below the water surface, $E_d(w)$, is always less than the irradiance $E_d(a)$ that produced $E_d(w)$, since some of the incident irradiance is always reflected by the surface[1]. The same is *not* true for radiance. Thus $L(w;\hat{\xi})$, $\hat{\xi} \in \Xi_d$, can be *greater* in magnitude than $L(a;\hat{\xi}')$, $\hat{\xi}' \in \Xi_d$, which produced it. This behavior is a simple consequence of geometric optics and the definition of radiance as power per unit area *per unit solid angle.* In passing from the air into the water, a ray of solid angle $\Delta\Omega_a(\hat{\xi}')$, used to define $L(a,\hat{\xi}')$, "contracts" to a ray with solid angle

$$\Delta\Omega_w(\hat{\xi}) = \frac{1}{n_w^2} \frac{\cos\theta'}{\cos\theta_t} \Delta\Omega_a(\hat{\xi}') ,$$

as can be seen from Straubel's invariant (4.17). Since $\Delta\Omega_w(\hat{\xi})$ is the solid angle used in the definition (or measurement) of $L(w;\hat{\xi})$, the magnitude of $L(w;\hat{\xi})$ can be either greater or less than $L(a;\hat{\xi}')$. Numerical values can be

---

[1]In this statement we are considering *only* the contribution to $E_d(w)$ made by irradiance transmitted through the surface. The value of $E_d(w)$ as *measured* in a water body also contains a contribution by upwelling light that has been reflected back downward by the water surface; recall Eq. (4.6). In special circumstances, the *total* $E_d(w)$ can exceed $E_d(a)$; see Mobley, *et al.* (1993) for an example of this situation.

obtained from the n^2 law for radiance. Consider the case of normal incidence, $\theta' = 0$, and water for which $n_w = 1.34$. Then from Eq. (4.21b) we get

$$L(w;\hat{\xi}_t) = t(\hat{\xi}'\cdot\hat{n})\, n_w^2\, L(a;\hat{\xi}')$$

$$\approx 0.98\,(1.34)^2\, L(a;\hat{\xi}') \approx 1.76\, L(a;\hat{\xi}')\,.$$

This increase in radiance in a particular direction in no way violates conservation of energy, which results from an integral of the radiance over all directions.

4.3 Capillary Waves

The level surface was easily treated using analytical mathematics. For example, the four radiance reflectance and transmission functions needed in Eqs. (4.3) and (4.4) were evaluated using only the Fresnel reflectance formula and the Dirac delta function. However, we are unable to provide a corresponding analytical treatment of even the simplest wind-blown surface (although a number of analytical results pertaining to random air-water surfaces are found in *H.O. VI*, Sections 12.10-12.14). We therefore are forced to seek recourse in numerical techniques. In the following sections we present some Monte Carlo procedures that have proved useful for estimating needed quantities such as the radiance reflectance and transmittance functions of Eqs. (4.3) and (4.4), and their irradiance counterparts of Eqs. (4.5) and (4.6). Along with these numerical techniques, we shall discuss various numerically obtained results, and thereby gain further insight into radiative transfer across air-water surfaces.

Monte Carlo methods comprise a large collection of mathematical techniques for statistically estimating the solution of a given problem by repeated random simulations of the process under investigation. In the problem at hand, we first construct a mathematical representation of a random, wind-blown, air-water surface. We then simulate light rays and trace their interactions with the random water surface. By repeating this process many times, we eventually obtain an acceptably accurate statistical description of how real light interacts with real water surfaces, i.e. we obtain statistical estimates of the surface reflectance and transmittance functions. Several general references on Monte Carlo methods are given at the end of Chapter 6.

The time-averaged optical characteristics of wind-ruffled water surfaces are determined primarily by capillary waves, so long as the surface

remains free of whitecaps. For this reason we shall concentrate on the numerical treatment of a water surface that is covered by wind-induced capillary waves, but which is otherwise horizontal. The numerical techniques developed for capillary waves are equally capable of modeling a full gravity-wave spectrum, or a spectrum of mixed gravity and capillary waves. The price of added realism in the numerical simulation lies mostly increased computer costs, rather than in additional intellectual effort.

We begin our numerical discussions by learning how to construct a random ensemble of water surfaces comprising capillary waves. Once a realization of a water surface is available, we can proceed to trace rays of incident photons as they are reflected and refracted by the (numerically simulated) water surface. Careful tally of the fates of these reflected and refracted rays allows the computation of the desired reflectance and transmittance functions. Thus we are attempting to simulate those processes in nature whereby countless individual photons interact with a random air-water surface, and in combination lead to the macroscopic quantities of radiative transfer.

The present computations leading to the desired optical properties of a wind-roughened water surface fall into five main stages:

(i) construction of a realization of the random air-water surface,

(ii) tracing incident parent light rays over, under, and through the realized surface toward their ultimate destinations,

(iii) assigning radiant energy content to each processed daughter ray,

(iv) storing daughter rays (that proliferate owing to multiple scattering of the parent ray) to await further processing, as in (ii) and (iii), and

(v) accumulating the assigned ray energies of the daughter rays to obtain the associated reflectance and transmittance properties of the random surface.

Stage (i) is described in this section. Stages (ii)-(iv) are discussed in Section 4.4, and stage (v) is treated in Section 4.5. A full treatment of the mathematical details can be found in Preisendorfer and Mobley (1985).

Wave-slope wind-speed law

Consider a wind blowing across a water surface and momentarily maintaining a set of capillary waves. At a fixed horizontal position, the water surface elevation η changes erratically in time because of the passing

waves. The nondimensional *upwind* (or *alongwind*) and *crosswind slopes* of the water surface are

$$\eta_u \equiv \frac{\partial \eta}{\partial x_1} \qquad \text{and} \qquad \eta_c \equiv \frac{\partial \eta}{\partial x_2},$$

respectively, where x_1 and x_2 are the horizontal coordinates of Fig. 4.1. It is known from experiment that the capillary wave slopes η_u and η_c vary in a random manner, being independently and normally distributed with zero mean and variances

$$\begin{aligned} \sigma_u^2 &= a_u U, \quad \text{where} \quad a_u = 3.16\times10^{-3}\ \text{s m}^{-1}, \\ \sigma_c^2 &= a_c U, \quad \text{where} \quad a_c = 1.92\times10^{-3}\ \text{s m}^{-1}, \end{aligned} \tag{4.32}$$

and where U is the wind speed in meters per second measured at an anemometer height of 12.5 m above mean sea level. Equation (4.32) is a statement of the *wave-slope wind-speed law* of capillary waves [see Supplementary Note 5].

The wave elevation η is also distributed normally with zero mean and variance

$$\sigma_\eta^2 = a_\eta U^q. \tag{4.33}$$

The values of a_η and q are left unspecified, since they will not be needed.

The wave-slope wind-speed law (4.32) was first deduced by Duntley (1952, 1954), and by Cox and Munk (1954a, b). Duntley determined wave-slope distributions by *in-situ* electrical measurements; Cox and Munk used light reflected from the water surface to deduce the wave-slope statistics. Their studies were dual and complementary: Duntley found the wave-slope wind-speed law from wave-slope time series obtained at a single point in space, whereas Cox and Munk found the same law from a spatially extensive glitter pattern photographed at one point in time (see *H.O. VI*, p. 145-152). This agreement of results is an example of *ergodic equivalence*, which states that for (most) stationary random processes, a time series taken at a given point yields the same information as spatially extensive data taken at a given time. We shall use this equivalence in our Monte Carlo simulations below.

Constructing a surface realization ▌▌ See Note

This is our first encounter with a *barred heading*, which tells the reader that the following discussion deals primarily with numerical techniques. In the present instance, we are beginning to learn how the wave-slope wind-speed law (4.32) can be used to construct a numerical model of a capillary-wave surface. This model is the foundation of various

algorithms that eventually yield estimates of the reflectance and transmittance functions seen in Eqs. (4.3)-(4.6).

For the computation of photon paths through a random water surface, to be described in the next section, we need to construct a large number of random capillary-wave surfaces. Figure 4.6 shows a portion of the mean-sea-level plane partitioned into a hexagonal grid of congruent isosceles triangles, called *triads.* The dimensions and orientation of one triad are shown in the inset of Fig. 4.6; the vertices of the triad are labeled v_1, v_2, v_3. The δ-dimension is aligned along the wind direction, while the opposite vertex may be as shown, or as reflected in the δ-base.

Now randomly draw three numbers η_1, η_2, η_3 (with units of meters) from $N(0,\sigma^2)$, a normal population of zero mean and variance σ^2 [that will be determined below; see Eq. (4.39)]. Draw three vertical lines (parallel to $\hat{\boldsymbol{i}}_3$) through the vertices of the triad and mark off in turn the lengths η_1, η_2, η_3 on each of the three lines starting from the vertices v_1, v_2, v_3, respectively, at mean sea level; this is illustrated for vertices v_2 and v_3 in Fig. 4.6. Since we have chosen to measure depth as positive downward, positive η_j's correspond to points below mean sea level, negative η_j's to points above

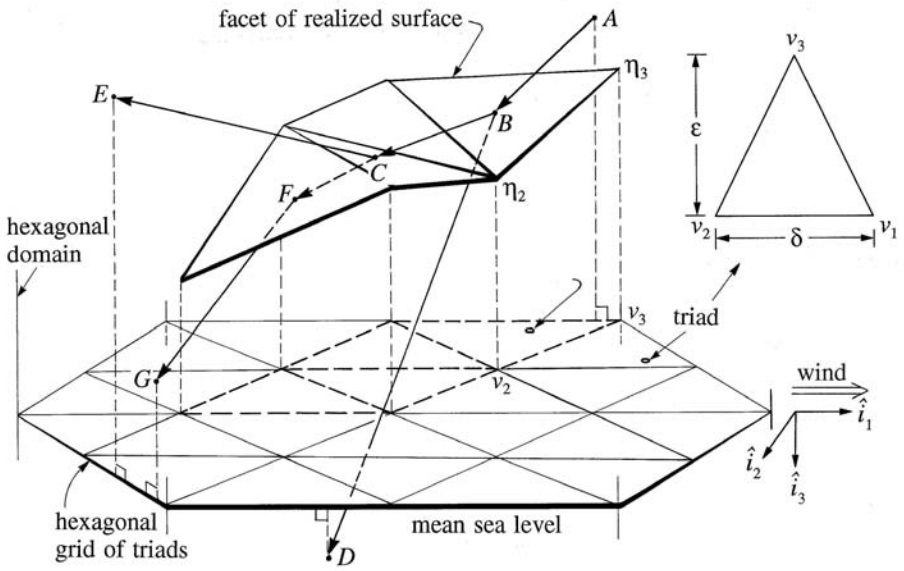

Fig. 4.6. Model of the sea surface as a hexagonal grid of triangular wave facets. A sequence of reflected and refracted rays is illustrated for a particular realization of the random sea surface.

mean sea level (the case illustrated in Fig. 4.6). Connect the three points so found to form a *facet* of the surface. Complete the realized surface by constructing all facets above or below the hexagonal grid. Note that only the first facet constructed requires the drawing of three random numbers; subsequent facets are defined by drawing only one number η_j and using it to determine the remaining unspecified vertex height of a neighboring facet. Four such facets are shown above the hexagonal grid of Fig. 4.6. The hexagonal grid may be thought of as covering a small patch of the ocean surface; the facets represent individual capillary wave faces.

After a wave facet has been defined for each triad in the hexagonal grid, we have one *realization* of a random capillary wave surface. Repeating the process, starting with a new seed for a random number generator, yields another, different realization of the random surface. In this manner we can generate an *ensemble* (or collection) of realizations of a random capillary wave surface.

By construction as just described, the upwind and crosswind slopes of a facet (with vertices numbered as in the inset of Fig. 4.6) are given by

$$\eta_u = \frac{\eta_1 - \eta_2}{\delta} \quad \text{and} \quad \eta_c = \frac{\eta_3 - \frac{1}{2}(\eta_1 + \eta_2)}{\epsilon}. \tag{4.34}$$

Let $\mathscr{E}\{\cdot\}$ denote an *ensemble average*, i.e. the average of the quantity in braces over all the realizations in the ensemble. Then by construction

$$\mathscr{E}\{\eta_j\} = 0 \quad \text{and} \quad \mathscr{E}\{\eta_i \eta_j\} = \sigma^2 \delta_{i-j},$$

for $i, j = 1, 2, 3$. Here δ_{i-j} is the Kronecker delta symbol defined in Eq. (1.19). Similarly, it follows that η_u and η_c are normally distributed with variances

$$\sigma_u^2 = \mathscr{E}\{\eta_u^2\} = \frac{2\sigma^2}{\delta^2} \quad \text{and} \quad \sigma_c^2 = \mathscr{E}\{\eta_c^2\} = \frac{3\sigma^2}{2\epsilon^2}, \tag{4.35}$$

and that η_u and η_c are uncorrelated: $\mathscr{E}\{\eta_u \eta_c\} = 0$.

The *elevation* of a wave facet is defined as

$$\eta = \frac{\eta_1 + \eta_2 + \eta_3}{3}.$$

Thus η is the vertical displacement (in meters) of the facet's centroid above or below the plane of the hexagonal grid. This η is a normally distributed variate of zero mean and variance

$$\sigma_\eta^2 = \mathscr{E}\{\eta^2\} = \frac{\sigma^2}{3}. \tag{4.36}$$

Fixing scales

We may now fix the horizontal sizes δ and ϵ, and the vertical scale σ, of the random wave facets as a function of wind speed U. From Eqs. (4.32), (4.33), (4.35) and (4.36) we have

$$\delta^2 = \frac{6\,a_\eta}{a_u}\,U^{q-1} \quad \text{and} \quad \epsilon^2 = \frac{9\,a_\eta}{2\,a_c}\,U^{q-1}, \tag{4.37}$$

from which

$$\frac{\epsilon^2}{\delta^2} = \frac{3\,a_u}{4\,a_c}. \tag{4.38a}$$

This means that the *shape* of a triad is independent of the wind speed and of the physical units of δ and ϵ. Moreover, by Eqs. (4.32) and (4.35),

$$\sigma^2 = \tfrac{1}{2}\,a_u\,\delta^2\,U. \tag{4.38b}$$

Thus only the vertical scale of the capillary surface changes with wind speed (i.e. the surface becomes more choppy as U increases).

For the purposes of numerical ray tracing, only the relative orientations of the facets are important, and we are free to choose $\delta = 1$, say. This then fixes ϵ and σ by Eq. (4.38). We shall therefore work with

$$\delta = 1, \quad \epsilon = \delta\left(\frac{3\,a_u}{4\,a_c}\right)^{1/2}, \quad \text{and } \sigma = \delta\left(\frac{a_u}{2}\,U\right)^{1/2}. \tag{4.39}$$

The probability distribution of wave slopes

A random water surface built over the hexagonal grid of Fig. 4.6 in the manner described above, using triad geometry defined by Eq. (4.39), will by construction obey the wave-slope wind-speed law (4.32) of capillary waves. In other words, the resultant population of alongwind and crosswind slopes of the realized air-water surfaces will then follow the two-dimensional normal distribution

$$p(\eta_u, \eta_c) = \frac{1}{2\pi\,\sigma_u\,\sigma_c}\exp\left[-\frac{1}{2}\left(\frac{\eta_u^2}{\sigma_u^2} + \frac{\eta_c^2}{\sigma_c^2}\right)\right]. \tag{4.40}$$

The connection between η_u, η_c and the outward (or upward) normal $\hat{\boldsymbol{n}}$ to a triangular wave facet is

$$\hat{\boldsymbol{n}} = -\frac{1}{\left(1 + \eta_u^2 + \eta_c^2\right)^{1/2}}\left(\eta_u \hat{\boldsymbol{i}}_1 + \eta_c \hat{\boldsymbol{i}}_2 + \hat{\boldsymbol{i}}_3\right), \tag{4.41}$$

where $\hat{\boldsymbol{i}}_1$, $\hat{\boldsymbol{i}}_2$, and $\hat{\boldsymbol{i}}_3$ are as shown in Figs. (4.1) and (4.6). Note that Eq. (4.41) reduces to $\hat{\boldsymbol{n}} = -\hat{\boldsymbol{i}}_3$ for a level surface.

Symmetries of the air-water surface

Observe that by systematically changing the signs of η_u and η_c, we can obtain four orientations of $\hat{\boldsymbol{n}}$ with the same value of the probability density. Thus $p(\eta_u,\eta_c)$ has symmetries which, for later reference, we spell out in analytic form.

Recall from Eq. (1.10) that the unit vector $\hat{\boldsymbol{\xi}} = (\xi_1, \xi_2, \xi_3)$ has components $\xi_1 = (1 - \mu^2)^{1/2}\cos\phi$, $\xi_2 = (1 - \mu^2)^{1/2}\sin\phi$, and $\xi_3 = \mu$ in our wind-oriented coordinate system. If a downward directed light ray $\hat{\boldsymbol{\xi}}'$ is reflected by a wave facet into the upward direction $\hat{\boldsymbol{\xi}}$, then from geometrical optics the wave facet must have alongwind and crosswind slopes at the point of reflection given by (Preisendorfer and Mobley, 1985):

$$\eta_u = -\frac{\xi_1 - \xi_1'}{\xi_3 - \xi_3'} \quad \text{and} \quad \eta_c = -\frac{\xi_2 - \xi_2'}{\xi_3 - \xi_3'}.$$

Thus the argument of the exponential in Eq. (4.40) can be written

$$\frac{\eta_u^2}{\sigma_u^2} + \frac{\eta_c^2}{\sigma_c^2} = \frac{1}{(\mu - \mu')^2}\left[(1 - \mu^2)\left(\frac{\cos^2\phi}{\sigma_u^2} + \frac{\sin^2\phi}{\sigma_c^2}\right) + (1 - \mu'^2)\left(\frac{\cos^2\phi'}{\sigma_u^2} + \frac{\sin^2\phi'}{\sigma_c^2}\right)\right.$$

$$\left. - 2(1 - \mu^2)^{1/2}(1 - \mu'^2)^{1/2}\left(\frac{\cos\phi\cos\phi'}{\sigma_u^2} + \frac{\sin\phi\sin\phi'}{\sigma_c^2}\right)\right]$$

$$\equiv q(\mu',\phi';\mu,\phi).$$

This function, by inspection, has the symmetries

$$q(\mu',\phi';\mu,\phi) = q(\mu',2\pi - \phi';\mu,2\pi - \phi) \tag{4.42a}$$

$$= q(\mu',\pi - \phi';\mu,\pi - \phi) \tag{4.42b}$$

$$= q(\mu',\pi + \phi';\mu,\pi + \phi), \tag{4.42c}$$

where $-1 \le \mu, \mu' \le 1$ and $0 \le \phi, \phi' < 2\pi$. This symmetry is that of an ellipse whose axes are parallel to the alongwind and crosswind directions. As we shall see in Section 8.5, the relations expressed in Eq. (4.42) can significantly reduce the numerical effort in calculations of the surface transfer functions of a wind-ruffled water surface.

4.4 Ray Tracing

We now have available a mathematical model of a capillary wave surface. This model reproduces nature to the extent that the slope statistics of the triangular wave facets are identical to the slope statistics (4.32) measured for actual capillary waves. The next step of our computation is to use the realized surfaces to trace the paths of light rays as they intercept the surface, there to be reflected and refracted by the wave facets, eventually leaving the surface region. We can think of these hypothetical light rays as consisting of a stream of photons, each possessing the same properties (direction, energy, etc.), carrying a given amount of energy per unit time, i.e. a certain spectral power. The geometrical factors required to convert the ray power into an irradiance or radiance will be incorporated at the appropriate steps of the ray-tracing algorithm [as for example in Eq. (4.49), below].

Consider once again Fig. 4.6 with its illustration of one realization of the triangular wave facets. These facets, four of which are shown in the figure, are contained in the *hexagonal domain*, the region of space directly above and below the hexagonal grid. A *parent ray* of unit radiant power is shown entering the hexagonal domain at point *A* of Fig. 4.6. Every such initial ray eventually intercepts a surface wave facet, as at *B*. In general, each encounter of a ray with a wave facet generates both a reflected and a refracted daughter ray. From knowledge of the wave facet's orientation, the directions and radiant powers of these daughter rays are determined by Snell's law and Fresnel's formula, respectively, as described in Section 4.2. The daughter rays may undergo further encounters with other wave facets. As illustrated in Fig. 4.6, the first refracted ray at *B* heads downward through the water and leaves the hexagonal domain at *D* without further scattering. The first reflected ray at *B*, however, intercepts another facet at *C*, generating two more rays. The reflected ray starting from *C* leaves the domain at *E*. The refracted ray starting from *C* encounters yet another facet at *F* and undergoes a total internal reflection before leaving the domain at *G*. Thus the initial ray finally results in one reflected and two refracted rays

emerging from the hexagonal domain. The powers at the points of emergence contribute to the appropriate reflectance and transmittance functions.

The computations involved in the ray-tracing require little more than the judicious application of analytic geometry and geometrical optics. In essence the ray-tracing procedure devolves on repeatedly finding the intersection of a straight line and a triangular plane facet in space. The details are rather tedious and need not be repeated here; the algorithms are fully described in Preisendorfer and Mobley (1985).

Figure 4.7 does however give an overview of the entire computational process in the form of a flow diagram of eleven steps. In step 1 of the diagram the computer run is initialized by choosing the wind speed and direction, size of the hexagonal grid, lighting conditions, and the like. In step 2 a realization of the random surface is constructed over the hexagonal grid as in Section 4.3. In step 3 an initial ray incident along the desired direction $\hat{\xi}'$ is specified. This *parent ray* may approach the surface from the air side, as in Fig. 4.6, or from the water side. The parent ray $\hat{\xi}'$ is assigned a radiant power $\Phi' = 1$, and the point $\vec{p}'$ where the ray enters the hexagonal domain (e.g. point *A* of Fig. 4.6) is determined. The information $(\hat{\xi}', \vec{p}', \Phi')$, which fully determines a ray, is then stored in an array, called the *stack*. [In computer jargon, this array is a "push-down, pop-up" or "last-in, first-out" stack.] In step 4 we pull the next available ray triple $(\hat{\xi}, \vec{p}, \Phi)$ from the stack and trace the ray to completion in step 5. That is, in step 5, we extend the ray from point $\vec{p}$ along direction $\hat{\xi}$ until either the surface is encountered or the ray leaves the hexagonal domain. If, in executing step 5, the surface is encountered, the point $\vec{p}_i$ of interception of the ray and the surface is determined (e.g. point *B* in Fig. 4.6), and *daughter rays* (e.g., *BC* and *BD* in Fig. 4.6) are produced. In step 6, one daughter ray is always generated at $\vec{p}_i$ along the reflected direction $\hat{\xi}_r$. In step 7, one daughter ray will be generated along $\hat{\xi}_t$ if and only if the ray is not totally internally reflected at $\vec{p}_i$. (For example, at point *F* in Fig. 4.6, total internal reflection takes place and there is no transmitted daughter ray.) In either of steps 6 or 7, the direction $\hat{\xi}$ of the parent ray (which of course may be a daughter ray from a previous ray-surface interception), the normal $\hat{n}$ to the intercepted wave facet, and the daughter ray direction $\hat{\xi}_r$ determine an associated Fresnel factor for reflectance, as in Eq. (4.14). This factor is multiplied into the current radiant power Φ of the parent ray to obtain the power Φ_r of the reflected daughter ray. The power of the transmitted ray is then $\Phi_t = \Phi - \Phi_r$. The daughter-ray triples are pushed into the stack for further processing. On the other hand, step 5 may fail to produce a point of interception $\vec{p}_i$ (as at *D*, *G*, or *E* of Fig. 4.6). In this

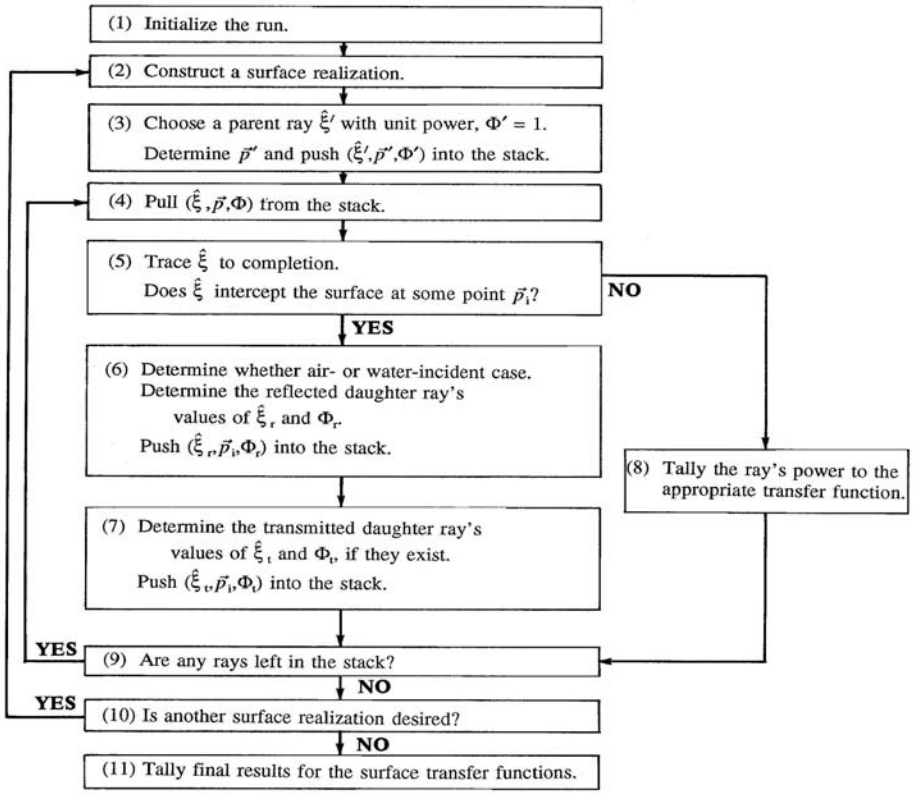

Fig. 4.7. Flow chart of the Monte Carlo ray-tracing procedure for estimating the reflectance and transmittance functions of a wind-blown water surface. [redrawn from Preisendorfer and Mobley (1985)]

case, the ray has finished its interactions with the surface in the hexagonal domain, and its radiant power is added (in step 8) to an accumulating sum for a reflectance or transmittance function, as the case may be.

In practice an initial parent ray may go on to encounter the air-water surface a large number (~10) of times so that, at some stage in the running calculation, several of its daughter ray triples may be simultaneously in the stack awaiting further processing of the kind in step 5 (during which they in turn can generate more daughter ray triples). The pushing activity of steps 3, 6 and 7 places each ray triple in the stack as soon as the ray is

generated. The stack is systematically serviced by the pulling activity of step 4 via step 9. The stack is crucial to the ray tracing algorithm, since it allows the "tree" of *multiply scattered* rays to grow without restrictions on the number of ray-surface interactions or upon the order in which daughter rays are traced to completion. When the stack of waiting ray triples is depleted, we check in step 10 to see if another surface realization is needed. If so, we return to step 2 of the ray-tracing flow diagram and begin anew; otherwise the final results are computed in step 11.

4.5 Irradiance Transfer Functions

We now consider the details of estimating the four irradiance reflectance and transmittance functions $r_{\pm}$ and $t_{\pm}$ of a random air-water surface. These are the functions encountered in the interaction principles (4.5) and (4.6) of Section 4.1, and defined in Eq. (4.7). We shall work with the random capillary surfaces defined in Section 4.3, and perform ray tracing as described in Section 4.4.

Let $S(\omega)$ be the ω^{th} realization of a random capillary-wave surface defined over a hexagonal domain like that of Fig. 4.6; $\omega = 1, ..., S$, where S is the total number of surfaces to be generated. $S(\omega)$ of course depends on the wind speed U, which is held constant. The hexagonal grid is located at the mean water surface, about which the facets of $S(\omega)$ are randomly placed. Parallel to the mean horizontal surface, and just above and below $S(\omega)$ at fixed distances, are two imaginary *horizontal monitoring surfaces* (h.m.s.), which we will use in the derivations below. We now consider two specific examples of how to compute the reflectance of $S(\omega)$ for downward irradiance. On the basis of these examples we can then describe the general recurrence formulas for the reflected and transmitted radiant powers Φ_r and Φ_t needed in steps 6 and 7 of the ray-tracing flow chart of Fig. 4.7.

Examples of ray paths

Consider a narrow unpolarized ray of central direction $\hat{\boldsymbol{\xi}}'$ incident on $S(\omega)$ at point B, as shown in Fig. 4.6. A closeup of this is shown in the upper panel of Fig. 4.8. The ray illuminates a small patch A of outward normal $\hat{\boldsymbol{n}}$ on $S(\omega)$. To define the reflectance of $S(\omega)$ when the surface is highly crinkled, we place an h.m.s. just above $S(\omega)$, as shown. We use the h.m.s. to register the incident radiant power $\Phi(I)$ of the ray as it crosses a small patch I of the h.m.s. on its way to patch A on $S(\omega)$. Clearly $\Phi(A) = \Phi(I)$ by conservation of energy. Now in accordance with Eq. (4.31), a

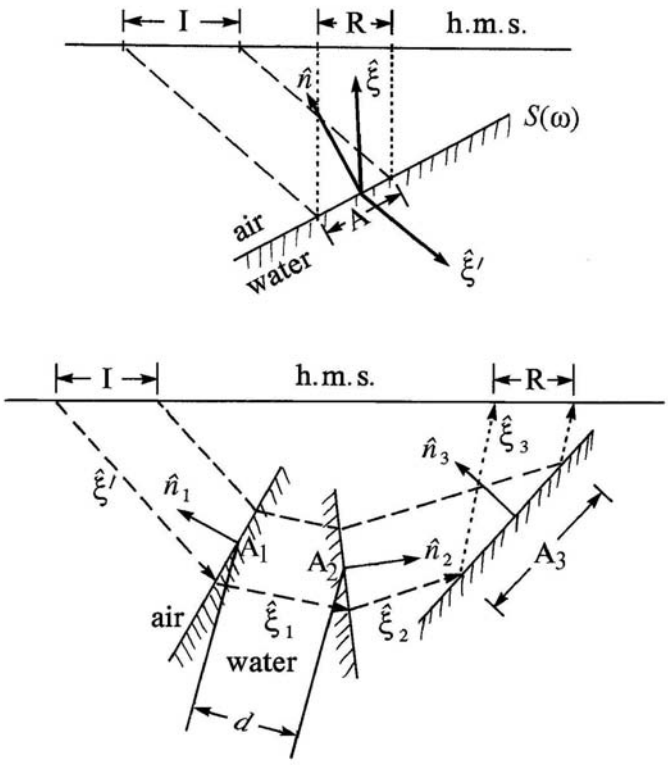

Fig. 4.8. Examples of simple (upper panel) and complex (lower panel) ray paths, and of the use of an upper horizontal monitoring surface (h.m.s.) in computing the irradiance reflectance $r_+ = r(a,w)$. [redrawn from Preisendorfer and Mobley (1985)]

fraction $r(\hat{\xi}'\cdot\hat{n})$ of $\Phi(A)$ is reflected into the direction $\hat{\xi}$ and then streams upward through patch R of the h.m.s. If $\Phi(R)$ is the radiant power of the reflected ray crossing R, then $\Phi(R) = \Phi(A)r(\hat{\xi}'\cdot\hat{n}) = \Phi(I)r(\hat{\xi}'\cdot\hat{n})$.

The *irradiance reflectance* $r_+(\hat{\xi}';\omega)$ relative to this particular ray and surface realization $S(\omega)$ is by definition

$$r_+(\hat{\xi}';\omega) \equiv \frac{\Phi(R)}{\Phi(I)} = r(\hat{\xi}'\cdot\hat{n}) . \tag{4.43}$$

The corresponding irradiance transmittance is, as always,

$$t_+(\hat{\xi}';\omega) \equiv 1 - r_+(\hat{\xi}';\omega) . \tag{4.44}$$

Recall that the notation "r_+" is used to represent $r(a,w)$, as in Eq. (4.7b); the

"+" subscript reminds us that $r_+(\hat{\boldsymbol{\xi}}')$ is a reflectance for rays $\hat{\boldsymbol{\xi}}'$ initially headed downward (the positive direction), i.e. $\hat{\boldsymbol{\xi}}' \in \Xi_d$.

The preceding ideas can be extended to more complicated paths over $S(\omega)$. In the lower panel of Fig. 4.8, an incident ray of unpolarized radiant power $\Phi(I)$ crosses the h.m.s. and illuminates a small patch A_1 with outward normal $\hat{\boldsymbol{n}}_1$, whereupon a refracted daughter ray is born and travels along direction $\hat{\boldsymbol{\xi}}_1$ a distance d underwater to encounter patch A_2 of outward normal $\hat{\boldsymbol{n}}_2$, there to be partially refracted into a new daughter ray along $\hat{\boldsymbol{\xi}}_2$. The final encounter of this particular ray with the water surface is over patch A_3 with outward normal $\hat{\boldsymbol{n}}_3$, from which a new daughter ray proceeds along $\hat{\boldsymbol{\xi}}_3$ toward the h.m.s. and emerges through patch R carrying radiant power $\Phi(R)$. The ratio of this emergent power $\Phi(R)$ to the incident power $\Phi(I)$, i.e., the reflectance of $S(\omega)$ in this path instance, is

$$r_+(\hat{\boldsymbol{\xi}}';\omega) = \frac{\Phi(R)}{\Phi(I)} = t(\hat{\boldsymbol{\xi}}'\cdot\hat{\boldsymbol{n}}_1)\, t(\hat{\boldsymbol{\xi}}_1\cdot\hat{\boldsymbol{n}}_2)\, r(\hat{\boldsymbol{\xi}}_2\cdot\hat{\boldsymbol{n}}_3)\,. \tag{4.45}$$

Note that we have neglected the small amount of attenuation by the water as the ray travels distance d from patch A_1 to A_2.

The general recursive ray path ▌▌

There is clearly an unlimited number of possible daughter paths that can spring from a single incident ray approaching $S(\omega)$ along a given direction $\hat{\boldsymbol{\xi}}'$. Figure 4.9 shows some of these possibilities. We can classify ray configurations by counting the number n_s of scattering points and the number n_b of ray branches (the total number of rays) involved in the scattering event. For air-incident rays, numerical experimentation shows that the three-branch, single-scattering event shown at the upper-left corner of Fig. 4.9 is by far the most common at all wind speeds and angles of incidence. As the wind speed increases, or as the incident rays come in nearly horizontally, then the numbers of scatters and branches increase. For water-incident rays, single-scattering events are also most common. Figure 4.9 shows how these single-scattering events consist of two kinds: the case of $n_s = 1$, $n_b = 2$ when total internal reflection occurs, and the case of $n_s = 1$, $n_b = 3$ when an upwardly transmitted ray is created. For crinkly surfaces, water-incident rays can undergo multiple scattering ($n_s \geq 2$), as indicated in the $n_s = 2$, $n_b = 4$ case of Fig. 4.9. Of the many possible configurations for air-incident multiple scattering, the second-order scatter, five-branch case is the most common, with third-order scatter, seven-branch cases being the

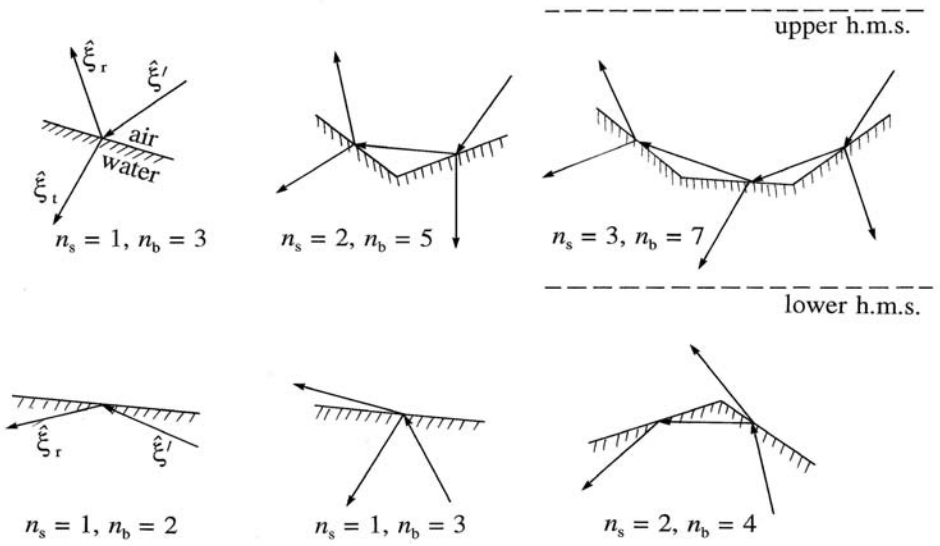

Fig. 4.9. Schematic diagrams of common water-surface scattering events. The order of the scattering is n_s, and n_b is the number of branches (the total number of rays involved in the scattering event). The upper row of diagrams is for air-incident rays, and the lower row is for water-incident rays. [redrawn from Preisendorfer and Mobley (1985)]

next most common. Configurations such as the $n_s = 3$, $n_b = 6$ case shown in Fig. 4.6 are rare, and cases where $n_b \geq 10$ almost never occur.

While it is possible to develop an algebraic notation to explicitly represent the general forms of Eqs. (4.43) or (4.45), it is more expedient in numerical work to simply write down a recursive formula for the radiant power of a newly born daughter ray at each step between the beginning and end of the parent ray's travels; and so we proceed as follows.

Suppose the numerical computation is at step (5) of the ray tracing procedure of Fig. 4.7. We then know the values of $\hat{\boldsymbol{\xi}}$, $\vec{p}$ and Φ defining the parent ray. Tracing the ray from $\vec{p}$ to an interception point $\vec{p}_i$ along $\hat{\boldsymbol{\xi}}$ yields a calculable distance $d = |\vec{p}_i - \vec{p}|$. The outward normal $\hat{n}_i$ to $S(\omega)$ at $\vec{p}_i$ is known from Eqs. (4.34) and (4.41). From $\hat{n}_i$ we can decide (as in Fig. 4.2) whether the path of the ray was in air or in water by finding whether $\hat{\boldsymbol{\xi}} \cdot \hat{n}_i < 0$ (air-incident case) or $\hat{\boldsymbol{\xi}} \cdot \hat{n}_i > 0$ (water-incident case). Note that an air-incident ray can be traveling either downward or upward; examples of each possibility are seen in the $n_s = 3$, $n_b = 7$ case of Fig. 4.9.

The same is true for water-incident rays. The daughter ray directions $\hat{\xi}_r$ and $\hat{\xi}_t$ at $\vec{p}_i$ are then found as in Eqs. (4.9) or (4.12). In the air-incident case the generated daughter rays are defined by

$$(\hat{\xi}_r, \vec{p}_i, \Phi_r), \quad \text{with} \quad \Phi_r = \Phi\, r(\hat{\xi}\cdot\hat{n}_i)\,, \tag{4.46a}$$

for the reflected ray, and

$$(\hat{\xi}_t, \vec{p}_i, \Phi_t)\,, \quad \text{with} \quad \Phi_t = \Phi\, t(\hat{\xi}\cdot\hat{n}_i)\,, \tag{4.46b}$$

for the refracted ray. In the water-incident case the daughter rays are defined in a similar way. In the case of total internal reflection, $r(\hat{\xi}\cdot\hat{n}_i) = 1$ and there is no refracted ray. The daughter ray triples defined by Eqs. (4.46) are immediately pushed into the stack for subsequent processing, as described in steps (6) and (7) of Fig. 4.7.

After the last ray of the last surface realization has been processed, the final tally yields the desired irradiance transfer functions $r_{\pm}(\hat{\xi}')$ and $t_{\pm}(\hat{\xi}')$ of the random surface, for a given wind speed U and incident direction $\hat{\xi}'$ of photons.

Transfer functions as ensemble averages ▌▌

We now interpret statistically the results of the preceding calculations. First, it should be noted that a *single* number such as $r_+(\hat{\xi}';\omega)$, found in Eqs. (4.43) or (4.45) by tracing a single ray, is statistically speaking, rather meaningless. It is only after thousands or even millions of such reflection numbers have been accumulated, and then averaged over ω, that a statistically meaningful result begins to emerge. Thus imagine these reflections to occur independently and in great numbers over the extent of the hexagonal grid for a single realization $S(\omega)$ of the surface. For a sufficiently large number of reflections, the ratio of the total amount of reflected radiant power from a small neighborhood about each point of the horizontal monitoring surface for $S(\omega)$, to the power incident upon the neighborhood, will approach a limit. This limit is the desired irradiance reflectance. By virtue of our construction of $S(\omega)$, this limit will be independent of the horizontal location of the neighborhood on the h.m.s. and will be a weighted average of terms of the kind seen in Eqs. (4.43) and (4.45). By ergodic equivalence, this argument will also go through by applying it to an ensemble of realized surfaces $S(\omega)$ irradiated over a small neighborhood about a fixed common point of their grid. A simple heuristic argument towards this end, using radiometric concepts, will now be

sketched. The argument also provides the basis for the interpretations of $r_+(\hat{\xi}')$.

Let $\Phi(I)$ be the downward incident radiant power over patch I of the upper h.m.s. of a realization $S(\omega)$ of the random water surface (as in the diagrams of Fig. 4.8). This $\Phi(I)$ is produced by a ray of radiance $L(\hat{\xi}')$ about direction $\hat{\xi}' \in \Xi_d$. If $\Delta\Omega$ and ΔA are the solid angle and the area of the ray normal to $\hat{\xi}'$, then

$$\Phi(I) = L(\hat{\xi}')\,\Delta\Omega\,\Delta A\,. \tag{4.47}$$

If $r_+(\hat{\xi}';\omega)$ is the facet reflectance associated with one of the daughter rays initiated by this parent ray, then by Eq. (4.47) the associated upward emergent power $\Phi(R;\omega)$ through the upper h.m.s. of $S(\omega)$ is given by

$$\begin{aligned}\Phi(R;\omega) &= \Phi(I)\, r_+(\hat{\xi}';\omega) \\ &= L(\hat{\xi}')\,\Delta\Omega\,\Delta A\, r_+(\hat{\xi}';\omega)\,.\end{aligned} \tag{4.48}$$

After solving Eq. (4.48) for $r_+(\hat{\xi}';\omega)$, multiplying and dividing by $|\hat{\xi}'\cdot\hat{i}_3|$, and taking the ensemble average we find

$$\mathop{\mathscr{E}}_{\omega}\left\{r_+(\hat{\xi}';\omega)\right\} = \frac{\mathop{\mathscr{E}}_{\omega}\left\{\dfrac{\Phi(R;\omega)}{\left(\dfrac{\Delta A}{|\hat{\xi}'\cdot\hat{i}_3|}\right)}\right\}}{L(\hat{\xi}')\,\Delta\Omega\,|\hat{\xi}'\cdot\hat{i}_3|} \equiv r_+(\hat{\xi}')\,. \tag{4.49}$$

Note that $\Delta A/|\hat{\xi}'\cdot\hat{i}_3|$ is the area of illuminated patch I, which we may assign to the ensemble average of $\Phi(R;\omega)$. Thus we see that the numerator of $r_+(\hat{\xi}')$ in Eq. (4.49) is an average upward radiant emittance (W m^{-2}) of the h.m.s., while the denominator is the downward irradiance (W m^{-2}) on the h.m.s. The value of $r_+(\hat{\xi}')$ in Eq. (4.49) is found in practice as outlined in steps 8 and 11 of Fig. 4.7. The values of $r_-(\hat{\xi}')$ and of $t_\pm(\hat{\xi}')$ are found in a similar way. This practical procedure gives the meaning of the ensemble average over all ω (= 1, ..., S) on the right in Eq. (4.49), and in turn, Eq. (4.49) shows the theoretical basis of steps 8-11 of Fig. 4.7.

The upper and lower horizontal monitoring surfaces have been conceptual aids in the development of Eq. (4.49). Since the random air-water surface is on average flat and horizontal, we may think of the horizontal monitoring surface approaching the mean surface and coalescing with it. Then $r_\pm(\hat{\xi}')$ and $t_\pm(\hat{\xi}')$ can be regarded as functions describing the

optical properties of the mean horizontal surface of a wind-roughened water surface.

4.6 Numerical Examples of Irradiance Transfer

Preisendorfer and Mobley (1986) used the numerical methods described in the preceding sections to study the optical properties of a water surface covered with capillary waves. Numerical experimentation showed that the sampling variability (Monte Carlo fluctuation) in computed $r_{\pm}$ and $t_{\pm}$ values was at most a few percent for ensemble averages based an 3,000 surface realizations (with one parent ray $\hat{\xi}'$ per realization). Most simulations were performed for collimated incident radiance distributions $L(\hat{\xi}')$, i.e. for all $\hat{\xi}'$ exactly the same, which corresponds to an infinitely distant, point sun in a black sky. Simulations performed with a variable $\hat{\xi}'$ corresponding to the finite angular size of the sun agreed with the point-sun simulations to better than one percent, except at high wind speeds (U = 20 m s^{-1}) for nearly horizontal incident rays, in which case the results differed by a few percent.

The results presented below are therefore accurate to within a few percent, *for the assumed sea-state model.* The magnitude of errors due to physical processes not modeled, in particular the presence of whitecaps and gravity waves at higher wind speeds, has not been quantified.

In the figures below, the incident ray direction $\hat{\xi}'$ is specified by (θ_s', ϕ_s'), where θ_s' is the polar angle of the light *source* measured from either the zenith or the nadir direction. Thus $0 \le \theta_s' \le 90°$, and the phrase "air-incident rays" or "water-incident rays" must be added to avoid ambiguity. A source located in the downwind direction has $\phi_s' = 0$.

Some observations on multiple scattering

The phenomenon of multiple scattering is quite difficult to handle in analytic formulations, but is nearly trivial to study when using Monte Carlo ray-tracing procedures. In Fig. 4.9 we defined the order n_s of scattering as the total number of times a parent ray or any of its daughter rays intercepts a wave surface. Figure 4.10 shows, as a function of θ_s' and wind speed, the percentage of incoming rays that undergoes multiple scattering of any order ($n_s \ge 2$). This figure is for incoming rays that are parallel to the wind ($\phi_s' = 0$). The figure is based on over 150,000 ray tracings. The curves are applicable to both air-incident and water-incident rays. Observe that for a given incidence angle θ_s', the percentage of rays undergoing multiple

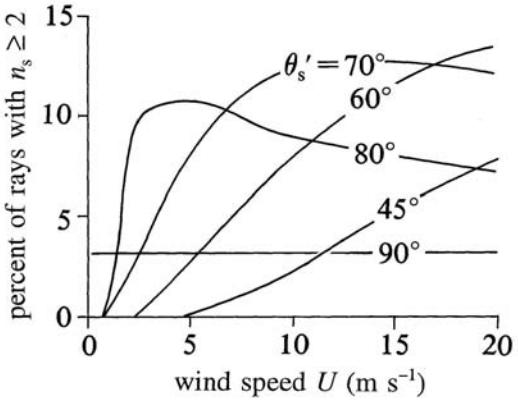

Fig. 4.10. Percentage of incident rays that results in multiple scattering ($n_s \geq 2$) from a capillary wave surface, as a function of wind speed U and source angle θ_s' of the parent rays. [redrawn from Preisendorfer and Mobley (1985)]

scattering generally increases with wind speed U, up to an incident angle of about 70°. Rays incident from within 30° of the zenith or from a similar cone near the nadir almost never have multiple scatters for winds in the range U = 0 to 20 m s^{-1}. We see that for wind speed $U \geq 5$ m s^{-1}, roughly ten percent of the rays incident from the range $60° \leq \theta_s' \leq 80°$ have multiple scatters. This is because the relative angles between the tilted wave facets and the incident rays are then most conducive to reflecting the incident ray into a nearly horizontal direction, so that the reflected daughter ray hits a neighboring facet. There is an overall dropoff in multiple scattering for nearly horizontal incoming rays, since the daughter rays then tend to head away from the surface at angles that cause them, on average, to miss even the nearest facets. The quantitative effects of multiple scattering are seen in the following figures.

Reflectances for capillary waves and collimated sources

Figure 4.11 shows $r_+(\hat{\xi}') = r(a,w;\theta_s',\phi_s')$ as a function of wind speed for selected θ_s' and ϕ_s' values. By the elliptical symmetry of the surface as expressed in Eq. (4.42), it is sufficient to determine $r_+(\theta_s',\phi_s')$ over the range $0° \leq \phi_s' \leq 90°$ for each θ_s'.

Four curves are shown in Fig. 4.11 for each θ_s' value. The solid lines are for the alongwind case, $\phi_s' = 0°$ (or 180°), in which the incoming

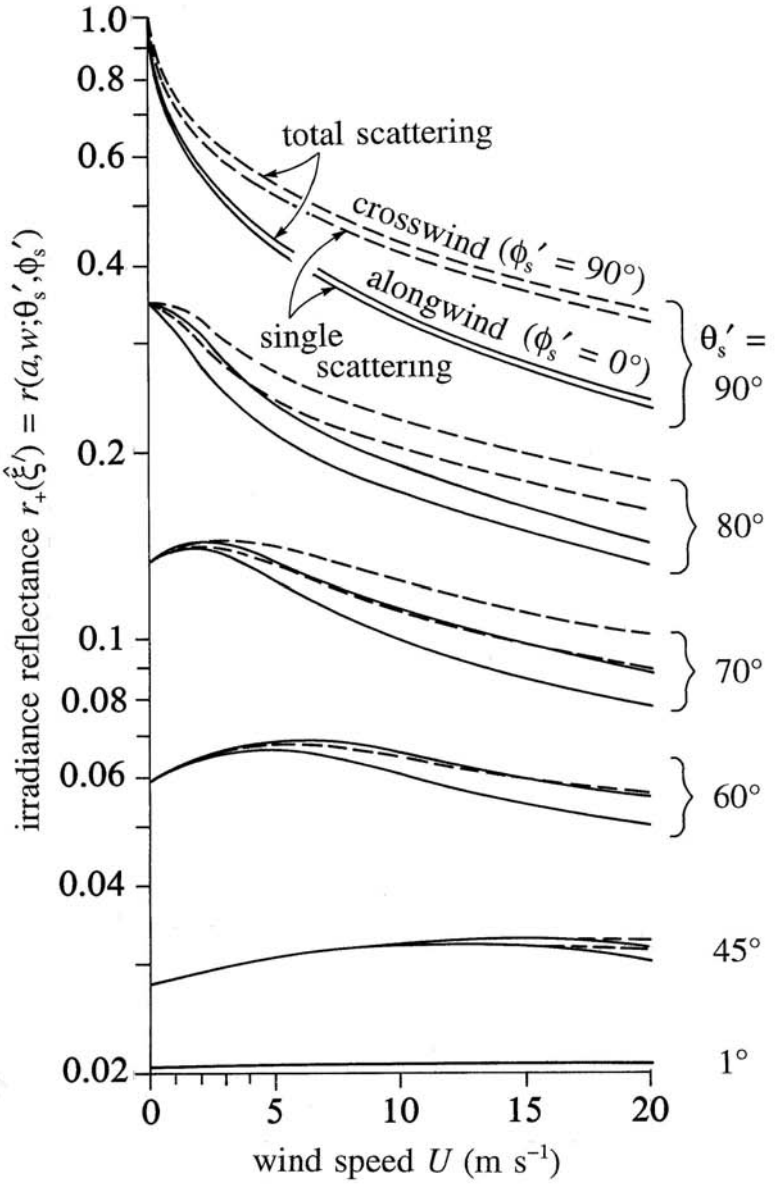

Fig. 4.11. Reflectances $r_+(\hat{\boldsymbol{\xi}}') = r(a,w;\theta_s',\phi_s')$ for random capillary waves and air-incident light rays from distant point sources. For each group of θ_s' curves, the solid lines are for $\phi_s' = 0°$ (light source and wind along the same direction), and the dashed curves are for $\phi_s' = 90°$ (source at right angles to the wind direction). For each pair of solid or pair of dashed curves, the top curve is for total scattering and the bottom curve is for single scattering only. [redrawn from Preisendorfer and Mobley (1985)]

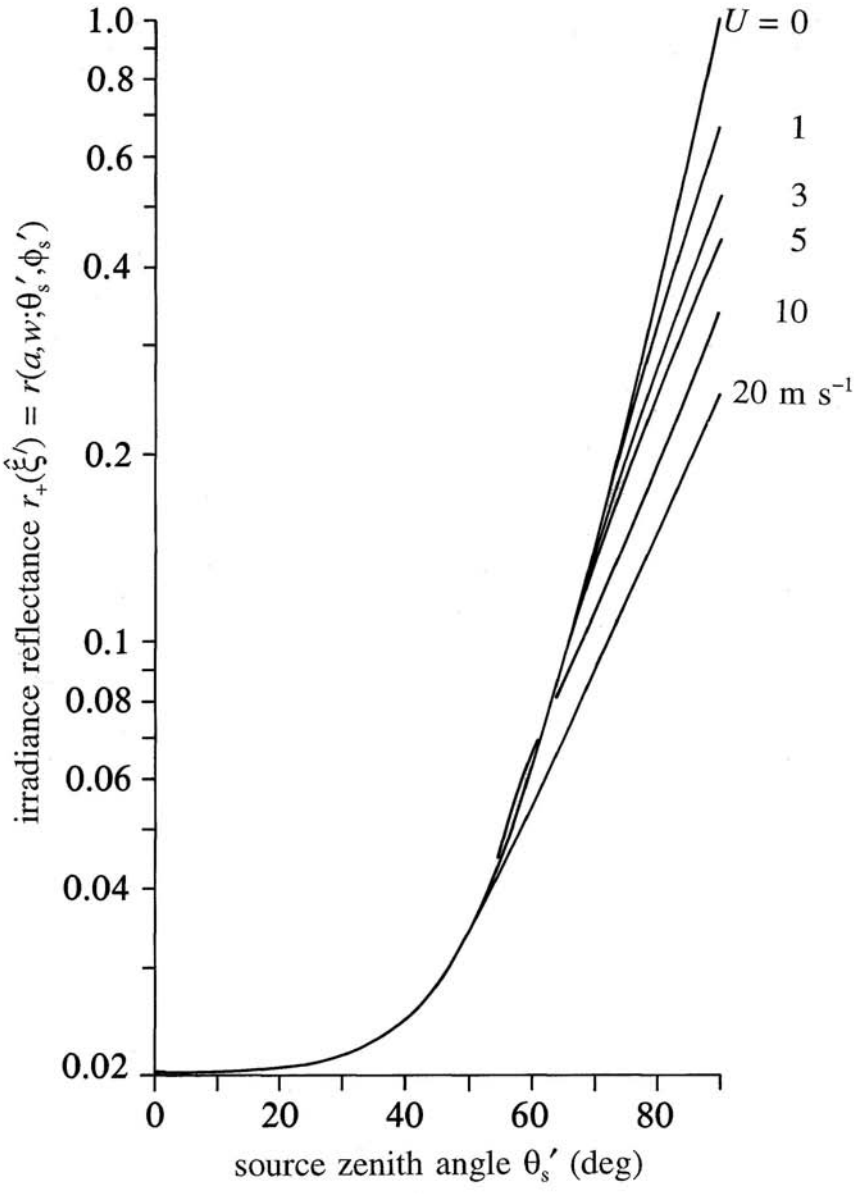

Fig. 4.12. Capillary-wave reflectances $r_+(\hat{\xi}') = r(a,w;\theta_s',\phi_s')$ as a function of wind speed and θ_s', for $\phi_s' = 0°$ and total scattering (replots of the upper solid curve of each solid pair in Fig. 4.11). [redrawn from Preisendorfer and Mobley (1985)]

rays are in the vertical plane parallel to the wind. The dashed lines are for the crosswind case, $\phi_s' = 90°$ (or 270°), in which the incoming rays are in the vertical plane perpendicular to the wind. In the computations, a separate tally was kept for singly-scattered rays, so that the effects of multiple scattering could be isolated. For each pair of solid or dashed curves, the top curve gives the total reflectance computed from all rays and the bottom curve gives the reflectance as computed from singly-scattered rays only. Most points on the curves of Fig. 4.11, above each labeled wind speed, are the average of three separate experiments of 3000 surface realizations per experiment. Spot checks of the accuracy of these curves showed that they are within a few percent of the true values (as defined by an infinite number of surface realizations). For example, for the alongwind total scattering case of $U = 20$ m s^{-1} with $\theta_s' = 60°$, five experiments (of 3000 realizations each) yielded an average $r_+(\hat{\boldsymbol{\xi}}')$ value of 0.05456, with a standard deviation of 0.00053. For the same situation except for $\theta_s' = 80°$, the five-experiment average yielded $r_+(\hat{\boldsymbol{\xi}}') = 0.14045$ with a standard deviation of 0.00128. Two of these standard deviations on each side of the curves will define points that are only slightly more separated than the drawn thickness of the curves. According to standard statistical reasoning, we can be 95% confident that the true mean values lie between these points.

The reflectances for zero wind speed in Fig. 4.11 are just the unpolarized Fresnel reflectance as given by Eq. (4.14) for a horizontal plane surface (the index of refraction used was $n_w = 4/3$) for the given θ_s'. For high solar altitudes (i.e. small θ_s'), the reflectance increases slightly as the wind increases from zero, whereas for low solar altitudes, the reflectance decreases markedly as the wind picks up. This qualitative behavior was predicted by Cox and Munk (1955) from approximate analytic calculations. Figure 4.11 reveals the quantitative features of this behavior, in particular the effects of capillary-wave anisotropy and multiple scattering.

Figure 4.12 reproduces in different form the total scattering curves of Fig. 4.11 for the alongwind case $\phi_s' = 0°$. The curve for $U = 0$ is the Fresnel reflectance for a level surface, as was seen in Fig. 4.3.

A detailed view of the dependence of $r_+(\theta_s', \phi_s')$ on the azimuth angle ϕ_s' of the source relative to the wind direction is shown in Fig. 4.13. This figure gives the total-scattering reflectance at a wind speed of 20 m s^{-1} for capillary waves. Since the wave facets are slightly less tilted, on average, in the crosswind direction than in the alongwind direction [recall that $\sigma_u^2 > \sigma_c^2$ in Eq. (4.32)], rays incident at right angles to the wind see a slightly flatter water surface, and thus have a slightly higher reflectance. This behavior is seen in Fig. 4.13. The dependence is very weak at high sun altitudes, but becomes substantial for incident angles near the horizon.

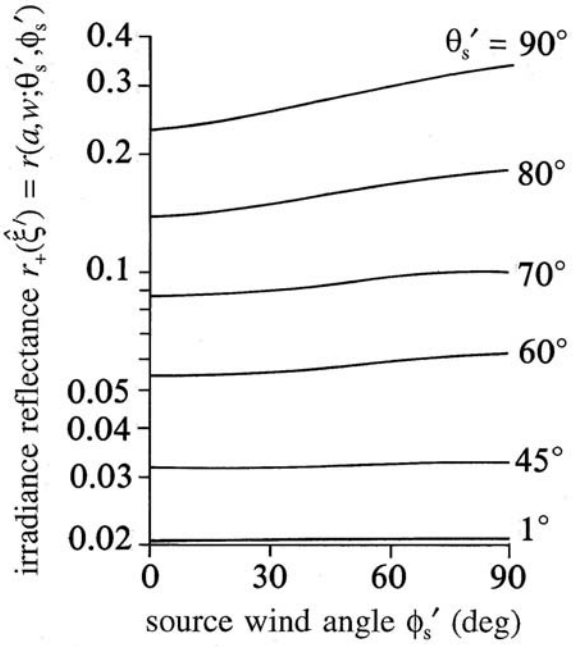

Fig. 4.13. Dependence of the capillary-wave, total-scattering reflectance $r_+(\hat{\xi}')$ = r$(a,w;\theta_s',\phi_s')$ on light source position relative to the wind direction, for a wind speed of $U = 20$ m s^{-1}. [redrawn from Preisendorfer and Mobley (1985)]

The reflectances for an underwater light source, $r_-(\hat{\xi}') = r(w,a;\theta_s',\phi_s')$, are shown in Fig. 4.14. Now θ_s' is measured from the nadir to the source location. The arrangement of the curves (alongwind and crosswind, total and single scattering) is the same as for the air-incident case in Fig. 4.11. However, the curves are markedly different from their counterparts in Fig. 4.11 because of the effects of total internal reflection. For the flat surface at zero wind speed, any water-incident ray with $\theta_s' \geq \sin^{-1}(1/n_w)$ [= 48.59° for n_w = 4/3; recall Eq. (4.13b)] is totally reflected, giving a reflectance of 1. The reflectance increases quite rapidly as this angle is approached, and is constant thereafter from 48.59° to 90°. As soon as the wind increases from $U = 0$, rays incident at $\theta_s' = 48.59°$ begin hitting tilted facets and sometimes experience only partial reflection with daughter rays making it through to the air above; the reflectance then drops sharply for this θ_s' value. Water-incident rays from nearly horizontal directions are almost always totally reflected even at high wind speeds, so $r_-(\hat{\xi}')$ remains close to 1 at these angles. For angles of incidence $\theta_s' \leq 45°$, there is a relatively

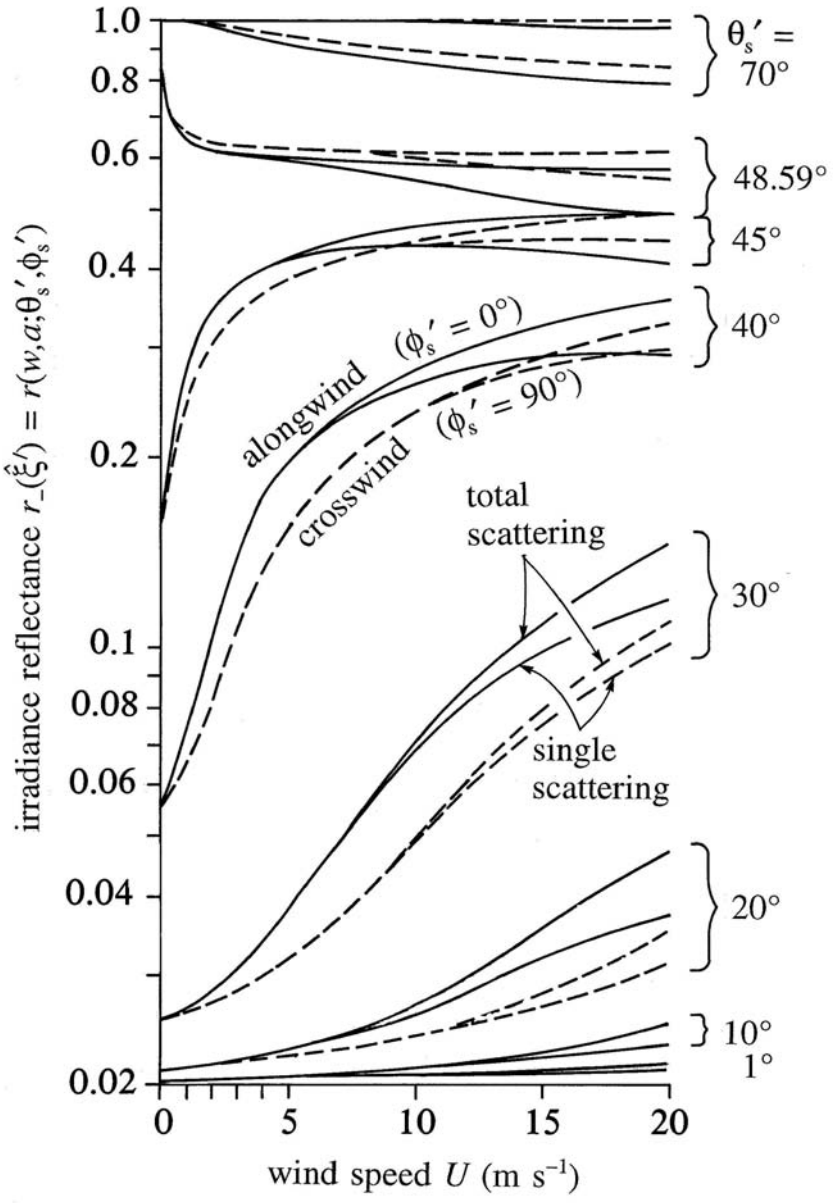

Fig. 4.14. Reflectances $r_{-}(\hat{\boldsymbol{\xi}}') = r(w,a;\theta_s',\phi_s')$ for random capillary waves and for water-incident light rays from distant point sources. θ_s' is measured from the nadir to the source location. The solid- and dashed-line conventions are the same as in Fig. 4.11. [redrawn from Preisendorfer and Mobley (1985)]

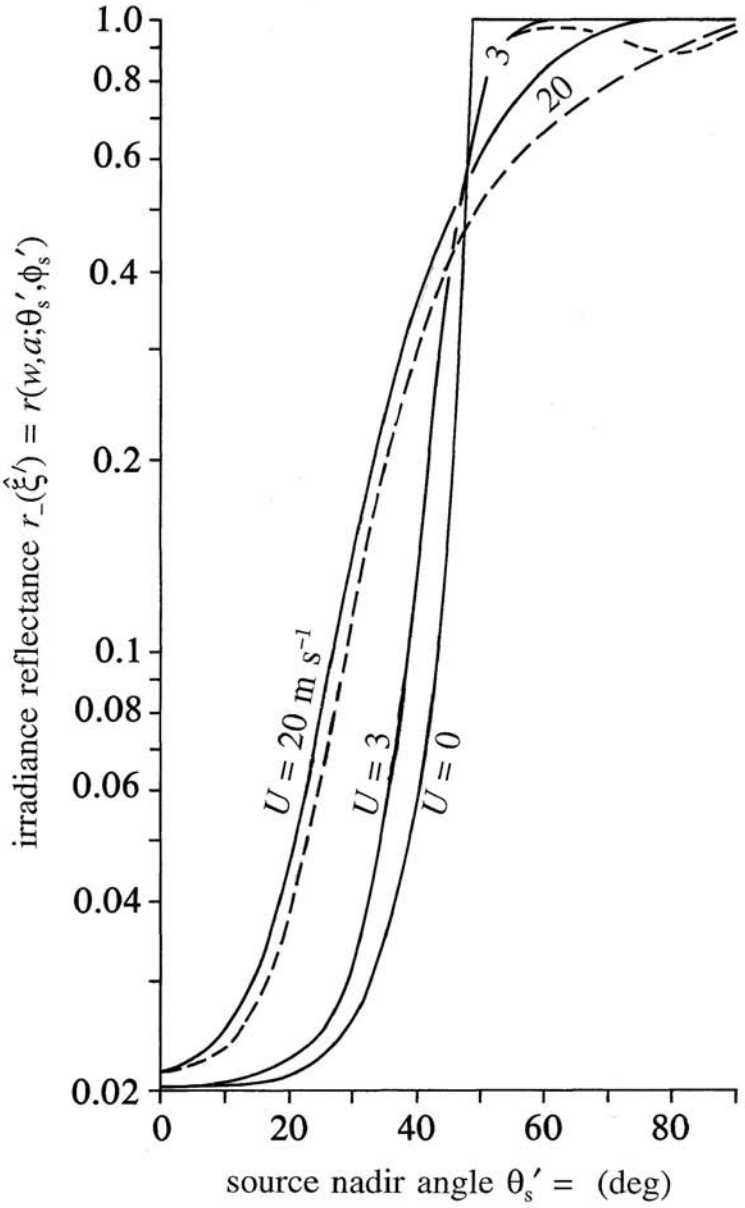

Fig. 4.15 Selected reflectances $r_-(\hat{\xi}') = r(w,a;\theta_s',\phi_s')$ replotted from Fig. 4.14. The solid curves are for the alongwind, total scattering cases for the wind speeds shown. The dashed curve is the single-scattering contribution at U = 20 m s^{-1}. [redrawn from Preisendorfer and Mobley (1985)]

strong dependence on θ_s', compared to the air-incident case of Fig. 4.11. We see that a rising wind speed now causes a rapid increase in the reflectances, with the alongwind values now generally being greater than the crosswind values. Comparing the curves for total and single scattering shows that multiply-scattered rays often make a substantial contribution to the reflectance for water-incident rays.

Figure 4.15 replots selected total-scattering curves (solid) from Fig. 4.14 in order to better show the strong dependence of $r_-(\hat{\xi}')$ on θ_s'. The steep slopes of the total- and single-scattering curves for the 20 m s^{-1} case show the importance of including multiple scattering in the $r_-(\hat{\xi}')$ estimates. The remaining solid curves are for total scattering, alongwind cases for the $U = 3$ m s^{-1} and $U = 0$ wind speeds shown. The $U = 0$ curve is just the Fresnel reflectance seen in Fig. 4.3.

Reflectances for capillary waves and distributed sources

The collimated-source reflectance $r_+(\hat{\xi}')$ is a reasonable approximation to nature for the case of the sun in a very clear sky. Likewise $r_-(\hat{\xi}')$ applies to a collimated, horizontally extensive light source just under the surface ("horizontally extensive" means simply that we are in a plane-parallel geometry). However, in the air-incident case, if the sky is overcast the position of the sun may be indiscernible, so that a horizontally extensive and *directionally diffuse* light source must be used in the calculations. Likewise, the upwelling radiance distribution just below the sea surface is always diffuse in natural water bodies. The reflectance for a diffuse source is in essence a weighted average of the collimated-source reflectances presented above; its value depends upon the exact form of the continuous radiance distribution over the appropriate hemisphere of incident directions. Reflectances for diffuse light sources can be computed with the Monte Carlo ray tracing model simply by allowing the incoming ray directions $\hat{\xi}'$ to be distributed according to the desired radiance distribution. For example, a reflectance for a uniform sky would have $\hat{\xi}'$ values chosen at random such that each point in the dome of the sky is equally likely to be the source direction of the parent ray with initial radiant power $\Phi' = 1$.

An approximate but convenient parameterization for diffuse lighting in nature is the *cardioidal radiance distribution* (*H.O. VI*, p. 21):

$$L(\hat{\xi}_s') \equiv L(\theta_s', \phi_s') = L_o(1 + C\cos\theta_s'), \tag{4.50}$$

where L_o is the radiance of the horizon ($\theta_s' = 90°$), and C is a real number. For the case of a heavy overcast, observations indicate that $C \approx 2$, so that

on such a day the radiance of the sky at the zenith ($\theta_s' = 0°$) is roughly three times the radiance of the sky at the horizon. A sky over which L is uniform is given by $C = 0$. For water-incident rays, values of C in the range $-0.9 \le C \le -0.7$ are representative of the range of upwelling radiance distributions observed in natural waters, where the source direction θ_s' in Eq. (4.50) is now measured from the nadir. Thus a submerged swimmer looking toward her horizon may see five to ten times the brightness (radiance) that she sees looking straight down into the depths.

That the subsurface horizon is much brighter than the nadir is in part a consequence of the total internal reflection of rays that are incident on the bottom side of the water surface from nearly horizontal directions. Another reason for the bright subsurface horizon is traceable to the large ratio of forward to backward scattering values of the volume scattering function of natural waters. It is simply more likely that light from the sun (after transmission through the sea surface) will be scattered into nearly horizontal directions than be backscattered into the zenith direction.

The irradiance reflectance for a continuous radiance distribution is given by the ensemble-averaged versions of Eqs. (4.7b) and (4.7c) in which the integrations over the reflected directions $\hat{\xi}$ have been performed by the Monte Carlo procedure:

$$r_{\pm} = \frac{\int_0^{2\pi}\int_0^{\pi/2} L(\theta_s',\phi_s')\, r_{\pm}(\theta_s',\phi_s') \cos\theta_s' \sin\theta_s'\, d\theta_s'\, d\phi_s'}{\int_0^{2\pi}\int_0^{\pi/2} L(\theta_s',\phi_s') \cos\theta_s' \sin\theta_s'\, d\theta_s'\, d\phi_s'}.$$

Here $r_{\pm}(\theta_s',\phi_s')$ is the Monte Carlo-produced reflectance for a collimated light source, and $r_{\pm}$ is the corresponding reflectance for a continuous radiance distribution over the appropriate hemisphere. As before, r_+ is short for $r(a,w)$, and r_- is $r(w,a)$. Assuming a cardioidal distribution for $L(\theta_s',\phi_s')$ and integrating gives

$$r_{\pm} = \frac{3}{(2C+3)\pi} \int_0^{2\pi}\int_0^{1} (1 + C\mu_s')\, \mu_s'\, r_{\pm}(\mu_s',\phi_s')\, d\mu_s'\, d\phi_s', \tag{4.51}$$

after letting $\mu_s' = \cos\theta_s'$.

The integral (4.51) can be evaluated numerically using the Monte Carlo-generated values of $r_{\pm}(\theta_s',\phi_s') \equiv r_{\pm}(\mu_s',\phi_s')$, which were discussed on the previous pages. This is precisely the approach taken by Preisendorfer and Mobley (1985, 1986), who fit a bicubic spline function to the available

$r_{\pm}(\mu_s', \phi_s')$ values. The continuous spline function was then used to integrate Eq. (4.51) numerically. This approach was computationally more efficient than performing *de novo* ray tracing for the cardioidal distribution. Figure 4.16 shows their computed $r_+ = r(a,w)$ for a uniform sky and for heavy overcast conditions. The results for total (solid curve) and single (dashed curve) scattering were computed by using the corresponding values of $r_+(\mu_s', \phi_s')$ in Eq. (4.51).

For the case of no wind, $r_+(\mu_s', \phi_s')$ is the Fresnel reflectance function, and Eq. (4.51) can be integrated analytically (*H.O. VI*, p. 22) to give $r_+(C=0) = 0.0665$ and $r_+(C=2) = 0.0513$ for the index of refraction $n_w = 4/3$. The values computed by the bicubic spline integrations were respectively $r_+(C=0) = 0.0669$ and $r_+(C=2) = 0.0519$ at $U = 0$. These comparisons indicate that the bicubic spline integration of Eq. (4.51) using the available collimated- source reflectances did not introduce any significant errors into the r_+ values. We see in general that the reflectances r_+ decrease with increasing wind speed and that the contribution by multiply scattered rays is usually significant.

The diffuse-light reflectances for water-incident rays are shown in Fig. 4.17 for a variety of upwelling subsurface radiance distributions. Solid

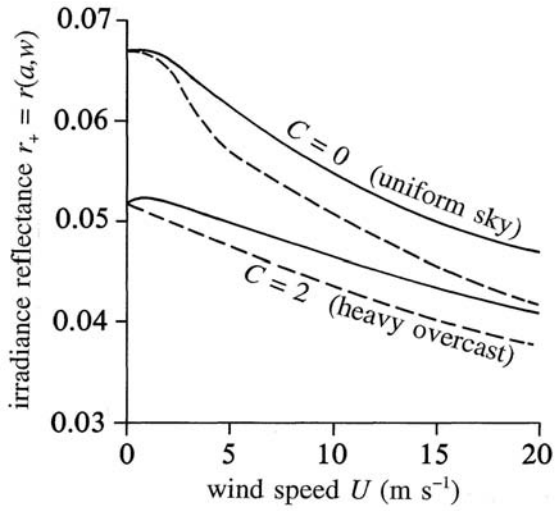

Fig. 4.16. Reflectances $r_+ = r(a,w)$ for continuous radiance distributions over the sky hemisphere. Solid lines are for total scattering, and dashed lines are for single scattering only. C is the cardioidal parameter of Eq. (4.50). [redrawn from Preisendorfer and Mobley (1985)]

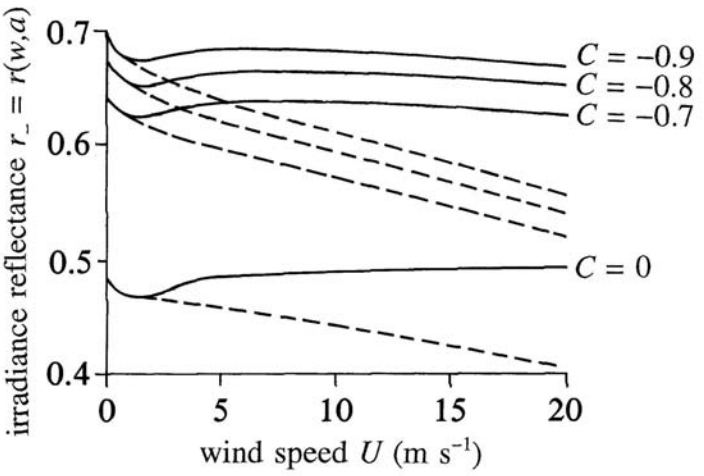

Fig. 4.17. Reflectances $r_- = r(w,a)$ for continuous radiance distributions over the water hemisphere. Solid lines are for total scattering and dashed lines are for single scattering only. C is the cardioidal parameter of Eq. (4.50). [redrawn from Preisendorfer and Mobley (1985)]

curves are for total scattering; dashed curves are for single scattering. For $U = 0$ and a uniform radiances distribution ($C = 0$), Judd (1942) numerically estimated the value $r_-(C{=}0) = 0.475$ for $n_w = 4/3$. The above integration of Eq. (4.51) for $U = 0$ yields $r_-(C{=}0) = 0.486$, a difference of about 2%. We see that both for uniform ($C = 0$) and natural lighting conditions ($C = -0.7, -0.8, -0.9$), the total r_- is only weakly dependent on wind speed in the total scattering (solid curve) case, but is about an order of magnitude greater than r_+. The observed dip in r_- at low wind speeds constitutes the net effects of the relative importance for different θ_s' of the rapidly changing values of $r_-(\theta_s', \phi_s')$ seen in Fig. 4.14. For the single scattering case, there is a significant decrease of r_- with wind speed. In practice, of course, one would work only with the total scattering (solid) curves in all of the above figures.

It is important to distinguish between the *albedo of the entire water body*,

$$A \equiv \frac{E_u(a)}{E_d(a)},$$

and the irradiance reflectance $r_+ = r(a,w)$ of the air-water surface itself. The difference in A and $r(a,w)$ is that A includes downwelling irradiance reflected back upward by the surface, as well as upwelling irradiance

transmitted from beneath the surface to above it; recall Eq. (4.5). Thus we expect that $r(a,w) < A$. This is indeed the case, as can be seen by comparing the present computations or $r(a,w)$ with measured albedos seen, for example, in Payne (1972) and in Simpson and Paulson (1979). This comparison is discussed in Preisendorfer and Mobley (1986).

The proper use of the quantities just computed is this: *the $r_\pm$ and $t_\pm$ values are necessary input to the irradiance boundary conditions at the air-water surface, as expressed by the interaction principles* (4.5) and (4.6). These boundary conditions are necessary for the solution of the two-flow irradiance equations for E_u and E_d, which will be developed in Section 5.10. The two-flow irradiance equations, when combined with their boundary conditions and certain additional information about the optical properties of the water itself, account for the effects of the water body as well as of the boundaries. The equations generate values of E_u/E_d that can be directly compared with observations. The solution of these equations along with their boundary conditions is the subject of Chapter 7.

4.7 Radiance Transfer Functions ▌▌

We now illustrate the evaluation of the *radiance* reflectance and transmittance functions of a random air-water surface. These functions are needed in the interaction principles (4.3) and (4.4), which are the sea-surface boundary conditions necessary for solution of the radiance transfer equation for $L(\zeta,\theta,\phi)$, to be developed in the next chapter.

We shall again work with the random capillary surfaces defined in Section 4.3 and perform ray tracing as outlined in Section 4.4. The ray-tracing procedure of this section is generally the same as that described in Section 4.5 for the irradiance case. There is, however, one important difference stemming from the fact that radiance is a directional quantity. Since its reflectance and transmittance functions must convert one radiance into another radiance, it follows that the transfer functions must be bidirectional: one direction $\hat{\boldsymbol{\xi}}'$ for incident rays, and one direction $\hat{\boldsymbol{\xi}}$ for scattered rays, as was seen in Eqs. (4.3) and (4.4).

When doing numerical studies of radiance fields, it is impossible to consider the infinite number of pairs $(\hat{\boldsymbol{\xi}}', \hat{\boldsymbol{\xi}})$ of incident and scattered directions. Some sort of *directional discretization* is required, so that only a *finite* number of direction pairs need be treated. Accordingly, we partition the upper (Ξ_u) and lower (Ξ_d) hemispheres of directions into a finite set of quadrilateral regions, called *quads*, plus a polar cap for each hemisphere. We then use the Monte Carlo procedure to compute certain averages over

these regions. Towards this end, we pause to define the notion of *quad-averaged directional functions*, such as $L(\hat{\xi})$, and of *quad-averaged bidirectional functions*, such as the $r(a,w;\hat{\xi}' \to \hat{\xi})$, etc. of Eqs. (4.3) and (4.4). We shall use these definitions to obtain a quad-averaged, i.e. a directionally discretized, form of the interaction principles (4.3) and (4.4). Moreover, we shall use these quad-averaging concepts repeatedly in Chapter 8 to reduce the radiance transfer equation within the water body to a form that is computationally tractable, and compatible with the quad-averaged interaction principles for the surface. Hence the work of this section provides both the radiance transfer functions of a random air-water surface and a foundation for later numerical developments.

Quad-averaged directional functions ▌▌

For our present and later purposes we partition the unit sphere Ξ of directions into quadrilateral domains called *quads*, and into *polar caps*. A quad is bounded by circular arcs of constant μ, i.e. of constant polar angle θ, and by circular arcs of constant azimuthal angle ϕ. The polar caps are circular domains centered on the two poles of the unit sphere. Figure 4.18 illustrates a partitioning of Ξ by means of 9 circles of constant μ (4 in the upper hemisphere, 4 in the lower hemisphere, and the equator) and by 20 semicircles of constant ϕ. Thus there are $4 \times 20 + 4 \times 20 = 160$ quads, and two polar caps. The figure also shows two directions, $\hat{\xi}'$ and $\hat{\xi}$, respectively belonging to two different quads, Q_{rs} in Ξ_d and Q_{uv} in Ξ_u. The symbol "Q_{ij}" denotes the quad indexed by the i^{th} μ and j^{th} ϕ values, where $i = 1,...,m$ and $j = 1,...,2n$ are numbered from some reference quad chosen for convenience. Note that the solid angles

$$\Omega_{rs} = \int\int_{Q_{rs}} d\mu\, d\phi \quad \text{and} \quad \Omega_{uv} = \int\int_{Q_{uv}} d\mu\, d\phi$$

associated with quads Q_{rs} and Q_{uv} are in general unequal in size. Other partitionings of Ξ and indexing details will be discussed below.

Let $F(\hat{\xi}) \equiv F(\mu,\phi)$ denote any continuous function of direction. For example, $F(\hat{\xi})$ can be the spectral radiance, $F(\hat{\xi}) = L(\vec{x};\hat{\xi};\lambda)$, where we omit the position and wavelength arguments for brevity. Then the *quad average* of $F(\hat{\xi})$ over any quad Q_{uv} in Ξ is defined by

$$F(u,v) \equiv \frac{1}{\Omega_{uv}} \int_{\xi \in Q_{uv}} F(\hat{\xi})\, d\Omega(\hat{\xi}) = \frac{1}{\Omega_{uv}} \int\int_{(\mu,\phi) \in Q_{uv}} F(\mu,\phi)\, d\mu\, d\phi\,. \qquad (4.52)$$

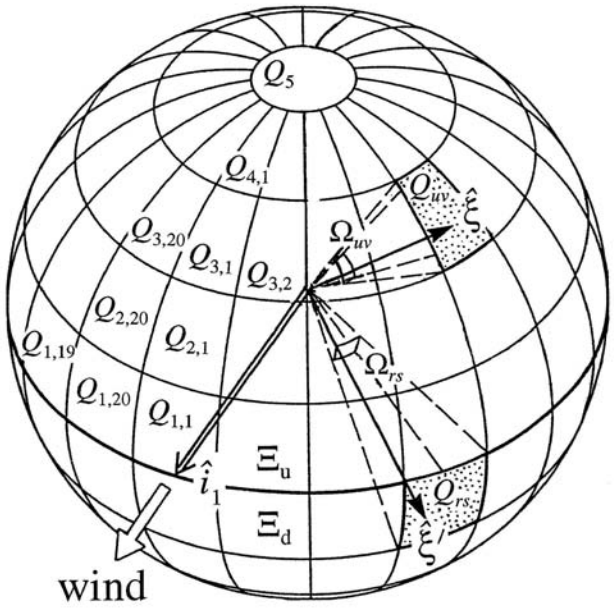

Fig. 4.18. An example partitioning of the unit sphere Ξ into quads, for the case of $m = 5$ μ-bands and $n = 10$ ϕ-bands. The origin of the wind-oriented $\hat{i}_1$-$\hat{i}_2$-$\hat{i}_3$ coordinate system is at the center of the unit sphere Ξ; only $\hat{i}_1$ is shown. Several quads in the upper hemisphere Ξ_u are explicitly labeled. [redrawn from Mobley and Preisendorfer (1988)]

Quad-averaged quantities are fundamental building blocks of many numerical radiative transfer models, in the particular Monte Carlo models discussed in Chapter 6 and the invariant-imbedding model to be developed in Chapter 8. Owing to the "smearing out" of the continuous $F(\hat{\xi})$ by the directional averaging in Eq. (4.52), the numerical model will not be able to resolve features of the radiance distribution that subtend solid angles smaller than Ω_{uv}. However, the solid angles of the quads can in principle be made arbitrarily small.

In a manner of speaking, the quad-averaging process replaces the "clear" unit sphere (with perfect μ-ϕ resolution) by a polyhedron of frosted glass windows; each window (i.e., each quad or polar cap) makes uniform the radiance distribution within that window. We note, however, that a model built up from such quad-averaging is still capable of arbitrarily fine resolution in its other variables, such as depth and wavelength.

Mathematical formalism of quad averaging ▌▌

The quad-averaging integral operator of Eq. (4.52) converts any continuous function of direction into its quad-averaged counterpart. However, later applications of this operation to the development of quad-averaged forms of complicated equations will be simplified if we pause now to formalize the quad-averaging procedure.

The quad-averaging procedure can be implemented in practice via the formal replacement of a function $F(\mu,\phi)$ defined on the unit sphere Ξ by the following linear combination $\bar{F}(\mu,\phi)$ of its quad averages $F(p,q)$:

$$\bar{F}(\mu,\phi) \equiv \sum_p \sum_q \chi_{pq}(\mu,\phi)\, F(p,q)\,, \tag{4.53}$$

where the dimensionless *quad indicator function* is defined by

$$\chi_{pq}(\mu,\phi) \equiv \begin{cases} 1 \text{ if } (\mu,\phi) \in Q_{pq} \\ 0 \text{ if } (\mu,\phi) \notin Q_{pq}\,, \end{cases} \tag{4.54}$$

and where $\Sigma_p\Sigma_q$ denotes a sum over all quads and polar caps Q_{pq} in the unit sphere Ξ. Henceforth, unless noted otherwise, polar caps will be considered as special quads. Observe that $\bar{F}(\mu,\phi)$ is a *piecewise continuous function of direction* but remains *constant* as (μ,ϕ) varies inside Q_{pq}, and is of magnitude $F(p,q)$, whereas the original $F(\mu,\phi)$ in Eq. (4.52) may have varied inside Q_{pq}. This follows from our interpretation of $F(u,v)$ as an average and emphasizes the consequence of the directional averaging operation. The same quad average over Q_{uv}, namely $F(u,v)$, is obtained from Eq. (4.52) if $\bar{F}(\mu,\phi)$ is used in place of $F(\mu,\phi)$, as is easily shown by direct computation:

$$\begin{aligned} \frac{1}{\Omega_{uv}} \iint_{Q_{uv}} \bar{F}(\mu,\phi)\, d\mu\, d\phi &= \frac{1}{\Omega_{uv}} \iint_{Q_{uv}} \left[\sum_p \sum_q \chi_{pq}(\mu,\phi)\, F(p,q) \right] d\mu\, d\phi \\ &= \sum_p \sum_q F(p,q)\, \frac{1}{\Omega_{uv}} \iint_{Q_{uv}} \chi_{pq}(\mu,\phi)\, d\mu\, d\phi \\ &= \sum_p \sum_q F(p,q)\, \frac{1}{\Omega_{pq}} \delta_{p-u}\, \delta_{q-v} \iint_{Q_{uv}} d\mu\, d\phi \\ &= F(u,v)\,. \end{aligned} \tag{4.55}$$

The interchange of summation and integration in the second line above is possible since only $\chi_{pq}(\mu,\phi)$ depends on (μ,ϕ). But $\chi_{pq}(\mu,\phi)$ is nonzero (namely of unit magnitude) only when $(\mu,\phi) \in Q_{pq}$, so the integral over Q_{uv}

is nonzero (and equal to Ω_{uv}) only when quad Q_{pq} is quad Q_{uv}. This is expressed in the third line by means of the Kronecker delta symbols. Thus we see that

$$F(u,v) = \frac{1}{\Omega_{uv}} \iint_{Q_{uv}} \bar{F}(\mu,\phi)\, d\mu\, d\phi \tag{4.56a}$$

and

$$\bar{F}(\mu,\phi) = \sum_p \sum_q \chi_{pq}(\mu,\phi)\, F(p,q) \tag{4.56b}$$

constitute a transform pair that respectively convert a continuous function of (μ,ϕ) into a discrete function of (u,v), and vice versa.

Let us illustrate the utility of this formalism by its application to Eq. (1.23), which gives the downwelling plane irradiance E_d in terms of the continuous radiance distribution $L(\mu,\phi)$:

$$E_d = \iint_{\Xi_d} L(\mu,\phi)\, |\mu|\, d\mu\, d\phi\,. \tag{4.57}$$

Our goal is to obtain a formula which gives E_d in terms of quad-averaged radiances. We thus replace $L(\mu,\phi)$ by $\bar{L}(\mu,\phi)$ and employ Eq. (4.53) to get

$$\begin{aligned} E_d &= \iint_{\Xi_d} \left[\sum_u \sum_v \chi_{uv}(\mu,\phi)\, L(u,v) \right] |\mu|\, d\mu\, d\phi \\ &= \sum_u \sum_v L(u,v) \iint_{\Xi_d} \chi_{uv}(\mu,\phi)\, |\mu|\, d\mu\, d\phi \\ &= \sum_u \sum_v L(u,v) \iint_{Q_{uv}} \mu\, d\mu\, d\phi\,. \end{aligned} \tag{4.58}$$

The last equation follows because $\chi_{uv}(\mu,\phi) \neq 0$ only when $(\mu,\phi) \in Q_{uv} \in \Xi_d$. The absolute value sign on μ has been dropped since $\mu > 0$ in Ξ_d, and the sums over u and v now mean summation over all quads in Ξ_d. Now let $\mu_u(1) < \mu_u(2)$ and $\phi_v(1) < \phi_v(2)$ be the bounding (μ,ϕ) values of quad Q_{uv}, i.e. the quad is of size $\Delta\mu_u = \mu_u(2) - \mu_u(1)$ by $\Delta\phi_v = \phi_v(2) - \phi_v(1)$. The μ-ϕ integral in Eq. (4.58) then becomes

$$\begin{aligned} \iint_{Q_{uv}} \mu\, d\mu\, d\phi &= \int_{\phi_v(1)}^{\phi_v(2)} \int_{\mu_u(1)}^{\mu_u(2)} \mu\, d\mu\, d\phi \\ &= \tfrac{1}{2}[\mu_u^2(2) - \mu_u^2(1)]\, [\phi_v(2) - \phi_v(1)] \\ &= \tfrac{1}{2}[\mu_u(2) + \mu_u(1)]\, [\mu_u(2) - \mu_u(1)]\, [\phi_v(2) - \phi_v(1)] \\ &= \mu_u\, \Delta\mu_u\, \Delta\phi_v = \mu_u\, \Omega_{uv}\,. \end{aligned} \tag{4.59}$$

Here $\mu_u \equiv \frac{1}{2}[\mu_u(2) - \mu_u(1)]$ is the average value of μ over quad Q_{uv}. Note that μ_u is not to be confused with $\bar{\mu}_u$, the upwelling average cosine defined in Eq. (3.15). The quad-averaged formula for E_d thus becomes

$$E_d = \sum_u \sum_v L(u,v)\,|\mu_u|\,\Omega_{uv}\,. \qquad (Q_{uv} \in \Xi_d) \tag{4.60}$$

Note the net result of applying the quad-averaging formalism: the integral over all directions (μ,ϕ) in Ξ_d is replaced by a sum over all quads in Ξ_d; continuous functions of direction, here $L(\mu,\phi)$ and μ itself, are replaced by the corresponding quad-averaged values, here $L(u,v)$ and μ_u; and the differential element of solid angle $d\mu d\phi$ is replaced by the finite solid angle of a quad, Ω_{uv}. The general validity of these simple conversion recipes (integrals to sums, etc.) follows from the precise formalism of the quad-averaging process.

Partitioning the unit sphere ▌▌

In the preceding discussion of quad-averaging, we saw qualitatively in Fig. 4.18 how the unit sphere is partitioned into quads. We also used notation such as "$\Sigma_p\Sigma_q F(p,q)$" and remarked that the sums were "over all quads in Ξ" or "over all quads in Ξ_d," as was appropriate to the case at hand. We now mention several schemes for partitioning Ξ into quads, and we establish a bookkeeping scheme for labeling the quads. We can then be more specific about how such sums are to be evaluated.

Let the number of quads in the μ-direction be M and let the number in the ϕ-direction be N ($M = 10$ and $N = 20$ in Fig. 4.18). Furthermore, let M and N be even, i.e. of the form $M = 2m$ and $N = 2n$ and, for reasons that will become clear later, let n itself be even. The restriction to even M and n values represents no significant loss of generality in the numerical model, but greatly simplifies the analysis formulas below. We also require that non-polar cap quads have equal angular widths in the ϕ-direction (the uniform $\Delta\phi$ makes possible the Fourier analysis in Chapter 8). Thus we set

$$\Delta\phi = \frac{2\pi}{N} = \frac{\pi}{n}, \quad \text{with } n \text{ even}.$$

We are free to center the first quad on the $\phi = 0°$, or downwind, direction as shown by the $\hat{i}_1$ unit vector in Fig. 4.18. Then the centers of the non-polar quads Q_{uv} have the ϕ values

$$\phi_v = (v - 1)\,\Delta\phi = (v - 1)\,\frac{\pi}{n}, \quad v = 1, 2, ..., 2n\,. \tag{4.61}$$

The azimuthal angle ϕ_v is not defined for the polar cap quads (just as ϕ is not defined at the poles, $\theta = 0$ and $\theta = \pi$, in a spherical coordinate system).

In Eq. (4.61), index $v = 1$ corresponds to the downwind azimuthal direction. It is convenient to let the polar angle index $u = 1$ label the bands of quads adjacent to the "equator" of Ξ. Then $u = m$ labels the polar caps. This notation is ambiguous since every quad Q_{uv} or Q_m in Ξ_u has its mirror image in Ξ_d. However, the context or other notation will always make clear which quad (the one in Ξ_u or Ξ_d) is meant.

The angular size $\Delta\mu$ (or $\Delta\theta$) of the quads in the μ direction can be fixed as desired. Unlike the azimuthal case, there is no requirement that the quads in different μ bands (defined by pairs of neighboring circles of constant μ value) have equal $\Delta\mu$ values. One simple scheme for defining the μ bands is to let $\Delta\mu_u = \Delta\mu = 1/m$, and thus have quads of equal μ size and hence of equal solid angle $\Omega_{uv} = \Delta\mu_u\Delta\phi_v = \Delta\mu\Delta\phi$ (except for the polar cap quads). With this choice there are $2(m-1)2n$ non-polar quads of size $\Omega_{uv} = (1/m)(\pi/n)$ sr, and two polar cap quads of size $\Omega_m = (1/m)(2\pi)$ sr, which total to the required 4π sr in Ξ.

Alternatively, if we set

$$\Delta\mu_u = \frac{2n}{(m-1)2n+1} = \Delta\mu \quad \text{for } u = 1, 2, ..., m-1,$$

and

$$\Delta\mu_m = \frac{\Delta\mu}{2n} \quad \text{for the polar cap, } u = m,$$

then all quads including the polar caps have the same solid angle

$$\Delta\Omega = \frac{2\pi}{(m-1)2n+1}.$$

This equal-solid-angle partition of Ξ is shown in Fig. 4.19(a) for $m = 10$, $n = 12$; i.e. 434 quads each of solid angle $\Delta\Omega \approx 0.029$ sr. The equal-solid-angle partition may be inconvenient for some applications, because the quads near the pole cover a large θ range and thus, for example, may cause an unacceptable loss of θ-resolution for solar positions near the zenith, or for lines of sight directed near the nadir. Fig. 4.19(b) shows an equal $\Delta\theta$ partition of the unit sphere. Figure 4.19(c) shows an equal $\Delta\theta$ case for a relatively fine partition with $m = 23$, $n = 30$, so that $\Delta\theta \approx 4°$ and $\Delta\phi = 6°$. A quad partitioning with $m \approx 10$, $n \approx 12$ as in Fig. 4.19(b) has been found to be reasonable for most computations, especially for those where irradiances or irradiance *K*-functions are the quantities of primary interest.

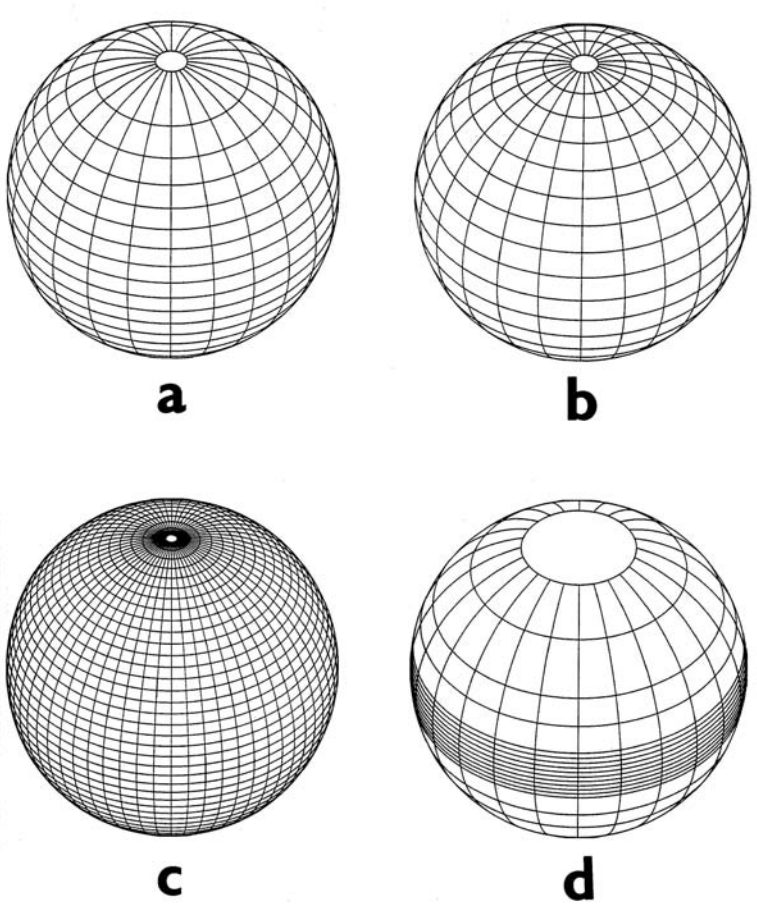

Fig. 4.19. Further examples of partitions of the unit sphere into quads. (a) $m = 10$ μ-bands and $n = 12$ ϕ-bands, with all solid angles Ω_{pq} and Ω_m equal. (b) $m = 10$ and $n = 12$, with all $\Delta\theta$ values equal. (c) $m = 23$, $n = 30$, with equal $\Delta\theta$ values, so that $\Delta\theta \approx 4°$, $\Delta\phi = 6°$. (d) $m = 10$, $n = 12$, with an *ad hoc* selection of the $\Delta\theta$ values. [redrawn from Mobley and Preisendorfer (1988)]

Quad partitionings as fine as that of Fig. 4.19(c) are required only if high angular resolution of the radiance distribution is required, although it is computationally reasonable to run the numerical model developed in Chapter 8 with such grids. Special studies may require an *ad hoc* spacing of the μ bands. Figure 4.19(d) shows a partitioning with many μ bands near the equator, as might be needed in a study requiring high angular resolution of the sun when very near the horizon. We do note that a grid for which the solar disk, which subtends an angle of about 0.5°, fills one quad of size

$\Delta\theta = \Delta\phi = 0.5°$ would require $m = 180$, $n = 360$. Since computation and storage requirements of the model developed in Chapter 8 are generally proportional to m^2n^2, such a grid would require nearly 300,000 times the computer effort relative to the $m = 10$, $n = 12$ grid. Such resolution is presently beyond the computational abilities of all but the most powerful computers.

For notational convenience in our later development, we will occasionally write sums of a function $F(p,q)$ over all quads as separate sums over $\Xi_+ \equiv \Xi_d$ and $\Xi_- \equiv \Xi_u$. Correspondingly, we will sometimes add a "+" or "−" superscript to the summand as a reminder of which hemisphere is referenced by the sum, as for example in

$$\sum_{\substack{p\\(Q_{pq}\in\Xi)}}\sum_{q} F(p,q) = \sum_{\substack{p\\(Q_{pq}\in\Xi_+)}}\sum_{q} F^+(p,q) + \sum_{\substack{p\\(Q_{pq}\in\Xi_-)}}\sum_{q} F^-(p,q)\,.$$

Here "$(Q_{pq} \in \Xi)$" means "all quads Q_{pq} of Ξ are to be summed over", etc.

Because there is no ϕ dependence for the polar caps, these "quads" are always special cases. The value of $F(p,q)$ at a polar cap will then be denoted by "$F^{\pm}(m,\cdot)$." Thus we write

$$\sum_{\substack{p\\(Q_{pq}\in\Xi)}}\sum_{q} F(p,q) = \sum_{p=1}^{m-1}\sum_{q=1}^{2n} F^+(p,q) + F^+(m,\cdot) + \sum_{p=1}^{m-1}\sum_{q=1}^{2n} F^-(p,q) + F^-(m,\cdot)\,. \tag{4.62}$$

Sums over Ξ or $\Xi_\pm$ will always be computed as shown by the explicit notation of Eq. (4.62), although we shall often omit the ranges of p and q if there is no danger of confusion.

Quad-averaged bidirectional functions

We can extend the above quad-averaging concept to bidirectional functions such as the surface transfer functions $r(a,w;\hat{\boldsymbol{\xi}}'\to\hat{\boldsymbol{\xi}})$, etc., or the scattering phase function $\tilde{\beta}(\hat{\boldsymbol{\xi}}'\to\hat{\boldsymbol{\xi}})$. In our equations, such functions will always have units of sr^{-1}. Accordingly, let $f(\hat{\boldsymbol{\xi}}'\to\hat{\boldsymbol{\xi}}) = f(\mu',\phi'\to\mu,\phi)$ be any bidirectional function with units of sr^{-1}. Then an appropriate extension of Eq. (4.52) is

$$f(r,s\rightarrow u,v) = \frac{1}{\Omega_{uv}} \int_{Q_{uv}} \left[\int_{Q_{rs}} f(\hat{\xi}'\rightarrow\hat{\xi})\, d\Omega(\hat{\xi}') \right] d\Omega(\hat{\xi})$$
$$= \frac{1}{\Omega_{uv}} \int\int_{Q_{uv}} d\mu\, d\phi \int\int_{Q_{rs}} d\mu'\, d\phi'\, f(\mu',\phi'\rightarrow\mu,\phi)\,, \tag{4.63}$$

where Q_{rs} and Q_{uv} are any quads or polar caps in Ξ. Observe that $f(r,s\rightarrow u,v)$ is dimensionless. The inverse of this transformation, corresponding to Eq. (4.53), is

$$\bar{f}(\hat{\xi}'\rightarrow\hat{\xi}) \equiv \bar{f}(\mu',\phi'\rightarrow\mu,\phi)$$
$$= \sum_r \sum_s \sum_u \sum_v \chi_{rs}(\mu',\phi')\, \chi_{uv}(\mu,\phi)\, \frac{f(r,s\rightarrow u,v)}{\Omega_{rs}} \qquad (\mathrm{sr}^{-1})\,, \tag{4.64}$$

where the quad indicator functions $\chi_{rs}(\mu',\phi')$ and $\chi_{uv}(\mu,\phi)$ are defined as in Eq. (4.54). The sums over r,s and u,v are evaluated as in Eq. (4.62). Here $\bar{f}(\mu',\phi'\rightarrow\mu,\phi)$ is a bidirectional step function, the quad-averaged approximation to $f(\mu',\phi'\rightarrow\mu,\phi)$. If $\bar{f}(\mu',\phi'\rightarrow\mu,\phi)$ is substituted in place of $f(\mu',\phi'\rightarrow\mu,\phi)$ in Eq. (4.63), we obtain $f(r,s\rightarrow u,v)$, as expected.

When there is no natural "up-down" notation built into $f(\mu',\phi'\rightarrow\mu,\phi)$ [this will be the case in Chapter 8 for the scattering function $\tilde{\beta}(\mu',\phi'\rightarrow\mu,\phi)$], we can keep track of which hemisphere ($\Xi_+ = \Xi_d$ or $\Xi_- = \Xi_u$) a directional index pair (r,s) or (u,v) belongs to in the quantity $f(r,s\rightarrow u,v)$ by appending "+" and "−" superscripts to f. There are four cases, for which we write

$$f^{\pm\pm}(r,s\rightarrow u,v) \text{ if } Q_{rs} \text{ is in } \Xi_\pm \text{ and } Q_{uv} \text{ is in } \Xi_\pm\,,$$
$$f^{\pm\mp}(r,s\rightarrow u,v) \text{ if } Q_{rs} \text{ is in } \Xi_\pm \text{ and } Q_{uv} \text{ is in } \Xi_\mp\,. \tag{4.65}$$

Here we read upper and lower signs together. From the basic definitions in Eqs. (4.3) and (4.4), we see that the quad-averaged form of $t(a,w;\hat{\xi}'\rightarrow\hat{\xi})$ is of the type f^{++}, $t(w,a;\hat{\xi}'\rightarrow\hat{\xi})$ is of the type f^{--}, $r(a,w;\hat{\xi}'\rightarrow\hat{\xi})$ is of the type f^{+-}, and $r(w,a;\hat{\xi}'\rightarrow\hat{\xi})$ is of the type f^{-+}.

Finally, we establish some notation to cover the special directions involved with the polar caps of the partitioned direction sphere Ξ. The notation carries to bidirectional functions the convention established in Eq.(4.62). There are three cases in the bidirectional function setting:

polar cap to quad: $f(m,\cdot\rightarrow u,v)$
quad to polar cap: $f(r,s\rightarrow m,\cdot)$
polar cap to polar cap: $f(m,\cdot\rightarrow m,\cdot)$.

The dot serves to fill the unneeded azimuthal direction at the caps. It will be clear from the context (e.g., using superscript ± notation) whether we are at one or the other polar cap.

Quad-averaged surface boundary conditions ▌▌

The interaction principles (4.3) and (4.4) may be placed into a directionally discrete form by using the preceding definitions of quad-averaged radiances and surface transfer functions. To illustrate the process, we first quad-average each side of Eq. (4.3) over quad Q_{uv}. The left side by definition is $L(a;u,v)$, with Q_{uv} in Ξ_+. The first term on the right side of Eq. (4.3) becomes

$$\frac{1}{\Omega_{uv}} \iint_{Q_{uv}} d\mu\, d\phi \left\{ \sum_r \sum_s \iint_{Q_{rs}} d\mu'\, d\phi'\, L(w;\mu',\phi')\, t(w,a;\mu',\phi' \rightarrow \mu,\phi) \right\},$$

where we have written the integral over Ξ_- as the sum of integrals over all Q_{rs} in Ξ_-. Next, using the approximate quad-averaged representation (4.53) for $L(w;\mu',\phi')$, this term reduces to

$$\sum_r \sum_s \sum_p \sum_q L(w;p,q) \times \left\{ \frac{1}{\Omega_{uv}} \iint_{Q_{uv}} d\mu\, d\phi \left[\iint_{Q_{rs}} d\mu'\, d\phi'\, \chi_{pq}(\mu',\phi')\, t(w,a;\mu',\phi' \rightarrow \mu,\phi) \right] \right\}.$$

The indicator function χ_{pq} in the square brackets produces zero integrals over Q_{rs} unless $(p,q) = (r,s)$. The net result is

$$\sum_r \sum_s L(w;r,s) \left\{ \frac{1}{\Omega_{uv}} \iint_{Q_{uv}} d\mu\, d\phi \iint_{Q_{rs}} d\mu'\, d\phi'\, t(w,a;\mu',\phi' \rightarrow \mu,\phi) \right\}$$

$$\equiv \sum_r \sum_s L(w;r,s)\, t(w,a;r,s \rightarrow u,v)\,,$$

where we have used Eq. (4.63) to define $t(w,a;r,s \rightarrow u,v)$ as the quantity in braces.

By repeating this development for the other terms in the boundary conditions, we eventually arrive at the quad-averaged versions of Eqs. (4.3) and (4.4):

$$L(a;u,v) = \sum_r \sum_s L(w;r,s)\, t(w,a;r,s\to u,v) + \sum_r \sum_s L(a;r,s)\, r(a,w;r,s\to u,v) \tag{4.66}$$

$$L(w;u,v) = \sum_r \sum_s L(w;r,s)\, r(w,a;r,s\to u,v) + \sum_r \sum_s L(a;r,s)\, t(a,w;r,s\to u,v)\,. \tag{4.67}$$

Each of the four transfer functions in Eqs. (4.66) and (4.67) has been obtained from its continuous counterpart by an application of Eq. (4.63). These interaction principles are for the water surface $S[a,w]$ of the medium. Observe how the ordered pairs (a,w) and (w,a) of depths of the upper (a) and lower (w) faces of the surface together with the "t" and "r" symbols serve to indicate the direction of transfer of the radiant power at the surface. This notation serves also to make clear the hemispheres (+ or −) over which the sums are to be taken. Thus $L(w;r,s)$ in Eq. (4.66), being an *incident* radiance on the bottom (water) side of the surface , must be upward, so that Q_{rs} is in $\Xi_- = \Xi_u$. The *response* radiance $L(a;u,v)$ on the upper (air) side of the surface must therefore be upward; and so on. Equations (4.66) and (4.67) will play crucial roles in the numerical solution of the radiance transfer equation in Chapter 8.

Radiance transfer functions by Monte Carlo simulation ▌▌

We are finally in position to start constructing the radiance transfer functions for the random air-water surface.

Let us consider a Monte Carlo experiment in which many air-water surface realizations $S(\omega)$ are generated, as in Section 4.5. For each surface realization $S(\omega)$, $\omega = 1, 2, ..., S$, one parent ray is aimed toward the surface along a randomly chosen direction in some selected input quad Q_{rs}, as in Fig. 4.18. Let $\hat{\xi}'_{rs}$ denote such a ray. This ray interacts with the ω^{th} surface realization, as illustrated in Fig. 4.6, and generates $\kappa(\hat{\xi}'_{rs};\omega)$ final daughter rays emerging from the hexagonal domain ($\kappa = 3$ in Fig. 4.6). The parent ray $\hat{\xi}'_{rs}$ is assigned a unit amount of radiant power, $\Phi' = 1$. At each interaction of a ray with a wave facet, the radiant power of the incident ray is apportioned to the daughter rays as described in Section 4.5. Thus when the parent ray intercepts a wave facet, the reflected daughter ray is assigned a radiant power of magnitude Φr_1, where r_1 is the computed Fresnel reflectance, and the transmitted ray is assigned a power of $\Phi(1-r_1)$. If the reflected daughter ray then intercepts another wave facet, as in Fig. 4.6, the

reflected ray receives a power $\Phi r_1 r_2$ and the transmitted ray receives $\Phi r_1(1-r_2)$, where r_2 is the Fresnel reflectance for the second ray-facet intersection. In this way it is possible to build up arbitrarily long products of Fresnel reflectances and transmittances just as we did in Section 4.5.

Let $\Pi[\hat{\xi}'_{rs}, \hat{\xi}_j(\hat{\xi}'_{rs};\omega)]$ be the product of the Fresnel reflectances and transmittances of all the daughter rays along a single unbroken path through space which connects the parent ray $\hat{\xi}'_{rs}$ with the j^{th} final daughter ray $\hat{\xi}_j(\hat{\xi}'_{rs};\omega)$ emerging from the hexagonal domain. As the notation indicates, the daughter rays $\hat{\xi}_j$, $j = 1, 2, ..., \kappa$, depend on the direction $\hat{\xi}'_{rs}$ of the initial ray and upon the wave facet orientations making up the ω^{th} random surface realization. The Fresnel product Π is dimensionless and satisfies $0 \le \Pi \le 1$. (The product equals 1 only in the case of $\hat{\xi}'_{rs}$ incident on the surface from the water side and undergoing a total internal reflection to generate one final daughter ray $\hat{\xi}_1$).

Now define a *radiant-power transfer function* Φ^{+-} by

$$\Phi^{+-}(r,s;u,v) \equiv \frac{1}{S}\sum_{\omega=1}^{S}\sum_{j=1}^{\kappa(\omega)} \Pi[\hat{\xi}'_{rs}, \hat{\xi}_j(\hat{\xi}'_{rs};\omega)]\, \chi_{uv}[\hat{\xi}_j(\hat{\xi}'_{rs};\omega)]\,, \qquad (4.68a)$$

where Q_{rs} is in Ξ_+ and Q_{uv} is in Ξ_-. As before, $\chi_{uv}(\hat{\xi}_j) = 1$ if $\hat{\xi}_j$ is in quad Q_{uv}, and $\chi_{uv}(\hat{\xi}_j) = 0$ otherwise. The "+" in Φ^{+-} denotes downward incidence (Q_{rs} in Ξ_+) and the "−" denotes upward reflection (Q_{uv} in Ξ_-). The sum over j adds up the κ Fresnel products for all those generated ray paths in space (for a single surface realization) which connect the input quad Q_{rs} and the output quad Q_{uv}; this result is then averaged over the ensemble of S surface realizations. Φ^{+-}(r,s;u,v) is therefore a sample estimate of the fraction of the radiant power incident down on the water surface toward quad Q_{rs} that is reflected up into quad Q_{uv}. This fraction Φ^{+-} can be associated with a unit area of the mean water surface in a way similar to Eq. (3.49) and is therefore an irradiance reflectance of the random sea surface for radiant power from Q_{rs} in Ξ_+ to Q_{uv} in Ξ_-. Three other transfer functions can be defined analogously to Eq. (4.68a), viz.:

$$\Phi^{--}(r,s\to u,v) \text{ when } Q_{rs} \text{ is in } \Xi_- \text{ and } Q_{uv} \text{ is in } \Xi_-, \qquad (4.68b)$$

$$\Phi^{-+}(r,s\to u,v) \text{ when } Q_{rs} \text{ is in } \Xi_- \text{ and } Q_{uv} \text{ is in } \Xi_+, \qquad (4.68c)$$

and

$$\Phi^{++}(r,s\to u,v) \text{ when } Q_{rs} \text{ is in } \Xi_+ \text{ and } Q_{uv} \text{ is in } \Xi_+. \qquad (4.68d)$$

Since the power $\Phi' = 1$ of each parent ray $\hat{\xi}'_{rs}$ is apportioned without loss to the daughter rays, it is easy to see that

$$\sum_{\substack{u \\ (Q_{uv}\in\Xi_-)}}\sum_{v} \Phi^{+-}(r,s\rightarrow u,v) \;+\; \sum_{\substack{u \\ (Q_{uv}\in\Xi_+)}}\sum_{v} \Phi^{++}(r,s\rightarrow u,v) \;=\; 1 \tag{4.69a}$$

for every Q_{rs} in Ξ_+, and

$$\sum_{\substack{u \\ (Q_{uv}\in\Xi_+)}}\sum_{v} \Phi^{-+}(r,s\rightarrow u,v) \;+\; \sum_{\substack{u \\ (Q_{uv}\in\Xi_-)}}\sum_{v} \Phi^{--}(r,s\rightarrow u,v) \;=\; 1 \tag{4.69b}$$

for every Q_{rs} in Ξ_-. These equations merely state that radiant power incident on the water surface is either reflected by the surface or transmitted through the surface without loss.

We also note that the irradiance reflectance of the water surface for power incident in Q_{rs} in Ξ_+ is given by

$$r_+(r,s) \;\equiv\; \sum_u \sum_v \Phi^{+-}(r,s\rightarrow u,v)\,. \tag{4.70a}$$

Here the summation is over the Ξ_- hemisphere. Defining the associated irradiance transmittance $t_+(r,s)$ as

$$t_+(r,s) \;\equiv\; \sum_u \sum_v \Phi^{++}(r,s\rightarrow u,v)\,, \tag{4.70b}$$

where the summation is over Ξ_+, we can express Eq. (4.69a) as

$$r_+(r,s) + t_+(r,s) = 1 \quad \text{for every } Q_{rs} \text{ in } \Xi_+.$$

A similar statement holds for the upward incident power in Eq. (4.69b):

$$r_-(r,s) + t_-(r,s) = 1 \text{ for every } Q_{rs} \text{ in } \Xi_-.$$

The four radiant power transfer functions defined by Eq. (4.68), and evaluated by Monte Carlo ray-tracing, form the core of the four quad-averaged r and t functions for radiance, as will now be seen.

The upward and downward plane irradiances, $E_- \equiv E_u$ and $E_+ \equiv E_d$, as computed from the quad-averaged radiances at any optical depth ζ, are given by [recall Eq. (4.60)]

$$\begin{aligned} E_\pm(\zeta) \;&=\; \sum_u \sum_v L^\pm(\zeta;u,v)\,|\mu_u|\,\Omega_{uv} \\ &\equiv\; \sum_u \sum_v E_\pm(\zeta;u,v)\,, \end{aligned}$$

where we have defined

$$E_{\pm}(\zeta;u,v) \equiv L^{\pm}(\zeta;u,v)\,|\mu_u|\,\Omega_{uv}\,. \tag{4.71}$$

Evaluating the downward irradiance at $\zeta = a$, i.e. at the upper side of $S[a,w]$, contributed solely by power in quad Q_{rs}, we can write the incident radiant power per unit horizontal area of the water surface (the irradiance) as

$$E_{+}(a;r,s) = L^{+}(a;r,s)\,|\mu_r|\,\Omega_{rs}\,.$$

The upward irradiance $E_{-}(a;u,v)$ generated when the sea surface reflects this incident irradiance is

$$E_{-}(a;u,v) = E_{+}(a;r,s)\,\Phi^{+-}(r,s;u,v)$$

since, as we have seen, $\Phi^{+-}(r,s;u,v)$ is by construction the irradiance reflectance connecting Q_{rs} and Q_{uv}. Using Eq. (4.71) this last equation can be written

$$L^{-}(a;u,v)\,|\mu_u|\,\Omega_{uv} = L^{+}(a;r,s)\,|\mu_r|\,\Omega_{rs}\,\Phi^{+-}(r,s\rightarrow u,v)\,,$$

or

$$L^{-}(a;u,v) = L^{+}(a;r,s)\left[\frac{\Phi^{+-}(r,s\rightarrow u,v)\,|\mu_r|\Omega_{rs}}{|\mu_u|\Omega_{uv}}\right]. \tag{4.72}$$

Now we recall the upper surface boundary condition (4.66):

$$L^{-}(a;u,v) = \sum_r \sum_s L^{-}(w;r,s)\,t(w,a;r,s\rightarrow u,v) + \sum_r \sum_s L^{+}(a;r,s)\,r(a,w;r,s\rightarrow u,v)\,.$$

This equation of course holds even if only one particular input quad Q_{rs} is illuminated and all others are dark, as we have postulated for the case of (4.72). In this case, Eq. (4.66) reduces to

$$L^{-}(a;u,v) = L^{+}(a;r,s)\,r(a,w;r,s\rightarrow u,v)\,. \tag{4.73}$$

Since the incident quad-averaged radiances are arbitrary, comparing Eqs. (4.72) and (4.73) immediately yields Eq. (4.74a), below. Equation (4.74a) gives us the connection between the quad-averaged *radiance* reflectance $r(a,w;r,s\rightarrow u,v)$ and the quad-averaged *irradiance* reflectance $\Phi^{+-}(r,s\rightarrow u,v)$

computed by ray tracing. Corresponding analyses for the other terms of the boundary equations (4.66) and (4.67) give the corresponding results seen in Eq. (4.74), which are the desired *radiance transfer functions* across the random air-water surface:

$$r(a,w;r,s\rightarrow u,v) = \Phi^{+-}(r,s\rightarrow u,v)\,\frac{|\mu_r|\Omega_{rs}}{|\mu_u|\Omega_{uv}}\,, \tag{4.74a}$$

$$t(a,w;r,s\rightarrow u,v) = \Phi^{++}(r,s\rightarrow u,v)\,\frac{|\mu_r|\Omega_{rs}}{|\mu_u|\Omega_{uv}}\,, \tag{4.74b}$$

$$r(w,a;r,s\rightarrow u,v) = \Phi^{-+}(r,s\rightarrow u,v)\,\frac{|\mu_r|\Omega_{rs}}{|\mu_u|\Omega_{uv}}\,, \tag{4.74c}$$

$$t(w,a;r,s\rightarrow u,v) = \Phi^{--}(r,s\rightarrow u,v)\,\frac{|\mu_r|\Omega_{rs}}{|\mu_u|\,\Omega_{uv}}\,. \tag{4.74d}$$

On comparing Eqs. (4.74b) and (4.74d) with the discussion of Section 4.2 [recall Eqs. (4.21)-(4.25)], it is clear that the present quad-averaged forms of the transmittance functions for the random air-water surface include the n^2 law for radiance within them.

Energy conservation at the surface ▌▌

A requirement for the quad-averaged radiance reflectances and transmittances is that they conserve energy at the air-water surface. The irradiance balance at the surface for downward incident irradiance is expressed as

$$\int_{\Xi_+} L(a;\mu,\phi)\,|\mu|\,d\Omega(\hat{\xi}) = \int_{\Xi_-} L(a;\mu,\phi)\,|\mu|\,d\Omega(\hat{\xi}) + \int_{\Xi_+} L(w;\mu,\phi)\,|\mu|\,d\Omega(\hat{\xi})\,. \tag{4.75}$$

The left side of Eq. (4.75) is the downward irradiance incident on the water surface from all directions above the surface. The first term on the right side of Eq. (4.75) is the upward irradiance at the surface induced by the incident downward radiance only, and the second term is the downward irradiance just below the surface also induced only by the incident downward radiance. Thus Eq. (4.75) states that the energy received from the sky alone by the surface is either reflected back to the sky or transmitted through to the water column. The quad-averaged form of Eq. (4.75) is

$$\sum_r \sum_s L^+(a;r,s)\,|\mu_r|\,\Omega_{rs} = \sum_u \sum_v L^-(a;u,v)\,|\mu_u|\,\Omega_{uv} + \sum_u \sum_v L^+(w;u,v)\,|\mu_u|\,\Omega_{uv}\,. \tag{4.76}$$

It is easy to show that Eq. (4.76) is an identity. By virtue of Eq. (4.73), for a single arbitrary input quad Q_{rs}, $L^-(a;u,v)$ can be rewritten in terms of $L^+(a;r,s)$, with a similar relation also possible for $L^+(w;u,v)$. If only one arbitrary input quad Q_{rs} of the unit sphere Ξ is illuminated, Eq. (4.76) becomes

$$L^+(a;r,s)\,|\mu_r|\,\Omega_{rs} = \sum_u \sum_v L^+(a;r,s)\,r(a,w;r,s\to u,v)\,|\mu_u|\,\Omega_{uv} + \sum_u \sum_v L^+(a;r,s)\,t(a,w;r,s\to u,v)\,|\mu_u|\,\Omega_{uv}\,,$$

or

$$1 = \frac{1}{|\mu_r|\,\Omega_{rs}} \sum_u \sum_v r(a,w;r,s\to u,v)\,|\mu_u|\,\Omega_{uv} + \frac{1}{|\mu_r|\Omega_{rs}} \sum_u \sum_v t(a,w;r,s\to u,v)\,|\mu_u|\,\Omega_{uv}\,.$$

Substituting from Eqs. (4.74a) and (4.74b) for the quad-averaged irradiances, this equation becomes

$$1 = \sum_u \sum_v \Phi_{+-}(r,s\to u,v) + \sum_u \sum_v \Phi_{++}(r,s\to u,v)\,,$$

or

$$1 = r_+(r,s) + t_+(r,s)\,,$$

after recalling Eq. (4.70). Hence the energy conservation equation (4.75) remains valid in the setting of quad-averaged radiative transfer. A corresponding result is obtained for energy incident onto the surface from below. Thus *ray-by-ray conservation of energy guarantees global (hemisphere-wide) conservation of energy in the computed radiance reflectance and transmittance functions*.

4.8 Numerical Examples of Radiance Transfer

In Section 4.6 we presented the results of numerical computations of water-surface *irradiance* reflectances. There it was relatively easy to display our results graphically as functions of wind speed and incident ray direction

(θ',ϕ'), since only two "output directions," upward and downward, were involved. Unfortunately, there is not a convenient way to present the corresponding results for *radiance* reflectances and transmittances, since now a separate display would be required for each pair of quads Q_{rs} and Q_{uv}. Moreover, quantities such as $r(a,w;\mu',\phi'\rightarrow\mu,\phi)$ and its quad-averaged form $r(a,w;r,s\rightarrow u,v)$ are not as intuitively easy to interpret as, say, the reflectances $r_+(\theta',\phi')$ of Fig. 4.11. However, the radiance reflectance and transmittance functions of a wind-blown water surface are of central importance for radiative transfer in natural waters, and so we must attempt to gain some impression of the behavior of these functions.

A level surface

The simplest case occurs for zero wind speed in Eq. (4.32), so that the air-water surface is flat, as in Section 4.2. For a level surface, we can make a direct comparison of ray-tracing results with the Fresnel reflectance formula, as follows.

Figure 4.20 shows a portion of the upper hemisphere of the $m = 10$, $n = 12$ grid of Fig. 4.19(b), which has all $\Delta\theta$ values equal ($\Delta\theta = 9.474°$), except for the polar cap, which has a half angle of $\Delta\theta = 4.737°$. For this partition of Ξ, $\Delta\phi = \pi/12 = 0.262$ rad $= 15°$. The quad solid angles Ω_{uv} depend on u. Table 4.1 displays the bounding θ and ϕ values of the quads, the average μ values, and the quad solid angles.

In Fig. 4.20 an incident ray $\hat{\boldsymbol{\xi}}'$ is shown approaching the water surface *from* a direction (θ_s',ϕ_s') in a *source* quad Q_{pq} in Ξ_u. The ray $\hat{\boldsymbol{\xi}}'$ is heading *toward input* quad Q_{rs} in Ξ_d, which lies exactly opposite Q_{pq} on the unit sphere Ξ. For a level water surface, the reflected ray $\hat{\boldsymbol{\xi}}$ traveling in direction (θ,ϕ) has $\theta = \theta_s'$, so that any ray heading toward Q_{rs} will be reflected into only one quad Q_{uv}, with $u = r$ and $s = v$, as shown for the case of $u = r = 3$. Angles θ_s' and θ are shown in the figure as zenith angles, for ease of drawing. The vectors $\hat{\boldsymbol{\xi}}'$, $\hat{\boldsymbol{\xi}}$, and $\hat{\boldsymbol{\imath}}_3$ are coplanar. If $\hat{\boldsymbol{\xi}}'$ has unit power, then ray $\hat{\boldsymbol{\xi}}$ has power equal to the value of Fresnel's formula for $r(\theta_s')$ in Eq. (4.14). If a large number of incident rays $\hat{\boldsymbol{\xi}}'$ is selected at random from directions (θ_s',ϕ_s') in Q_{pq}, then $\Phi^{+-}(r,s\rightarrow u,v)$, computed as in Eq. (4.68a) is in effect the average of the Fresnel reflectance over the θ range of the quad Q_{rs}, $\langle r(\theta_s')\rangle_{rs}$. Moreover, since $u = r$ and $s = v$ for a level surface, $|\mu_r|\Omega_{rs} = |\mu_u|\Omega_{uv}$, and Eq. (4.74a) reduces to just

$$r(a,w;r,s\rightarrow r,s) = \Phi^{+-}(r,s\rightarrow r,s) = \langle r(\theta_s')\rangle_{rs}\,.$$

All $r(a,w;r,s\rightarrow u,v)$ values are zero for $r \neq u$ and $s \neq v$. Similar statements

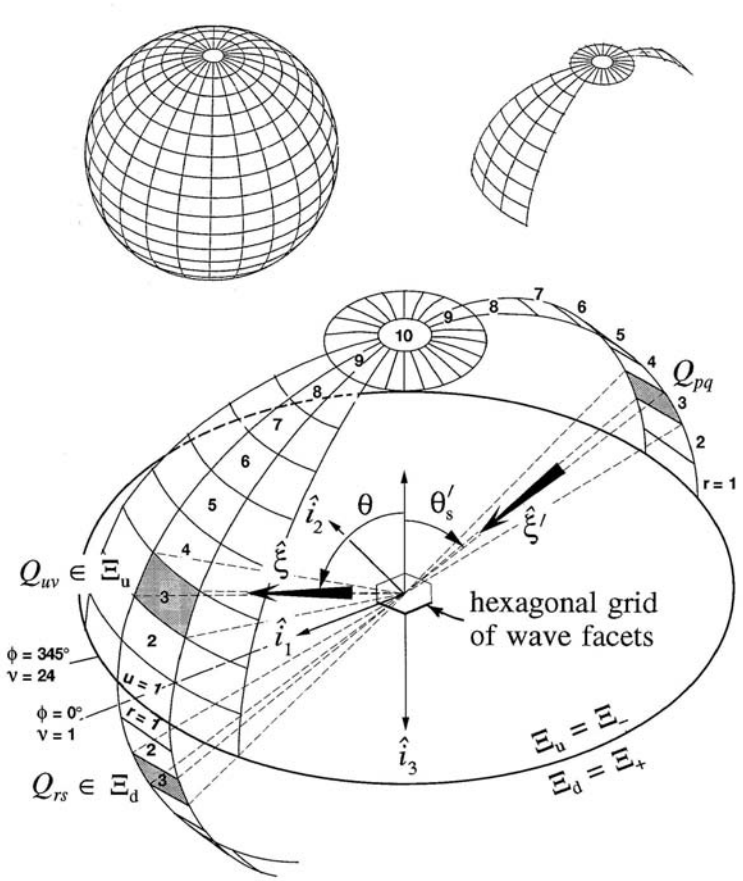

Fig. 4.20. A portion of the upper (Ξ_u) hemisphere of Fig. 4.19(b), showing the ray-tracing geometry. A ray source quad Q_{pq}, input quad Q_{rs}, and the associated specular-reflectance quad Q_{uv} are shown shaded. The insets clarify the relation of the main figure to the full sphere of quads.

can be made for the case of water-incident rays and the values of $r(w,a;r,s \rightarrow u,v)$.

Figure 4.21 shows the value of the continuous Fresnel reflectance function $r(\theta_s')$ for air-incident rays superimposed on the values of $r(a,w;r,s \rightarrow r,s)$ as computed by tracing 1000 rays toward each input quad Q_{rs}, $r = 1, ..., m = 10$, shown in Fig. 4.20. The corresponding curve of $r(\theta_s')$ for water-incident rays is also compared to $r(w,a;r,s \rightarrow r,s)$. The quad-averaged values are clearly good estimates of the average of $r(\theta_s')$ over the θ ranges of the various quads.

Table 4.1 Quad specifications for the $m = 10$, $n = 12$, equal $\Delta\theta$ partition of Fig. 4.19(b).

quad u index	θ range (deg)	μ range	average μ value, μ_u	quad solid angle, Ω_{uv} (sr)
1	80.53 - 90.00	0.000 - 0.165	0.0823	0.0431
2	71.05 - 80.53	0.165 - 0.325	0.2446	0.0419
3	61.58 - 71.05	0.325 - 0.476	0.4003	0.0396
4	52.11 - 61.58	0.476 - 0.614	0.5451	0.0362
5	42.63 - 52.11	0.614 - 0.736	0.6750	0.0318
6	33.16 - 42.63	0.736 - 0.837	0.7864	0.0266
7	23.68 - 33.16	0.837 - 0.916	0.8765	0.0206
8	14.21 - 23.68	0.916 - 0.969	0.9426	0.0140
9	4.74 - 14.21	0.969 - 0.997	0.9830	0.0071
10	0.00 - 4.74	0.997 - 1.000	0.9983	0.0215

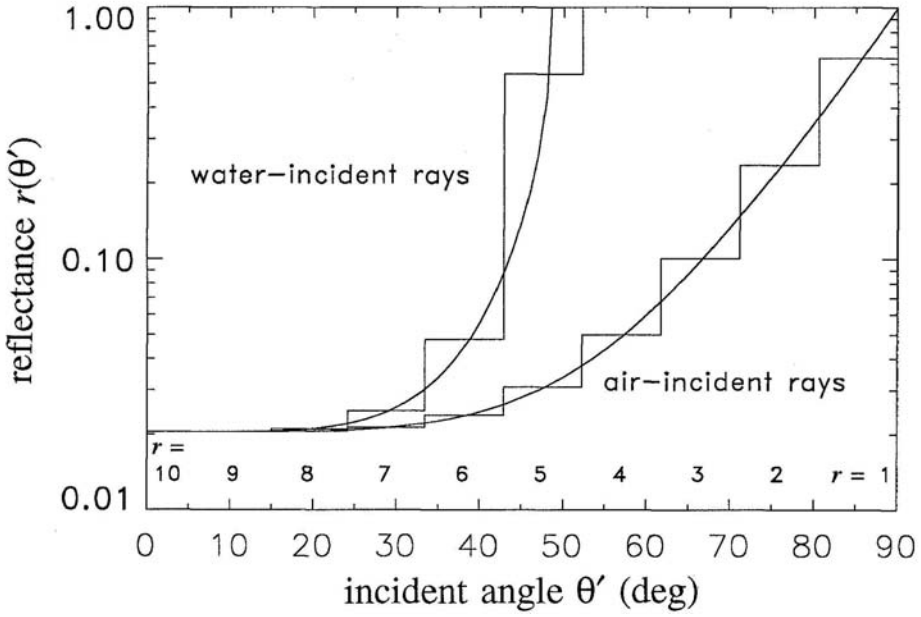

Fig. 4.21. Fresnel reflectances for $n_w = 4/3$ (smooth curves) and the corresponding quad-averaged radiance reflectances (stair-step curves), for the case of a level water surface.

Capillary wave surfaces; air-incident rays

If the wind speed is greater than zero, so that the air-water surface is covered by capillary waves as described in Section 4.3, then the daughter rays $\hat{\boldsymbol{\xi}}$ belonging to a given incident ray $\hat{\boldsymbol{\xi}}'$ may be directed toward any quad Q_{uv}, and the simple geometry of Fig. 4.20 no longer holds. We shall illustrate the effects of the capillary waves for a wind speed of U = 10 m s^{-1} and for the same input quad Q_{rs} shown shaded in Fig. 4.20.

Figure 4.22 graphically displays the results of one Monte Carlo experiment, which traced 10,000 initial rays toward the same input quad Q_{rs}, $r = 3$, illustrated in Fig. 4.20. Each initial ray used a different realization of the capillary-wave surface. As always, the wind is in the $\hat{\boldsymbol{i}}_1$ direction, so that $\phi' = 0$, as in Fig. 4.6. Now, however, the tilted wave facets cause the reflected and refracted daughter rays $\hat{\boldsymbol{\xi}}$ to be directed into many different quads Q_{uv}.

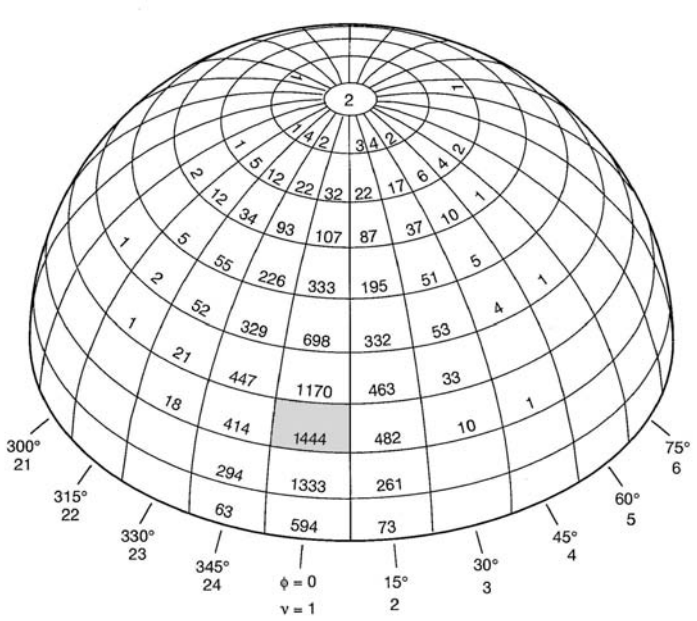

Fig. 4.22. A perspective view of the upper (Ξ_u) hemisphere of Fig. 4.19(b). The number in each quad gives the total number of reflected daughter rays ending up in that quad, for one Monte Carlo experiment tracing 10,000 air-incident initial rays for a wind speed of U = 10 m s^{-1}. The shaded specular quad $Q_{uv} = Q_{3,1}$ would receive all 10,000 reflected rays in the case of zero wind speed. Quads with no number never received a reflected ray.

The numbers in the quads give the total number of reflected rays falling into each quad. The "specular quad" $Q_{uv} = Q_{3,1}$ (shown shaded) would have received all 10,000 reflected rays in the case of a level water surface (as in Fig. 4.20). In this experiment with capillary wave surfaces, $Q_{3,1}$ received only 1,444 reflected rays which, not surprisingly, is the most of any quad. Quads near the specular quad also received substantial ray counts. Quads located at an angular distance of more than 45° from the specular quad received few, if any, reflected rays.

The observant reader will note that the total number of rays displayed in Fig. 4.22 is only 9,991. For a horizontally *finite* hexagonal grid of wave facets, daughter rays sometimes leave the hexagonal domain of Fig. 4.6 before they have completed their multiple scattering interactions with the simulated water surface. In the present experiment there were 9 such rays. The number of such "lost" rays can be made arbitrarily small by making the hexagonal grid sufficiently large; this, however, increases the computational costs. The loss of one ray per thousand is a reasonable tradeoff between cost and accuracy.

The displayed ray count also gives an indication of the magnitude of the statistical fluctuations associated with the Monte Carlo ray tracing technique. Since, in this experiment, both the wind and the incident rays are in the $\phi = 0$ direction, the elliptical symmetry of the water surface [recall Eq. (4.42)] implies that, *on average*, equal numbers of rays should be reflected into azimuthal directions ϕ and $2\pi - \phi$. Thus in Fig. 4.22, for a given u value (i.e. for a given μ-band of quads), we would expect on average to have equal ray counts for quads Q_{uv} with $v = 2$ and $v = 24$, $v = 3$ and $v = 23$, and so on. We see, for example, that the ray counts for quads $Q_{u,2}$ and $Q_{u,24}$ differ by typically 15%, for this experiment with 10,000 initial rays. A corresponding asymmetry can be expected in the $r(a,w;r,s\rightarrow u,v)$ values computed from these rays.

This statistical fluctuation can be made arbitrarily small by tracing a sufficient number of rays, with an attendant increase in computation expense. Any user of Monte Carlo techniques must decide how much statistical error can be tolerated in the computed results and then determine (most likely by numerical experimentation) how many Monte Carlo simulations must be performed (e.g., how many rays must be traced).

Figure 4.23 displays the ray counts for the transmitted, or refracted, daughter rays generated by the same 10,000 air-incident rays just discussed. These are the rays used to compute $t(a,w;r,s\rightarrow u,v)$. In Fig. 4.23 we are in the position of a scuba diver looking up toward the water surface. Two features of the transmitted ray count deserve comment. First, the angular distribution of the transmitted rays is noticeably tighter than for the reflected

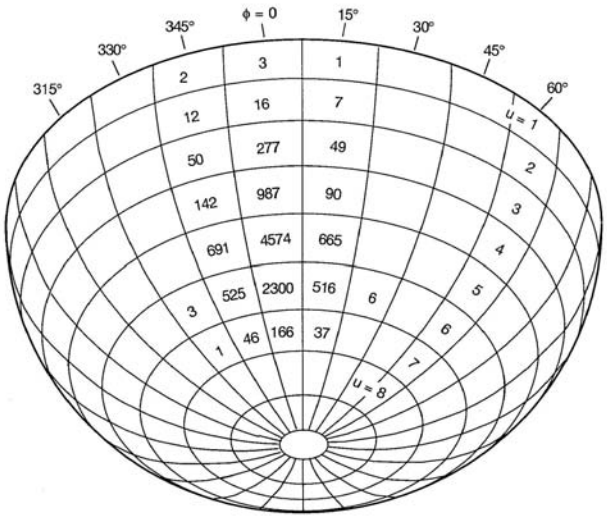

Fig. 4.23. A perspective view of the lower (Ξ_d) himisphere of Fig. 4.19(b); the azimuthal, or ϕ, orientation matches that of Ξ_u in Fig. 4.22. The numbers give the total number of transmitted (refracted) rays ending up in each quad, for the same 10,000 air-incident parent rays tallied in Fig. 4.22.

rays of Fig. 4.22. Second, the quad receiving the most rays is the one with $u = 5$, which is nearer to the nadir direction than the incident quad Q_{rs} ($r = 3$) is to the zenith direction. The first feature represents the well-known "focusing" of rays when passing from air to water and, like the second feature, is a direct consequence of Snell's law. *The presence of these features in the transmitted rays is evidence that the n^2 law for radiance, Eq. (4.21), is properly modeled by the ray-tracing procedure.*

Finally, we remark that of the 10,000 initial rays of this experiment, 8,918, or 89%, underwent a single-scatter, three-branch interaction with the surface, as shown in upper left of Fig. 4.9. The double-scatter, five-branch event of Fig. 4.9 occurred 1,004 times, for 10% of the total. Still higher order scattering accounted for 1% of the interactions. Thus multiple scattering occurred for 11% of the incident rays. This number is seen to be compatible with the results displayed in Fig. 4.10, after noting in Table 4.1 that the incident rays had θ' values from 61.6° to 71.1°. The number of transmitted rays tallied in Fig. 4.23 is 11,166, owing to the proliferation of transmitted rays by multiple scattering events (see Fig. 4.9).

Each ray tallied in Figs. 4.22 and 4.23 had a power computed as a product of Fresnel reflectances and transmittances, as described in the

paragraphs leading to Eq. (4.68). Figure 4.24 shows the radiant power transfer functions $\Phi^{+-}(r,s\rightarrow u,v)$ computed as in Eq. (4.68a) from the rays tallied in Fig. 4.22. The numbers displayed are $100\times\Phi^{+-}$, i.e. a percent of the total incident power; recall that each incident ray is assigned unit power. Note that the specular quad at $u = 3$ (with 1,444 rays) received 1.401% of the power, whereas the quad below, at $u = 2$, received 1.962% of the power even though this quad received fewer (1,333) rays. The quad nearest the equator, at $u = 1$, tallied only 594 rays but received almost as much power, 1.307%, as the specular quad. This power distribution is explained by the observation that even though the $Q_{1,1}$ and $Q_{2,1}$ quads had fewer rays than the $Q_{3,1}$ quad, the average Fresnel reflectances for the individual rays were considerably greater for rays reflected into directions near the equator (so that the angle of incidence relative to the normal of the reflecting wave facet is large) than for rays reflected into the specular direction or poleward thereof. Summing the $\Phi^{+-}(r,s\rightarrow u,v)$ values as in Eq. (4.70a) yields a reflectance $r_{+}(r,s) = 0.092$, which is compatible with Figs. 4.11 and 4.12 for incident angles in the range of Q_{rs}, namely $61.6° \le \theta_s' \le 71.1°$.

The remaining 90.8% of the incident power is of course transmitted through the surface, into the water. Figure 4.25 shows the $\Phi^{++}(r,s\rightarrow u,v)$ values obtained from the rays tallied in Fig. 4.23. Note that almost 42% of all incoming power is transmitted through the surface and into only one quad, $Q_{5,1}$. This quad and its eight nearest neighbors account for almost 89% of the incident power.

The four radiant power transfer functions $\Phi_{\pm\pm}$ are easily interpreted, as we have just seen for Φ^{+-} and Φ^{++}. However, it is not the $\Phi_{\pm\pm}$ of Eq. (4.68) that are needed for *radiance* transfer computations, but rather the quad-averaged radiance transfer functions of Eq. (4.74). Figure 4.26 shows $r(a,w;r,s\rightarrow u,v)$ as obtained from the Φ^{+-} values of Fig. 4.24 and the μ and Ω factors of Table 4.1, using Eq. (4.74a). Figure 4.27 shows the $t(a,w;r,s\rightarrow u,v)$ values obtained from the $\Phi^{++}(r,s\rightarrow u,v)$ values seen in Fig. 4.25, using Eq. (4.74b). The numbers in these two figures do not lend themselves to a simple physical interpretation as did Φ^{+-} and Φ^{++}, owing to the presence of the geometrical factors in Eqs. (4.74a) and (4.74b); they are merely the numbers needed in the quad-averaged equations (4.66) and (4.67) in order to compute the reflectance and transmittance of the quad-averaged radiance $L(a;r,s)$ by the air-water surface, *for this particular quad partition and wind speed.*

It should be remembered that Figs. 4.22-4.27 pertain to one particular input quad Q_{rs}, one wind speed, and one set of 10,000 Monte Carlo realizations of the random air-water surface. A similar set of figures could be generated for every input quad and every wind speed, and the statistical

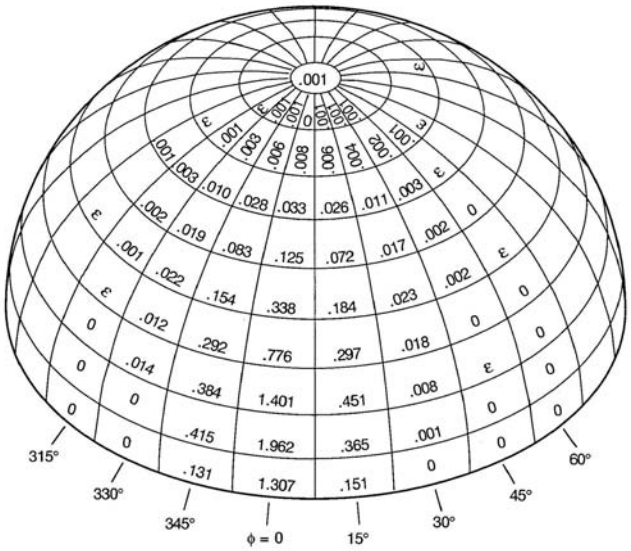

Fig. 4.24. The radiant power transfer function $\Phi^{+-}(r,s\rightarrow u,v)$ corresponding to Fig. 4.22. The plotted values are $100\times\Phi^{+-}$, i.e. Φ^{+-} as a percentage of the total incident power. ϵ denotes a plotted values less that 0.001, i.e. a value $\Phi^{+-} < 10^{-5}$.

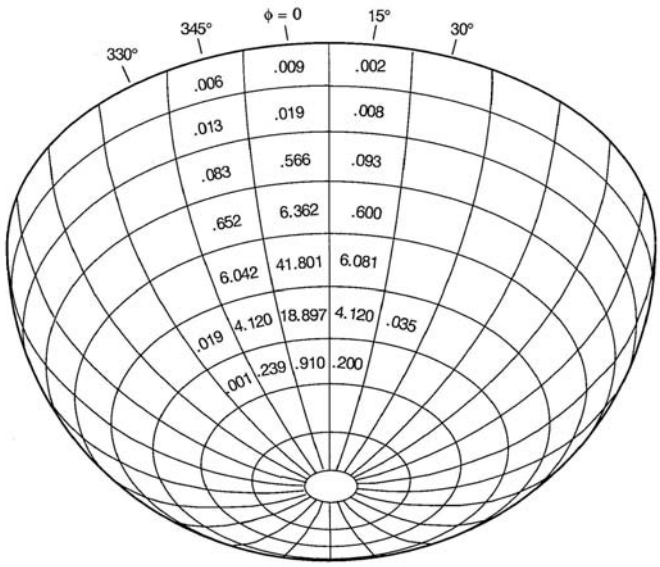

Fig. 4.25. The radiant power transfer function $\Phi^{++}(r,s\rightarrow u,v)$ corresponding to Fig. 4.23. The plotted values are $100\times\Phi^{++}$, i.e. Φ^{++} as a percentage of the total incident power.

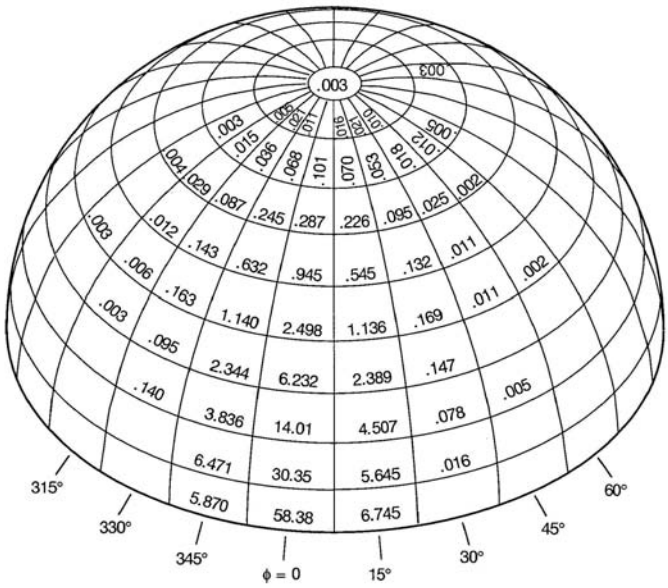

Fig. 4.26. The quad-averaged radiance reflectance function $r(a,w;r,s\rightarrow u,v)$ corresponding to Figs. 4.22 and 4.24. The numbers plotted are $10^3\times r(a,w;r,s\rightarrow u,v)$.

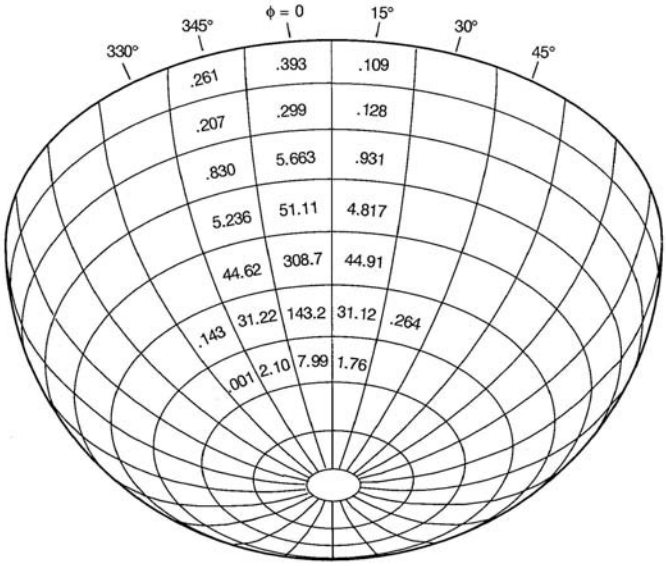

Fig. 4.27. The quad-averaged radiance transmittance function $t(a,w;r,s\rightarrow u,v)$ corresponding to Figs. 4.23 and 4.25. The numbers plotted are $10^3\times t(a,w;r,s\rightarrow u,v)$.

character of each of these data sets can be studied by making repeated, independent Monte Carlo experiments. Although such analyses must be meticulously done in order to verify the correctness of the numerical techniques and of the associated computer coding, a discussion of the results is beyond our present needs. There is, however, one other situation requiring comment, and that is the case of water-incident rays.

Capillary wave surfaces; water-incident rays

Think of turning Fig. 4.20 "upside down", so that the source quad Q_{rs} is in Ξ_+ and the initial rays $\hat{\xi}' \in \Xi_-$ are traveling upward and hitting the air-water surface from below. The reflected rays $\hat{\xi}$ are then heading downward, contributing to Φ^{-+} and $r(w,a;r,s\rightarrow u,v)$. The refracted rays are transmitted through the surface and into the air, contributing to Φ^{--} and $t(w,a;r,s\rightarrow u,v)$.

In the case of a level surface, all incident rays undergo total internal reflection, since Q_{rs} with $r = 3$ has θ_s' (now measured from the nadir direction) in the range $61.58° \le \theta \le 71.05°$, which is greater than the critical angle for total reflection, 48.59°, obtained from Eq. (4.13b). Thus $\Phi^{-+}(r,s\rightarrow u,v) = 1$ when Q_{uv} is the specular quad $Q_{3,1}$; all other elements of Φ^{-+} and all elements of Φ^{--} are zero.

When the wind speed is greater than zero, the incident rays will occasionally encounter capillary wave facets which are tilted so as to allow daughter rays to be transmitted through the surface, and the reflected and transmitted rays may be directed toward any quad.

Figure 4.28 shows the distribution of reflected rays obtained from tracing 10,000 water-incident initial rays, just as in the experiment previously described for the air-incident case. Once again, the specular-reflection quad (shown shaded) has received the most reflected rays. This ray-count diagram is not greatly different from that of the air-incident case shown in Fig. 4.22. Figure 4.29 shows the Φ^{-+} power distribution diagram belonging to Fig. 4.28. The $\Phi^{-+}(r,s\rightarrow u,v)$ values are much larger than the Φ^{+-} values for air-incident rays, shown in Fig. 4.24. These differences in air-incident and water-incident reflected power values are of course a consequence of the much larger Fresnel products of the water-incident reflected rays. Note, for example, in Fig. 4.28 that the quad $Q_{uv} = Q_{1,24}$ (the first μ-band at $\phi = 345°$) received 76 rays (i.e. 0.76% of the 10,000 initial rays). Now note in Fig. 4.29 that this quad received 0.76% of the total power. Thus we see that each of these 76 rays was the daughter ray of an initial ray that underwent total internal reflection, thereby receiving a Fresnel product of 1. Similar results can be seen in other quads near the equator.

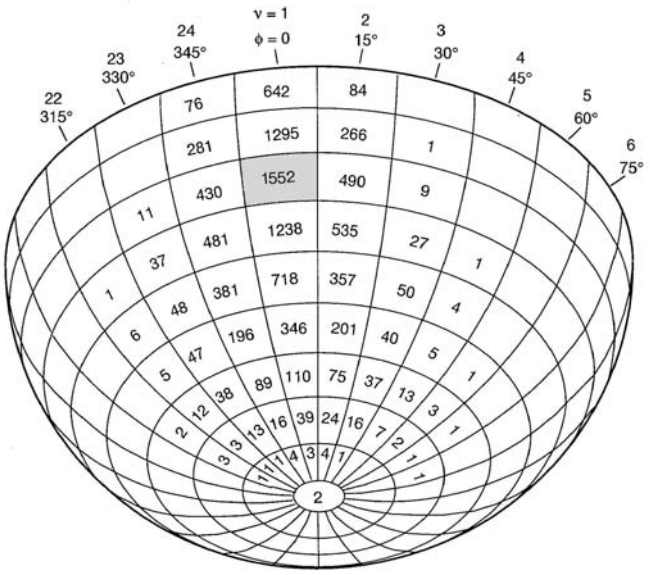

Fig. 4.28. The distribution of reflected daughter rays in the Ξ_d hemisphere, for 10,000 water-incident parent rays and for a wind speed of $U = 10$ m s^{-1}. The shaded specular quad would have received all 10,000 reflected rays in the case of a level surface.

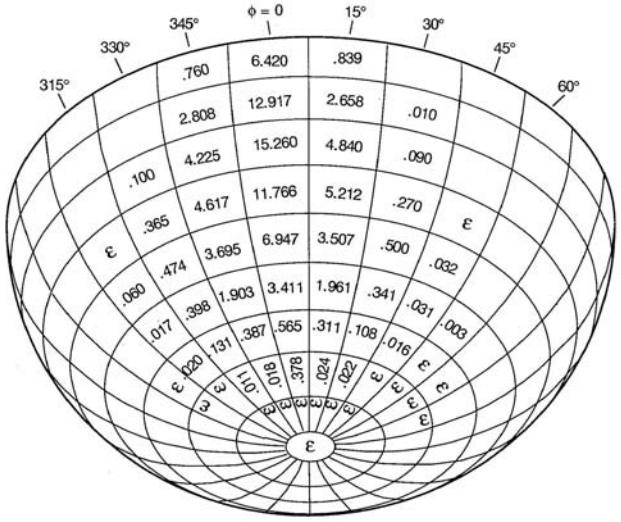

Fig. 4.29. The radiant power transfer function $\Phi^{-+}(r,s;u,v)$ corresponding to Fig. 4.28. The plotted values are $100\times\Phi^{-+}$, i.e. Φ^{-+} as a percentage of the total incident power.

The total ray count in Fig. 4.28 is 10,384, which is greater than 10,000 owing to multiple scattering; 84% of the ray-surface interactions were of the single-scatter, two-branch, total-internal reflection type seen in Fig. 4.9. The high frequency of total reflection gives a reflectance of $r_{-}(r,s) = 0.981$, which is consistent with an $r_{-}(\theta_s', \phi_s')$ value estimated from Fig. 4.14 for θ_s' in the range of 61° to 70°.

Only 493 rays were able to pass through the surface; their distribution is seen in Fig. 4.30. Figure 4.31 gives the corresponding power distribution $\Phi^{--}(r,s \rightarrow u,v)$, which leads to $t(w,a;r,s \rightarrow u,v)$. These Φ^{--} values total to 0.019, as expected.

When using the numerical model of Chapter 8 for radiance calculations, we must evaluate the four radiance transfer functions of Eq. (4.74) for *every* input quad Q_{rs} in Ξ. The elliptical symmetry of the capillary wave surface does, however, reduce the computation by a factor of four since, if the transfer functions are known for all quads in the "first quadrant" of Ξ (i.e. for $0 \le \phi \le \pi/2$), then the functions can be obtained for all other quads by quad versions of the symmetry relations (4.42). These matters are discussed in Section 8.5.

Moreover, *these surface computations need be done only once for a given wind speed and quad partitioning, because the ray-tracing model is independent of the water body and of the incident radiance to be imposed in any particular study*. There will always be quads that receive only a few daughter rays, and consequently the values of the transfer functions for these quads will be relatively uncertain. However, these quads account for only a very small part of the total power, and large relative errors in the associated transfer functions will have little effect on the overall radiance distribution. Those quads near the specular directions receive most of the power and therefore dominate the radiance distribution. It is computationally practicable to trace enough rays to guarantee that the larger elements in the transfer functions have errors of at most a few percent, which is acceptable for most radiance calculations. The actual number of initial rays that must be traced from each source quad depends on the quad solid angle and upon the wind speed, and must be determined on a case-by-case basis by a few independent Monte Carlo experiments like the ones discussed above. For a 10 m s^{-1} wind speed and for the quad-partitioning used in Figs. 4.22-4.31, tracing 50,000 rays from each input quad Q_{rs} appears to give acceptably accurate radiance transfer functions. Fewer rays need be traced for lower wind speeds.

We note in closing that the ray tracing procedures developed and used in this chapter are ideally suited to parallel processing. Thus it is reasonable to suppose that within a few years of this writing, researchers

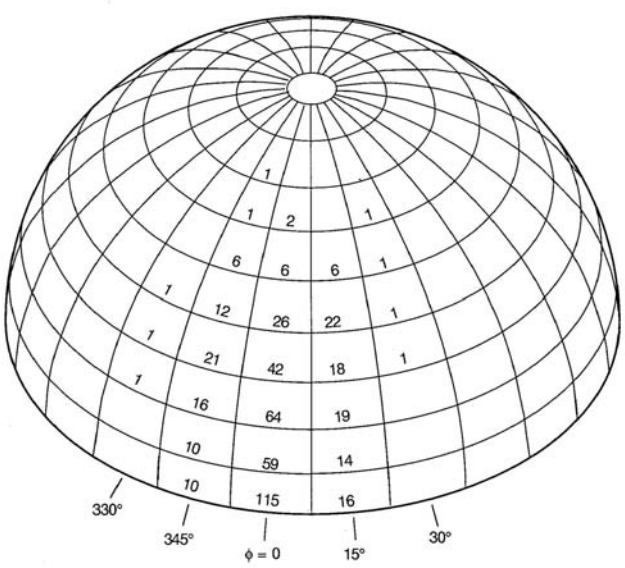

Fig. 4.30. The distribution of transmitted daughter rays in the Ξ_u hemisphere, for the same 10,000 water-incident parent rays of Fig. 4.28.

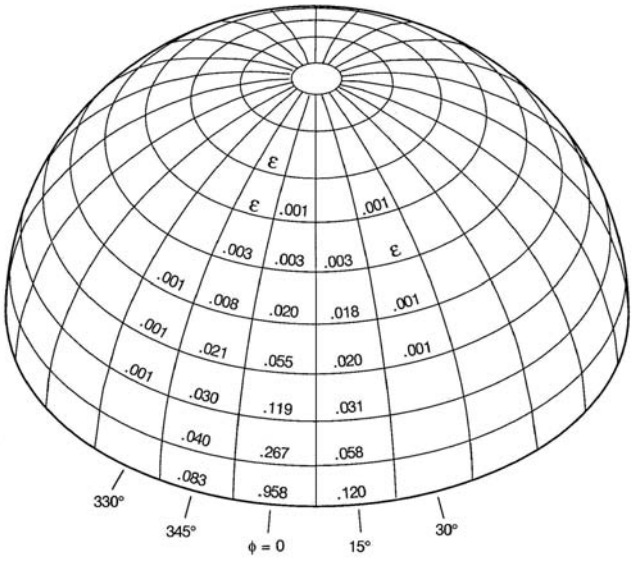

Fig. 4.31. The radiant power transfer function $\Phi^{--}(r,s\rightarrow u,v)$ corresponding to Fig. 4.30. The plotted values are $100\times\Phi^{--}$, i.e. Φ^{--} as a percentage of the total incident power. ϵ denotes a plotted values less that 0.001, i.e. a value $\Phi^{--} < 10^{-5}$.

will be able to trace, at nominal cost, millions of rays per quad, with quad resolutions as fine as that of Fig. 4.19(c), and with a fully developed sea replacing our capillary waves.

4.9 Extensions to Arbitrary Wave Spectra

The results presented on the previous pages pertain to an air-water surface covered by capillary waves, but otherwise level. This situation occurs in nature only for times shortly after the wind has begun to blow over a previously calm surface. It is to be expected that the optical properties of a well developed sea, over which the wind has been blowing for long times and extensive fetches, will be affected by the presence of the resultant gravity waves. In particular, at low solar elevations the effects of *wave shielding* may become important, because the incoming rays will tend to strike the "frontsides" of the large gravity waves while their "backsides" remain in shadow.

As has been mentioned, the ray-tracing algorithm based on the representation of the water surface by triangular wave facets is immediately applicable to the modeling of a surface on which gravity waves are present. *In principle*, it is necessary only to replace the capillary wave statistics (4.32) and (4.33) with equations defining the statistics of the desired wave spectrum. In practice, however, this replacement is not trivial. It is therefore worthwhile to illustrate how more complicated wave spectra can be incorporated into the numerical model.

We note first that modeling a full gravity-capillary wave surface in the brute-force manner of Section 4.3 would require an astronomical number of triangular wave facets: the facets must be small enough ($\leq$ 0.005 m) to resolve the optically dominant capillary waves, and the hexagonal domain of facets must be large enough ($\geq$ 100 m) to cover several wavelengths of the larger gravity waves. Such spatial resolution far exceeds the capabilities of even the largest computers. It is therefore also necessary to develop algorithms that dynamically generate (as the randomly directed daughter rays are generated) only those parts of the sea surface that are needed for interaction with the daughter rays generated by the previous interaction of a ray with the surface. That is to say, we need to generate only small patches of the sea surface at the locations of the ray-surface intersections. However, these patches must represent all scales of surface waves. Efficient algorithms for such a treatment of well developed seas have not been developed.

A hybrid gravity-capillary wave model

The next-best approximation to nature might be to use a gravity-wave spectrum to generate a random sea surface of triangular gravity-wave facets. These gravity-wave facets would resolve only the larger gravity-wave components – those larger than 1 m, for example. Ray tracing would be initiated with a realization of the gravity-wave surface. Whenever an incoming ray $\hat{\boldsymbol{\xi}}'$ intersects a gravity wave facet, then that facet alone can be covered with a surface of capillary waves, generated as in Section 4.3. The ray-surface interaction would then be completed with the capillary waves "riding" on the tilted gravity wave facet. Tilting by the gravity waves can then be thought of as producing a systematic change in the incoming ray direction relative to the capillary waves riding on the gravity wave facet. Thus when a ray strikes a gravity wave facet that is tilted toward the sun, the capillary waves on that facet see the sun as being "higher in the sky" relative to the plane of their gravity wave facet.

Figure 4.32 quantifies this idea, using gravity waves generated in the manner described below. Let $\hat{\boldsymbol{n}}$ be the surface normal of the gravity wave facet that has intercepted an incoming ray $\hat{\boldsymbol{\xi}}'$, and let θ_c' be the *equivalent* zenith angle for capillary waves on the gravity wave facet. That is, a tiny observer on the gravity wave facet would see $\hat{\boldsymbol{\xi}}'$ come in at the angle θ_c' from the local normal. For a flat horizontal surface, $\hat{\boldsymbol{n}} = -\hat{\boldsymbol{i}}_3$ and $\theta_c' = \theta_s'$, the true zenith angle of the incoming rays. Figure 4.32 shows the average (over thousands of incident rays) of θ_c' as a function of wind speed and true zenith angle θ_s'. This figure gives us an idea of when gravity-wave tilting is important. For incident angles of $\theta_s' \leq 60°$, there is little shielding over the wind speed range from 0 to 20 m s^{-1}, and so the incoming rays are rarely intercepted in their way to the target facet. The average θ_c' is therefore equal to θ_s'. For rays incident from nearer the horizon, shielding becomes noticeable at the higher wind speeds. Thus at sunset ($\theta_s' = 90°$) the capillary waves on the gravity waves see a solar position which on average is around 10° above their horizon (i.e. $\theta_c' \approx 80°$) at a wind speed of 20 m s^{-1}.

Such two-scale models of the sea surface have been used in studies of radar backscatter by wind-generated waves (Donelan and Pierson, 1987, and references therein). However, further investigations of the optical properties of this hybrid gravity-capillary wave model have not been made.

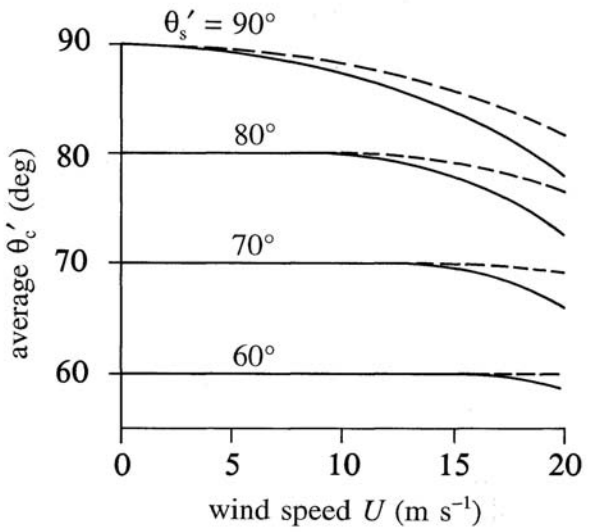

Fig. 4.32. The average equivalent polar angle θ_c' as a function of the wind speed and of the true polar angle θ_s'. Solid lines are for $\phi_s' = 0°$ (incident rays parallel to the wind), and dashed lines are for $\phi_s' = 90°$ (incident rays perpendicular to the wind). [redrawn from Preisendorfer and Mobley (1985)]

Generating a gravity-wave surface ▌▌

It is worthwhile to sketch how the realizations of a random gravity-wave surface were generated in the studies leading to Fig. 4.32, since the technique is applicable to any wave spectrum.

A rectangular, wind-based coordinate system for gravity waves on the sea surface is shown in Fig. 4.33. The horizontal plane of the system rests at mean sea level. The region covered is $2X$ by $2Y$ meters and the x-axis lies downwind. (Our notation in this section deviates slightly from that adopted in Section 4.1; here we use x and y as horizontal coordinates). The distances $2X$ and $2Y$ are divided respectively into 2ℓ and $2m$ equal parts, forming a grid of alongwind and crosswind coordinate lines, of spacings $\Delta x = X/\ell$ and $\Delta y = Y/m$. A point (or node) on the grid is located by the pair of integers (i,j), with $-\ell \le i \le \ell$ and $-m \le j \le m$.

The ω^{th} realization of a spatially stationary, zero-mean random surface over this grid is defined by a surface elevation function η whose value (in meters), at node (i,j) is (Preisendorfer, 1988, p.155)

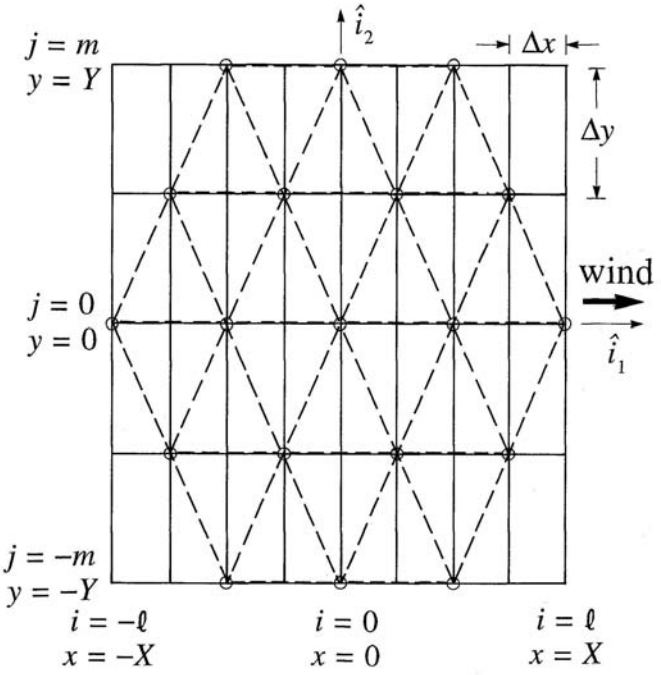

Fig. 4.33. The rectangular, spatial-domain (x,y) coordinate system (solid lines) used to construct a random air-water surface of triangular gravity-wave facets. The facet triads corresponding to Fig. 4.6 are shown by dashed lines. [redrawn from Preisendorfer and Mobley (1985)]

$$\eta(i,j;\omega) = \sum_{(u,v)\in W} \left[b_{uv}(\omega) \cos 2\pi \left(\frac{ui}{p} + \frac{vj}{q} \right) + c_{uv}(\omega) \sin 2\pi \left(\frac{ui}{p} + \frac{vj}{q} \right) \right]. \tag{4.77}$$

Here W is the set of (u,v) values such that $u = 0$ and $1 \le v \le m$, or $1 \le u \le \ell$ and $-m \le v \le m$; $p = 2\ell + 1$ and $q = 2m + 1$. The quantities b_{uv} and c_{uv} are independent, normally distributed random variables of zero mean and variances

$$\mathscr{E}\{b_{uv}^2\} = \mathscr{E}\{c_{uv}^2\} = E(k_u,k_v)\,\Delta u\,\Delta v\,, \tag{4.78}$$

where

$$(u,v) \in W,$$

$$\Delta u = \frac{2\pi}{p\,\Delta x}, \qquad \Delta v = \frac{2\pi}{q\,\Delta y},$$

$$k_u = u\,\Delta u, \qquad k_v = v\,\Delta v.$$

The quantity $E(k_u,k_v)$ is the *directional energy spectrum* of the waves in rectangular coordinate form. As before, $\mathscr{E}$ denotes the ensemble average over the $\omega = 1, \ldots, S$ realizations of the random surface. The spectral domain W is shown in Fig. 4.34. $E(k_u,k_v)$ has the symmetry $E(-k_u,-k_v) = E(k_u,k_v)$, so that W covers all wave trains moving generally downwind.

The directional energy spectrum for gravity waves as deduced from observation during the Stereo Wave Observation Project (SWOP; Cot , *et al.*, 1960; see also *H.O. VI* Chapter 12) is given by

$$E(k_u,k_v) = F(\sigma_{uv},\phi_{uv})\frac{g^2}{2\sigma_{uv}^3} \qquad (\mathrm{m}^4), \tag{4.79}$$

where

See Note

$$\sigma_{uv} = (g k_{uv})^{1/2} \qquad (\mathrm{s}^{-1}),$$

$$\phi_{uv} = \tan^{-1}\left(\frac{k_v}{k_u}\right),$$

$$k_{uv} = (k_u^2 + k_v^2)^{1/2} \qquad (\mathrm{m}^{-1}),$$

$$F(\sigma_{uv},\phi_{uv}) = C\,\sigma_{uv}^{-6}\exp\left[-2\left(\frac{g}{\sigma_{uv}U}\right)^2\right] f(\sigma_{uv},\phi_{uv}) \qquad (\mathrm{m}^2\,\mathrm{s}),$$

$$f(\sigma_{uv}.\phi_{uv}) = 1 + (0.50 + 0.82\xi)\cos(2\phi_{uv}) + 0.32\xi\cos(4\phi_{uv}),$$

$$\xi = \exp\left[-\frac{1}{2}\left(\frac{\sigma_{uv}U}{g}\right)^4\right],$$

$$C = 0.763\ \mathrm{m}^2\,\mathrm{s}^{-5} \quad \text{and} \quad g = 9.80\ \mathrm{m}\,\mathrm{s}^{-2}.$$

The first four of these equations are completely general; the last four define the SWOP spectrum [see Supplementary Note 6]. This formidable set of equations (4.77)-(4.79) is used as follows. Select the wind speed U (in meters per second). This fixes the frequency (*H.O. VI*, p. 187)

$$\sigma_{\max} = \left(\frac{2}{3}\right)^{1/2}\frac{g}{U}$$

of the highest spectral energy density of waves represented by the spectrum. By $\sigma^2 = gk$ and $\lambda = 2\pi/k$, the value of $\sigma_{\max}$ also determines the associated wavelength

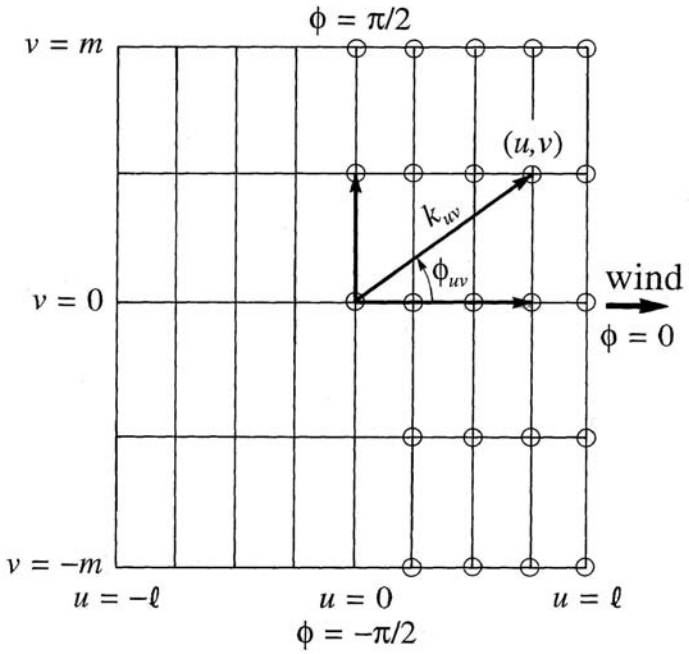

Fig. 4.34. The spectral-domain (u,v) coordinate system corresponding to the spatial domain of Fig. 4.33. W is the set of (u,v) values shown by circles. [redrawn from Preisendorfer and Mobley (1985)]

$$\lambda_{\max} = \frac{3\pi U^2}{g}$$

of the waves of maximum energy density. (Note that this λ is the wavelength of the water waves, not the wavelength of light.) This wavelength can be used to set the physical scale of the hexagonal grid of Fig. 4.33. For example, $X = Y = 4\lambda_{\max}$ would give an hexagonal domain capable of resolving four wavelengths of the maximum-energy waves. Each of the maximum-energy waves is resolved according to the choice of ℓ and m: $\ell = m = 24$, say, gives $\Delta x = \Delta y = \lambda_{\max}/24$. Note that the simple scaling of Eq. (4.39), e.g. the choice of $\delta = 1$, no longer holds. Once the grid resolution has been fixed, $E(k_u,k_v)$ is determined from Eq. (4.79) evaluated for each pair of integers (u,v) in W. *This calculation is performed only once.* Finally, to construct the ω^{th} realization of a random surface, for each $(u,v) \in W$ we randomly draw (for the ω^{th} time) independent samples $b_{uv}(\omega)$ and $c_{uv}(\omega)$ from a normal distribution of zero mean and variance $E(k_u,k_v)\Delta u\Delta v$ [recall Eq. (4.78)]. The surface elevation $\eta(i,j;\omega)$ at node (i,j) is then found from Eq. (4.77) using the samples $b_{uv}(\omega)$ and $c_{uv}(\omega)$ just

drawn. An example of a sea surface simulated in this manner [using a different wave spectrum than Eq. (4.77)] can be seen in McLean (1990; his Fig. 2).

Note in Fig. 4.33 that the vertices of the wave triads, used to define the triangular wave facets, coincide with every other (i,j) point of the rectangular grid used to define $E(k_u,k_v)$. Thus Eq. (4.77) need be evaluated at only those (i,j) nodes coinciding with a triad vertex (the points shown by circles in Fig. 4.33).

Techniques similar to that just described have been used in recent studies of ocean glitter patterns. For example, Tse, *et al.* (1990) show a very realistic looking simulation of a moonlit sea surface (their Fig. 7). However, systematic investigations of the radiative transfer properties of a well developed sea have not been made, in part because the requisite computer power has not been available.

4.10 Limitations of the Air-Water-Surface Model

The mathematical techniques developed in this chapter for describing wind-blown water surfaces are imperfect in several ways related to spatial (or wave) and temporal resolution, and to the omission of relevant physics.

Spatial and temporal resolution

The modeling of a sea surface as capillary waves of scales ~0.01 m riding of gravity waves of scales ≥ 1 m is clearly a poor simulation of nature. Real water surfaces comprise waves of all sizes in a continuous distribution from the smallest to the largest, and this physics should be incorporated into the numerical simulation of the random water surface.

Water-wave spectra are an area of continuing research in hydrodynamics, and the literature abounds with semi-empirical and theoretical formulas for $E(k_u,k_v)$ and related quantities. Each new set of measurements of wind-generated waves seems to require a slightly different energy spectrum for its description. This is not surprising, since the exact nature of the wind-blown surface depends on the history of the surface – how long the wind has been blowing, over what fetch, on the presence of currents, etc.

The SWOP spectrum (4.79) is quite out of date for purposes of understanding the details of wave growth and dissipation. We have presented it here only because it is the spectrum used to generate Fig. 4.32. Recently developed spectra include all size scales from capillary to gravity

in a continuous fashion (Glazman, 1993, and references therein). These more sophisticated spectra are essential for understanding wave turbulence and the nonlinear cascade of energy from larger to smaller scales. The use of such spectra already has advanced our understanding of radar backscatter by the sea surface beyond that obtained from two-scale models (Glazman, 1990). Equations (4.77) and (4.78) are valid for all wave spectra. We need only replace Eqs. (4.79) with the equations describing the desired wave spectrum, and then procede as described above. However, such calculations at visible wavelengths, as are needed to revise Figs. 4.11-4.17 to include the effects of waves larger than capillary waves, are yet to be made.

We also reiterate that the surface reflectance and transmittance properties computed in this chapter are *time-averaged* values. Surface waves can generate an interesting and important time-dependent phenomenon known as *wave focusing*, in which light rays passing through the surface are occasionally refracted in just the right directions so as to focus at a particular point below the surface. Wave focusing is familiar to anyone who has noticed the fluctuating pattern of bright light on the bottom of a swimming pool. Wave focusing is important because the responses of biological organisms or of some instruments to a rapidly fluctuating light field of some average value may be different than the responses to a steady light field of the same average value.

Figure 4.35 illustrates the character of the fluctuations in the downwelling plane irradiance. The figure shows a one-second-long time series of E_d measured at a depth of $z = 0.5$ m and a wavelength of $\lambda = 525$ nm. Note that the irradiance exceeded twice its average value $\bar{E}_d$ three times in one second, and that one "flash" in E_d was 4.5 times the average value. Observation and simple modeling [e.g. Stramski (1986), Stramski and Dera (1988)] show that wave focusing effects are most pronounced at high solar elevation, at wind speeds less than 5 m s^{-1}, and when the sky and water are clear. Typical flashes last for a few tens of milliseconds. The intensity of the flashes damps out rapidly with depth, so that the fluctuations in E_d are small below the upper few meters of the water column. Relatively smooth surface waves with lengths of centimeters to tens of centimeters appear to be most responsible for wave focusing.

Whitecaps and foam

The models developed above also omit the effect of whitecaps and foam, which are present at wind speeds greater than a few meters per second, and which can have a pronounced effect on the optical properties of the sea surface. To be precise, we must distinguish between *whitecaps*,

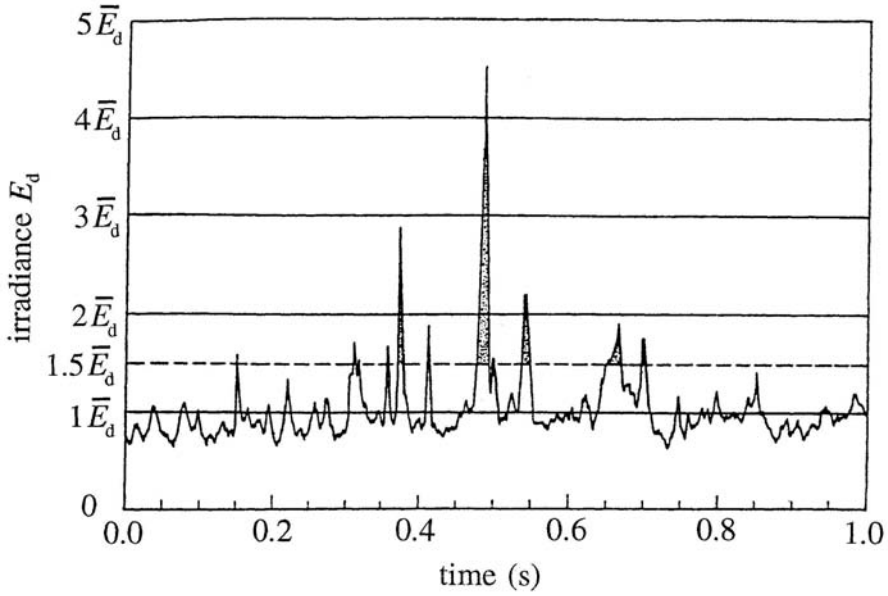

Fig. 4.35. Measured time series of spectral downwelling plane irradiance $E_d(t)$ showing the effects of wave focusing. $\bar{E}_d$ is the average value of $E_d(t)$ over the one-second observation period. [redrawn from Stramski (1986), with permission]

which are the foamy part of actively breaking waves, and the total area covered by all foam, including that which is left over after a wave has broken. The whitecap area is determined by the hydrodynamics of the waves; the total foam area depends also on water chemistry and air-sea temperature differences. There is often a factor of ten difference in the two areas. A proper dynamical treatment of whitecaps is difficult [see Monahan and MacNiocaill (1986), and Glazman and Weichman (1989)], but a crude estimate of the effect of foam can be made as follows.

Consider the computation of the irradiance reflectance $r_+ = r(a,w)$, as was presented in Fig. 4.16. Let f be the fractional area of the wind-blown sea surface that is covered by foam, $0 \le f \le 1$. Then $1 - f$ is the fractional area of the surface that is free of foam, and for which the computed reflectance $r(a,w)$ is assumed to hold. If we assign an average reflectance r_{foam} to the foam, $0 \le r_{foam} \le 1$, then the average reflectance $\bar{r}$ of the sea surface can be estimated as

$$\bar{r} = f\, r_{foam} + (1 - f)\, r(a,w)\,. \tag{4.80}$$

The value of f depends on the air-sea temperature difference, as well as upon wind speed. Monahan and O'Muircheortaigh (1986) present the empirical formula

$$f = 1.95\times10^{-5}\, U^{2.55} \exp\left[\, 0.0861\, (T_w - T_a)\right],$$

where U is the wind speed in meters per second measured at an elevation of 10 m, and T_w and T_a are respectively the water and air temperatures in degrees Celsius. Glazman and Weichman (1989) present a formula the fraction of the sea surface that is covered by whitecaps; their formula is based on theoretical considerations of the hydrodynamics of breaking waves.

The reflectance of newly made, thick foam in whitecaps is typically greater than 0.5. The reflectance decreases with time as the foam ages and eventually disappears. The average value of r_{foam} over the life of a patch of foam is likely in the range of 0.2 to 0.3 (Koepke, 1984). Using a value of f = 0.02, appropriate for neutral stability ($T_w = T_a$) and U = 15 m s^{-1} in the preceding formula, a value of r_{foam} = 0.3, and $r(a,w)$ = .05 (see Fig. 4.16), Eq. (4.80) yields $\bar{r}$ = 0.055. This value is 10% greater than the computed value of $r(a,w)$ = 0.05. It can be inferred from crude analyses of this sort that the reflectances $r(a,w)$ computed by ray tracing are ~10% too low at the higher wind speeds. The effect of foam is expected to be much greater at very high wind speeds ($U \geq 30$ m s^{-1}); then the contribution of the foam to $\bar{r}$ may equal the contribution of the foam-free surface.

An interesting method for dynamically incorporating whitecaps into a glitter simulation has been developed by Tse, *et al.* (1990). Gordon and Jacobs (1977) performed a crude numerical study of the effects of foam on the earth's albedo and concluded that sea foam often may be as important as the water itself in determining the earth's albedo. However, comprehensive studies of the optical effects of whitecaps and foam have not been made, in spite of the significant influence they may have on radiative transfer across the air-water surface.

4.11 Lambertian Bottom Surfaces

This chapter has been devoted to a detailed discussion of the time-averaged radiative-transfer properties of air-water surfaces. However, sandy or muddy bottoms in shallow waters can also greatly affect the nature of the underwater light field, and of the light leaving the air-water surface. We saw proof of this in Figs. 2.6 and 2.7. Such surfaces therefore require some discussion.

Consider an opaque, reflecting bottom boundary $S[m,b]$ whose radiance reflectance function is

$$r(m,b;\hat{\xi}'\rightarrow\hat{\xi}) = r(m,b;\theta',\phi'\rightarrow\theta,\phi) = \frac{R}{\pi}\cos\theta', \qquad (\mathrm{sr}^{-1}) \tag{4.81}$$

where $0 \le R \le 1$ and $\hat{\xi}' \in \Xi_d$, $\hat{\xi} \in \Xi_u$. Substituting Eq. (4.81) into an irradiance reflectance equation of the form of Eq. (4.7b) gives

$$r(m,b) = \frac{1}{E_d(m)} \int_{\Xi_u} \left[\int_{\Xi_d} L(m,\hat{\xi}') \frac{R}{\pi} \cos\theta' \, d\Omega(\hat{\xi}') \right] |\cos\theta| \, d\Omega(\hat{\xi}) \tag{4.82a}$$

$$= \frac{1}{E_d(m)} \frac{R}{\pi} \int_{\Xi_u} \left[E_d(m) \right] |\cos\theta| \, d\Omega(\hat{\xi}) \tag{4.82b}$$

$$= -\frac{R}{\pi} \int_0^{2\pi} \int_{\pi/2}^{\pi} \cos\theta \sin\theta \, d\theta \, d\phi = R . \tag{4.82c}$$

We have used the definition of E_d in going from Eq. (4.82a) to (4.82b). Equation (4.5) written for the bottom boundary reads

$$E_u(m) = E_u(b)\, t(b,m) + E_d(m)\, r(m,b) .$$

Letting $t(b,m) = 0$ for an opaque bottom, we see that $r(m,b)$ is just the irradiance reflectance of the opaque bottom, so

$$r(m,b) = \frac{E_u(m)}{E_d(m)} = R . \tag{4.83}$$

This result gives us a simple physical interpretation for the R of Eq. (4.81).

Surfaces whose radiance reflectance is of the form of Eq. (4.81) are called *Lambertian surfaces*, and R is called the (irradiance) reflectance of the surface. The radiance reflected by a Lambertian surface is, in analogy to Eq. (4.3),

$$L(\hat{\xi}) = \int_{\Xi_d} L(\hat{\xi}') \frac{R}{\pi} \cos\theta' \, d\Omega(\hat{\xi}') = \frac{R}{\pi} E_d . \tag{4.84}$$

Note that $L(\hat{\xi})$ is independent of $\hat{\xi}$. *Although the radiance reflectance depends on the incident angle* θ'*, the radiance is reflected equally into all directions* (θ,ϕ). *This is the meaning of a Lambertian surface.* Such surfaces are also called *cosine reflectors*, for an obvious reason. Matte

surfaces such as sand or silt are reasonably well modeled as Lambertian reflectors.

4.12 Problems

4.1. Suppose that the sun is at a zenith angle of 60°, and that the radiance of the solar disk is L_s when measured in air. What will be the measured radiance of the solar disk if the instrument is placed just below a calm water surface? The submerged instrument points toward the refracted solar image. Repeat the above problem for a solar zenith angle of 85°.

4.2. Use the quad-averaging formalism to develop a formula giving E_{ou} in terms of the quad-averaged radiances.

4.3. Equation (4.84) shows that for a Lambertian surface, $E_u = RE_d$, where E_d is the plane irradiance incident onto the surface, and E_u is the plane irradiance reflected by the surface. What is E_{ou} for a Lambertian surface? Is there a value of R for which $E_{ou} = E_u$?

4.4. You wish to model the spring phytoplankton bloom in the Arctic, where the sun is always low in the sky. On a calm, clear day, with a level sea surface, a certain amount of light gets into the water. If the wind starts to blow, will more or less light get into the water? How might your answer change if the sky changes to a heavy overcast?

4.5. Show that the albedo of a water body can be written as

$$A = r(a,w) + [1 - r(w,a)] \frac{E_u(w)}{E_d(a)} . \tag{4.85}$$

Next rewrite $E_u(w)/E_d(a)$ as $R(w)E_d(w)/E_d(a)$ and use Eq. (4.6) to express $E_d(w)/E_d(a)$ in terms of $E_u(w)/E_d(a)$. Use these relations to transform Eq. (4.85) into an infinite series, which can be summed to give

$$A = r(a,w) + \frac{[1 - r(w,a)]\, R(w)\, [1 - r(a,w)]}{1 - R(w)\, r(w,a)} .$$

Use this exact formula to estimate the albedo of a water body for clear skys, sun at 45°, and wind = 5 m s^{-1}; assume that the water has $R(w) = 0.02$.

Next Chapter >>